Universidad EAFIT

Thesis of Master in Science

Compendium of Publications on:

Computational Geometry Applications in Industry 4.0

Master Student
Juan Camilo Pareja Corcho

Supervisors
Prof. Dr. Ing. Oscar E. Ruiz Salguero
Laboratory of CAD CAM CAE
Universidad EAFIT

Dr. Ing. Aitor Moreno Guerrero
Industry and Advanced Manufacturing
Vicomtech Foundation

Dr. Ing. Jorge Posada Velásquez
Associate Director
Vicomtech Foundation

Dissertation
Submitted in partial fulfillment of the requirements for the degree of Master of Engineering in the College of Engineering of Universidad EAFIT. This thesis results from joint research collaboration between Universidad EAFIT (Colombia) and Vicomtech Foundation (Spain).

UNIVERSIDAD EAFIT
COLLEGE OF ENGINEERING
MASTER PROGRAM IN ENGINEERING
MEDELLIN, COLOMBIA
NOVEMBER 2021

Dedication

To my friends and family.

Acknowledgments

> The only true voyage of discovery, the only fountain of Eternal Youth, would be not to visit strange lands but to possess other eyes, to behold the universe through the eyes of another, of a hundred others, to behold the hundred universes that each of them beholds, that each of them is.
>
> *Marcel Proust*

To my mother and father: without your support this would not have been possible.

I want to express my utmost gratitude to Prof. Dr. Ing. Oscar Ruiz Salguero for his effort, patience and professionalism. His words of advise have had a great impact in my life and I treasure them dearly.

I am grateful to Dr. Jorge Posada, Dr. Iñigo Barandiaran, and Dr. Aitor Moreno for trusting and supporting me during my internship in Vicomtech.

I am sincerely thankful to Universidad EAFIT and Vicomtech for helping and providing the funding for my research and my studies.

I would like to acknowledge Ing. MSc. Diego Montoya for his advises and friendship through my time in the Laboratory of CAD CAM CAE.

I am grateful to the whole team of Laboratory of CAD CAM CAE. Thank you for your help and friendship.

Contents

List of Figures

List of Tables

1 Introduction

Computational modeling of porous and lattice materials is a topic that attracts the attention of ongoing research efforts. Industries such as product design, additive manufacturing, biomedicine, automotive and aerospace are environments in which porous and lattice materials are of special interest given their properties.

Computer Aided Design (CAD) three-dimensional (3D) Models are nowadays ubiquitous in many engineering contexts: in the automotive industry, for instance, more than 30.000 different parts are needed for complete vehicle, and most of them have a 3D CAD representation. In this sense, the ability to inspect the topology and the geometry of a standard 3D CAD representation model (such as STEP) is of high importance. More particularly, feature recognition is a task where this model inspection is relevant for engineers and designers, since they can easily find features of interest that are related with specific tasks: optimization, planning of additional manufacturing processes, detection of design errors, etc.

Gerotor pumps play an important role in the aerospace industry, specially in the processes of cooling, lubrication and fuel boost and transfer. The design process of gerotor pumps usually involves: i) a *geometric modeling* stage in a CAD environment, ii) a *design verification* stage using fluid mechanics simulations to validate the efficiency and other desired characteristics of the pump, and iii) a *physical testing* stage to verify the predicted characteristics of the pump in a real test bank once the design has been validated through a simulation tool. Digital Twins would allow a faster workflow for the design and testing of gerotor pumps.

This work presents a compilation of different contributions to the problems stated in this introduction. Sections 1.1 and 1.2 summarize the articles included in this compendium and list all the co-authors associated to each publication. Sections 1.3 and 1.4 summarize the special advisors and industrial research projects associated with the Master Thesis. Section 1.5 reports the distinctions and acknowledgements awarded to the student during his Master Thesis. Finally, Section 1.6

explains to the reader how to follow this document.

1.1 Summary of Publications

In Table 1.1 are listed the published and submitted articles with their respective authorship and bibliographic information.

Table 1.1: List of publications related to this Master Thesis.

Item	**Bibliographic Information**	**Type / Status**
1	Diego Montoya-Zapata, Diego A. Acosta, Camilo Cortes, Juan Pareja-Corcho, Aitor Moreno, Jorge Posada, Oscar Ruiz-Salguero. (2020). *Meta-modeling of Lattice Mechanical Responses via Design of Experiments*. Presented in MACISE-2020- 2nd Intl. Conf, on Mathematics and Computers in Science and Engineering. ISBN: 978-94-6186-910-4. Madrid, Spain, January 14-16, 2020.	Conference Article / Published
2*	Diego Montoya-Zapata, Diego A. Acosta, Camilo Cortes, Juan Pareja-Corcho, Aitor Moreno, Jorge Posada, Oscar Ruiz-Salguero. (2020). *Approximation of the Mechanical Response of Large Lattice Domains Using Homogenization and Design of Experiments*. Published in Journal Applied Sciences, ISSN 2076-3417, 2020, 10(11), 3858, DOI: https://doi.org/10.3390/app10113858. Indexed in ISI (Q2), Scopus (Q1), Publindex (A1).	Journal Article / Published
3	Juan Pareja-Corcho, Oscar Betancur-Acosta, Jorge Posada, Antonio Tammaro, Oscar Ruiz-Salguero, Carlos Cadavid. (2020). *Reconfigurable 3D CAD Feature Recognition Supporting Confluent n-Dimensional Topologies and Geometric Filters for Prismatic and Curved Models*. Published in Journal Mathematics, MDPI, ISSN 2227-7390, 2020, 8(8), 1356, DOI: https://doi.org/10.3390/math8081356. Indexed in ISI (Q1), Scopus (Q3), Publindex (A1).	Journal Article / Published
4	Juan Pareja-Corcho, Aitor Moreno, Bruno Simoes, Asier Pedrera-Busselo, Ekain San-Jose, Oscar Ruiz-Salguero, Jorge Posada. (2021). *A Virtual Prototype for Fast Design and Visualization of Gerotor Pumps*. Published in Journal Applied Sciences, MDPI, ISSN 2076-3417, 2021, 11(3), 1190, DOI: https://doi.org/10.3390/app11031190. Indexed in ISI (Q2), Scopus (Q1), Publindex (A1).	Journal Article / Published

1.2 List of Co-authors of this Compendium of Publications

The names and affiliations of the co-author of the articles presented in this compendium are listed in Table 1.2.

Table 1.2: Co-authors of this compendium of publications.

Name	**Affiliation**
Diego Andrés Acosta Maya	Process Development and Design Research Group (DDP), Universidad EAFIT, Colombia
Carlos Cadavid Moreno	Functional Analysis Group, Universidad EAFIT, Colombia
Camilo Cortés Acosta	eHealth and Biomedical Applications, Vicomtech, Spain
Diego Alejandro Montoya Zapata	Laboratory of CAD CAM CAE, Universidad EAFIT, Colombia Industry and Advanced Manufacturing, Vicomtech, Spain
Aitor Moreno	Industry and Advanced Manufacturing, Vicomtech, Spain
Antonio Tammaro	Industry and Advanced Manufacturing, Vicomtech, Spain
Oscar Mauricio Betancur Acosta	Integration and Engineering Construction Services S.A. de CV, Mexico
Bruno Simoes	Industry and Advanced Manufacturing, Vicomtech, Spain
Asier Pedrera Busselo	Egile Innovative Solutions, Spain
Ekain San Jose	Egile Innovative Solutions, Spain
Juan Camilo Pareja Corcho	Laboratory of CAD CAM CAE, Universidad EAFIT, Colombia Industry and Advanced Manufacturing, Vicomtech, Spain
Jorge Posada	Vicomtech, Spain
Oscar Ruiz Salguero	Laboratory of CAD CAM CAE, Universidad EAFIT, Colombia

1.3 Special Advisors

In addition to the support provided by the Thesis supervisors in EAFIT and Vicomtech, the student was advised by the specialists in Table 1.3.

Table 1.3: Special Advisors related to this Master Thesis

Name	**Role**	**Entity**	**Topic**
Dr. Eng. Jorge Posada	Scientific Coordinator and Advisor	Vicomtech, Spain	Industrial application of Feature Recognition, applications of fluid mechanics to gerotor pumps
Prof. Dr. Carlos A. Cadavid	Scientific Advisor	Mathematics and Applications, Department of Mathematical Sciences, Universidad EAFIT, Colombia	Mathematical foundations of Feature Recognition
Dr. Eng. Aitor Moreno	Senior Researcher	Industry and Advanced Manufacturing, Vicomtech, Spain	Geometry Processing and Numerical Simulation
Dr. Eng. Bruno Simoes	Researcher	Industry and Advanced Manufacturing, Vicomtech, Spain	Programming Principles and Geometry Processing
M.Sc. Eng. Asier Pedrera Busselo	Senior Researcher	Egile Innovative Solutions, Spain	Mechanistic principles of gerotor pumps
M.Sc. Eng. Oscar Betancur Acosta	Senior Project Manager	Integration Engineering and Construction Services S.A. de C.V., Mexico	Industrial application of Feature Recognition

1.4 Projects

The student executed the previously cited research in the context of industrial projects hosted by Vicomtech Foundation (Spain). The student was granted an 18-month research internship at Vicomtech in the context of the colaboration agreement between Vicomtech Foundation and Universidad EAFIT for Master and PhD students. Part of this work is product of an intership conducted by the student at Integration Engineering and Construction Services S.A. de C.V. (Mexico) during his undergraduate studies. The student participated in the following projects:

1. **LatticeFEM**: development a rapid FEM-based methodology to estimate mechanical behaviour of large lattice materials. *Institutions:* Vicomtech, Spain; Laboratory of CAD CAM CAE, Universidad EAFIT, Colombia.

2. **Feature Recognition**: development of a fast feature recognition software for the automotive industry. *Institutions:* Integration Engineering and Construction Services S.A. de C.V., Mexico; Vicomtech, Spain; Laboratory of CAD CAM CAE, Universidad EAFIT, Colombia.

3. **LATIDO**: development of a digital twin tool for the design and evaluation of lubrication systems. *Institutions:* EGILE Innovative Solutions, Spain; Vicomtech, Spain; Laboratory of CAD CAM CAE, Universidad EAFIT, Colombia.

1.5 Distinctions

The following table presents the distinctions and acknowledgements that the student and the Master Thesis team achieved during the post-graduate process:

Table 1.4: Awards and Recognizements obtained by the Student related to this Master Thesis

Distinction	**Context**	**Observation**
Research Fellowship: Research in Industry and Advanced Manufacturing	Vicomtech Foundation (2020-1 to 2021-2)	48300 EUR for project cost and student's support during his stay at Vicomtech
Post-Graduate Scholarship: Recognizement for outstanding research in Undergraduate students	Universidad EAFIT (2020-1 to 2021-2)	48.379.776 COP covering academic credits of Master Courses
Award: Invitation to publish in journal Applied Sciences, MDPI	MACISE-2020- 2nd International Conference on Mathematics and Computers in Science and Engineering	January 14-16, Madrid, Spain

1.6 How to Read this Document

This document presents the developments of a research executed at the Laboratory of CAD CAM CAE at Universidad EAFIT (Colombia), and Vicomtech (Spain). The obtained results are a combination of computational geometry, data structures and algorithms, and mathematics. Numerical simulation plays an important role to test the accuracy and to evaluate the impact of the developed approaches. **All the articles included in this compendium have been submitted and accepted in peer-reviewed journals or conferences.**

Chapter 2 proposes a methodology that systematically uses Design of Experiments (DOE) to produce simple mathematical expressions (meta-models) that relate the stress/strain behavior of the lattice domain and the displacements of the homogeneous domain. The devised meta-models can be integrated with material homogenization to allow the mechanical characterization of large lattice domains.

Chapter 3 proposes an extension of the reconfigurable feature recognition method introduced in [2] that allows the treatment of different curved geometries (using curvature-based filters). It shows an industry-based implementation (including its interactive graphic user interface) and the recognition process results.

Chapter 4 proposes a novel implementation in the domain of a Digital Twin tool. The proposed approach: (1) integrates all phases of design process, (2) does not require an external specialized platform, (3) allows for fast pre-CFD simulation of gerotor performance and (4) compares simulated data vs. measured Gerotor operational data. Finally, relevant conclusions of this work as well as possible future improvements on this research are presented in Chapter 5.

2

Approximation of the Mechanical Response of Large Lattice Domains Using Homogenization and Design of Experiments

Diego Montoya-Zapata[1,2], Diego A. Acosta[3], Camilo Cortés[2], Juan Pareja-Corcho[1,2], Aitor Moreno[2], Jorge Posada[2] and Oscar Ruiz-Salguero[1]

[1] Laboratory of CAD CAM CAE, Universidad EAFIT, Cra 49 no 7-sur-50, Medellín 050022, Colombia

[2] Vicomtech Foundation, Basque Research and Technology Alliance (BRTA), Mikeletegi 57, Donostia-San Sebastian 20009, Spain

[3] Grupo de Diseño y Desarrollo de Procesos (DDP), Universidad EAFIT, Cra 49 no 7-sur-50, Medellín 050022, Colombia

applied sciences

an Open Access Journal by MDPI

IMPACT FACTOR 2.217

Context

Approximation of the Mechanical Response of Large Lattice Domains Using Homogenization and Design of Experiments. Diego Montoya-Zapata, Diego A. Acosta, Camilo Cortes, Juan Pareja-Corcho, Aitor Moreno, Jorge Posada, Oscar Ruiz-Salguero. Journal Applied Sciences, (ISSN 2076-3417; CODEN: ASPCC7), 2020, 10(11), 3858; (This article belongs to the Special Issue Computational and Mathematical Methods in Engineering and Information Science). url= https://www.mdpi.com/2076-3417/10/11/3858, doi= https://doi.org/10.3390/app10113858, Published online: 1 June 2020.

This work is an extension and upgrade of a previous conference publication by the same authors (see below). The editorial board of MACISE - 2020 - 2nd International Conference on Mathematics and Computers in Science and Engineering invited the authors to extend and upgrade the presented paper to be published in a journal as a recognizement for being part of the best papers in the conference.

Diego Montoya-Zapata, Diego A. Acosta, Camilo Cortes, Juan Pareja-Corcho, Aitor Moreno, Jorge Posada, Oscar Ruiz-Salguero. MACISE - 2020 - 2nd Intl. Conf, on Mathematics and Computers in Science and Engineering. January 18-20, 2020. Madrid, Spain. Pages: 308-317. DOI: 10.1109/MACISE49704.2020.00065, URL: https:// ieeexplore.ieee.org/ document/9195607, e-ISBN: 978-1-7281-6695-7, ISBN: 978-1-7281-6696-4, Publisher: IEEE. URL: http://www.macise.org (CPS - Conference Publishing Services).

Indexing: ISI (Q2), SCOPUS (Q1), Publindex (A1)

Abstract

Lattice-based workpieces contain patterned repetition of individuals of a basic topology (Schwarz, ortho-walls, gyroid, etc.) with each individual having distinct geometric grading. In the context of the design, analysis and manufacturing of lattice workpieces, the problem of rapidly assessing the mechanical behavior of large domains is relevant for pre-evaluation of designs. In this realm, two approaches can be identified: (1) numerical simulations which usually bring accuracy but limit the size of the domains that can be studied due to intractable data sizes, and (2) material homogenization strategies that sacrifice precision to favor efficiency and allow the simulation of large domains. Material homogenization synthesizes diluted material properties in a lattice, according to the volume occupancy factor of such a lattice. Preliminary publications show that material homogenization is reasonable in predicting displacements, but is not in predicting stresses (highly sensitive to local geometry). As a response to such shortcomings, this paper presents a methodology that systematically uses Design of Experiments (DOE) to produce simple mathematical expressions (meta-models) that relate the stress/strain behavior of the lattice domain and the displacements of the homogeneous domain. The implementation in this paper estimates the von Mises stress in large Schwarz Primitive lattice domains under compressive loads. The results of our experiments show that (1) material homogenization can approximate efficiently and accurately the displacements field even in complex lattice domains and (2) material homogenization and DOE can produce rough estimations of the von Mises stress in large domains (more than 100 cells). The errors in the von Mises stress estimations reach 42% for domains of up to 24 cells. This result means that *coarse*

stress / strain estimations may be possible in lattice domains by combining DOE and homogenized material properties. This option is not suitable for *precise* stress prediction in sensitive contexts where high accuracy is needed. Future work is required to refine the meta-models to improve the accuracy of the estimations.

Keywords: Design of Experiments, Lattice Structures, Homogenization, Schwarz Primitive, Mechanical Characterization, Modeling and Simulation.

2.1 Introduction

New emerging technologies in the context of Industry 4.0 such as digital twins pose new challenges in the design and simulation in the industrial and biomedical ecosystems. The interactive nature of the processes of Industry 4.0 requires fast simulation methods that enable real-time decision making and digital twin's continuous update with the physical world [3].

Lattice materials have multiple applications in engineering (e.g. energy absorption) and biomedicine (e.g. implants and scaffolds) [4]. However, the simulation of large lattice domains is in many cases unfeasible because: (1) the meshing of these domains is a time consuming process that involves human intervention and (2) the size of the produced meshes is intractable due to the geometric complexity associated to these domains [5, 6].

This manuscript implements a methodology that combines material homogenization and design of experiments (DOE) to estimate the stress/strain response in large lattice domains. The main advantage of this methodology is its inferior computational expense in comparison to finite element analysis (FEA). We apply this approach to approximate the von Mises stress in lattice structures of the type Schwarz Primitive. This manuscript is an extension of the work in [7] which presents a methodology to develop the meta-models using DOE but does not integrate them with material homogenization to produce stress/strain estimations in large lattice domains.

The remainder of this article is organized as follows: Section 2.2 provides a review of the relevant related work. Section 2.3 describes the proposed methodology to estimate the stress/strain response in lattice domains using material homogenization and DOE. Section 2.4 presents and evaluates the results of the implementation of our methodology. Section 2.5 concludes the manuscript and suggests future extensions of the article.

2.2 Literature Review

2.2.1 Lattice Structures and Material Homogenization

Lattice structures are generally composed by replicas of a unit cell that are continuous, uniformly distributed and fill the space. The reason why lattice structures attract the attention of engineers is its ability to retain a good mechanical performance while reducing material usage and weight. For this reason, lattice structures are used for energy absorption, heat transfer and vibration damping applications [4]. Additive manufacturing (AM) has also widen the application range of lattice structures. The manufacturing freedom of AM has promoted the use of lattice structures for materializing the results of structural optimization [8–11] and for biomedical applications in orthopedics and tissue engineering [12, 13].

Material homogenization seeks the equivalent Young's modulus and Poisson's ratio to produce a homogeneous structure that resembles the displacements field of the lattice domain. Material homogenization suppresses the geometrical complexity associated to lattice domains. Therefore, lighter FEA meshes are obtained and, consequently, the computational cost and time of FEA simulations are reduced [8, 14].

Apart of predicting macro-mechanical properties (Young's and Poisson's moduli), material homogenization has allowed the study of periodic strut-like lattice structures built via AM, considering the defects caused during the manufacturing with AM and the stiffening in the joints of the structure [15, 16]. These studies are however limited to strut-like lattice structures. Material homogenization has also been successfully integrated with topology optimization to produce optimal designs of lattice structures suitable for AM [8, 14]. However, since the homogeneous and lattice domains have notorious geometrical differences and stresses/strains depend on the geometry, the stress/strain behavior of the homogeneous domain does not resemble the one of the lattice domain.

2.2.2 Modeling and Simulation of Lattice Structures

The numerical analysis of the mechanical behavior of large lattice structures is challenging due to the high computing (memory and time) requirements [6]. Large lattice structures demand heavy FEA meshes formed by solid elements. Sometimes solid FEA meshes can be simplified using simpler and lighter FEA elements (beams or shells). This approach has allowed the simulation of relatively large domains of a few hundred of cells [6, 17–19]. However, this technique cannot be applied to surface-type lattice structures like Schwarz Primitive lattices, since this kind of architecture cannot be synthesized into long struts or thin plates.

Regarding the joint use of FEA and DOE, we found that they have been combined in several applications in non-lattice structures. The current work can be divided in three groups: (i) material or mechanical properties evaluation, including metallic [20], resins [21] and composite materials [22], (ii) shape optimization on mechanical parts, including medical devices [23] and automobile parts [24], and (iii) generation of meta-models to estimate the stress-strain response in small lattice domains using DOE [7]. However, the produced meta-models are not used for any further analysis with large lattice domains. To the best of our knowledge, the works in the literature do not implement a methodology that integrates systematically material homogenization and DOE for stress/strain estimation in the field of lattice materials.

Monte Carlo methods [25, 26] use random samples in the domains of input variables for an experiment. The experiment is run under the prescribed combination of input variables, and the resulting output values recorded. The model mathematical model for the system or cause/effect is computed on the basis of maximal likeness. In our case, the expenses of running each test are significant since each test requires the preparation and setup of the FEA experiment, the execution itself and its post-processing, along with the analysis of results. This high cost is common to almost all experiments, and leads to choose a minimal (and as possible orthogonal) set of samples of the input set, leading to DOE. This DOE, more economical than the Monte Carlo trials, was chosen for the present work.

2.2.3 Conclusions of the Literature Review

In our literature survey, we found that the geometry of lattice structures implies the use of small FEA elements which produces intractable FEA meshes. Consequently, the numerical analysis of large

lattice structures is a complex (sometimes unfeasible) process, limited by its elevated computational cost.

To alleviate the computational burden of the simulation of lattice structures, material homogenization is applied to produce regular domains that mimic the lattice domain. Following this approach, one can obtain fast and accurate approximations of the displacements field of the lattice domain. However, the stress/strain response cannot be directly obtained due to the geometric dissimilarities between the lattice and the homogeneous domains.

Our goal with this paper is to contribute to the problem of the estimation of the stress/strain response in large lattice domains. For this purpose, we propose a methodology that integrates material homogenization and DOE. We use the DOE-based methodology in [7] to devise simple mathematical expressions (meta-models) to characterize the stress/strain of Schwarz Primitive lattice domains. The inputs of the produced meta-models are displacement-based features that can be efficiently calculated using material homogenization instead of full FEA simulations. The meta-models developed in this article are not intended to be suitable in high precision contexts, but to produce rough and efficient estimations of the von Mises stress that allow fast pre-evaluation of designs.

Particularly, we apply our methodology to estimate the von Mises stress under compressive loads for large (more than 100 cells) Schwarz Primitive lattice structures. The meta-models use the strains of the boundary of the lattice cell to relate the displacement field of the homogeneous domain with the von Mises stress of the lattice domain.

2.3 Methodology

2.3.1 Schwarz Primitive Lattice Structures

Schwarz Primitive lattice structures are obtained by calculating isosurfaces of the real valued function $F : \mathbb{R}^3 \to \mathbb{R}$ in Eq. 2.1:

$$F(x, y, z) = cos\left(\frac{2\pi}{L}x\right) + cos\left(\frac{2\pi}{L}y\right) + cos\left(\frac{2\pi}{L}z\right), \tag{2.1}$$

where L is the desired length of the cell [27].

Schwarz Primitive lattice structures are employed in topology optimization for AM. The result of some common methods in topology optimization is a density map that is impossible to manufacture. The problem of converting that density map into a manufacturable domain does not have an exact solution. The mathematical structure of Schwarz Primitive lattice allow to find approximate solutions to that problem, providing manufacturable designs with smooth transitions in the connections of multiple cells, preventing stress concentration [9]. Moreover, Schwarz Primitive lattice structures are stiffer than other lattice structures (such as the gyroid) [28]. These properties make Schwarz Primitive structures attractive for engineering and biomedical applications [9, 10, 28].

In order to show the geometry of the Schwarz Primitive cell, we obtained the isosurfaces for the isovalues $t = -0.87, 0.0, 0.87$, that is, we found the surfaces that solved the equation $F = t$. The corresponding relative density ρ (i.e. the ratio of the volume of the cell and L^3) of each cell was $\rho = 0.25, 0.5, 0.75$, respectively. Figure 2.1 displays the cells along with their corresponding isovalues and relative densities.

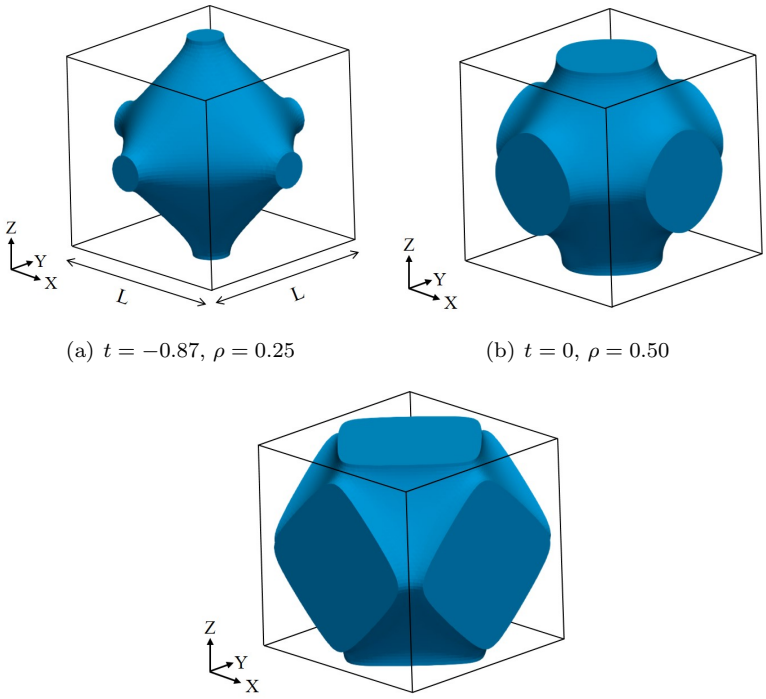

(a) $t = -0.87$, $\rho = 0.25$

(b) $t = 0$, $\rho = 0.50$

(c) $t = 0.87$, $\rho = 0.75$

Figure 2.1: Geometry and relative density of Schwarz Primitive cells for different isovalues.

2.3.2 Methodology to Estimate the Stress/Strain Response of Lattice Structures

In this paper, we propose a methodology for the efficient estimation of the stress/strain response of large lattice structures. The proposed algorithm relies on two main concepts: material homogenization and DOE. The algorithm is divided into four stages: (1) material homogenization of the lattice structure, (2) numerical simulation of the load case using the homogeneous domain, (3) extraction of displacement-based features, and (4) the application of meta-models to estimate the response variable based on the features extracted in (3). Below, we describe every step of our algorithm. Figure 2.2 presents a graphical summary of the proposed methodology, with the inputs and outputs of each phase of the process.

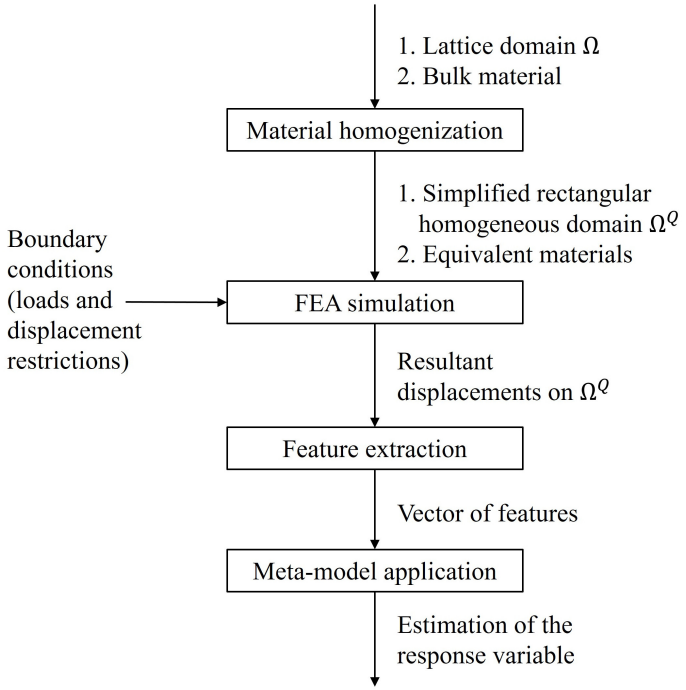

Figure 2.2: Work-flow for the estimation of the mechanical response of lattice domains using material homogenization and DOE.

Material Homogenization

This process seeks to obtain a simplified regular (homogeneous) domain Ω^Q that approximates the heterogeneous lattice structure Ω. The goal is to find an equivalent material $\left(E^Q, \nu^Q\right)$ so that the regular domain equipped with the equivalent material $\left(E^Q, \nu^Q\right)$ resembles the displacement field of the original lattice domain. We implemented the numerical homogenization method presented in [29], which has been applied in the context of lattice structures in [8, 14]. In Section 2.3.3, the reader can find more details on the foundations of material homogenization.

FEA Simulation of the Homogeneous Domain

At this stage, the load case is simulated on the homogeneous domain Ω^Q using analogous boundary conditions. The result of this stage is the displacement field on Ω^Q, which is an approximation of the displacement field on the lattice domain Ω.

Feature Extraction

Characteristic features of every cell of the lattice domain Ω are extracted using the displacement field over the homogeneous domain Ω^Q obtained in the previous step. These displacement-based features extracted at this stage are used as inputs of the meta-models to estimate the stress/strain response of every cell. The definition of these features is central to obtain reliable meta-models and is highly dependent to the expertise of the modeler.

The extracted features condense (or characterize) the deformation of the cell and must provide information about the variable of interest. In this work, we use as features the average normal strain at the flat faces of the boundary of the Schwarz Primitive cells, which can be obtained directly from the displacements on the homogeneous domain Ω^Q. A discussion on how to generate the meta-models using DOE is presented in Section 2.3.4.

Meta-model Execution

A meta-model is a simple mathematical expression (i.e. function) that relates the features extracted in the previous stage and the response variable. In other words, the features extracted in the previous stage (denoted by $\boldsymbol{X} = [x_1, \ldots, x_n]^T$) are used to feed a function $f : \mathbb{R}^n \to \mathbb{R}$ that gives an estimation of the response variable for every cell of the lattice domain. In this article, the meta-models are developed using DOE techniques (see Section 2.3.4).

2.3.3 Material Homogenization

Material homogenization seeks to represent a heterogeneous material with a simple *homogeneous* material. In the case of lattice structures, a lattice unit cell can be treated as a composite material formed by solid (with bulk properties E and ν) and void (with properties E_0 and ν_0) zones [8, 14]. Material homogenization aims to find the material properties (E^Q and ν^Q) that make a filled cube behaves like the unit lattice cell (see Fig. 2.3).

We implemented the numerical homogenization method proposed in [29]. This method finds the elasticity matrix $\boldsymbol{C}^Q$:

$$\boldsymbol{C}^Q = \begin{bmatrix} c_1 & c_2 & c_2 & 0 & 0 & 0 \\ c_2 & c_1 & c_2 & 0 & 0 & 0 \\ c_2 & c_2 & c_1 & 0 & 0 & 0 \\ 0 & 0 & 0 & c_3 & 0 & 0 \\ 0 & 0 & 0 & 0 & c_3 & 0 \\ 0 & 0 & 0 & 0 & 0 & c_3 \end{bmatrix}, \tag{2.2}$$

that relates stresses and strains in the homogeneous material as $\boldsymbol{\sigma} = \boldsymbol{C}^Q \boldsymbol{\varepsilon}$. The corresponding Young E^Q and Poisson ν^Q moduli are provided by the following equations:

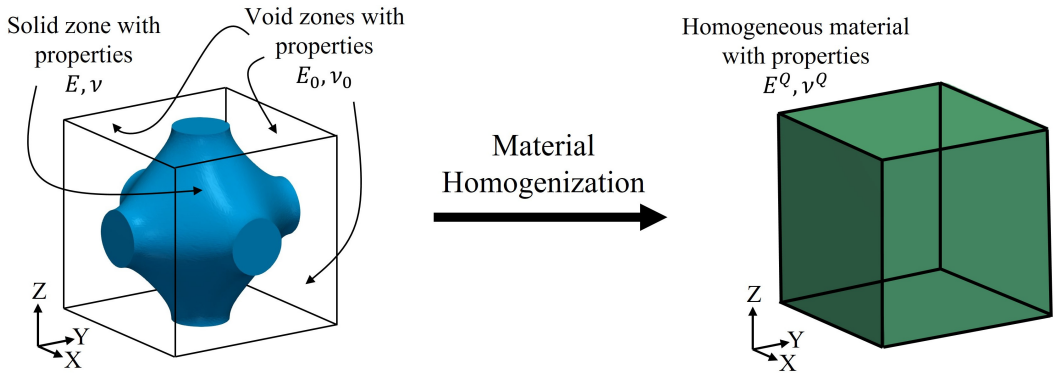

Figure 2.3: Graphical representation of material homogenization.

$$E^Q = \frac{c_1^2 + c_1 c_2 - 2c_2^2}{c_1 + c_2}, \tag{2.3}$$

$$\nu^Q = \frac{c_2}{c_1 + c_2}. \tag{2.4}$$

In this work, we selected the Titanium alloy *Ti-6Al-4V* as bulk material with properties: Young's modulus $E = 114$ GPa and Poisson's ratio $\nu = 0.33$. We applied the homogenization procedure to obtain the diluted properties of Schwarz Primitive cells for the relative densities $\rho \in \{0.25, 0.3, 0.4, 0.5, 0.6, 0.7, 0.8, 0.9\}$. Table 2.1 displays the results obtained. Table 2.1 also includes the case in which the density is $\rho = 1.0$. Notice that the properties of the homogeneous domain coincide with the bulk properties (as expected). When needed, the properties of intermediate densities were obtained via linear interpolation.

Table 2.1: Results of numerical homogenization of Schwarz Primitive cells: Young's modulus and Poisson's ratio.

Relative density (ρ)	Equivalent Young's modulus (E^Q)	Equivalent Poisson's ratio (ν^Q)
0.25	7.5 GPa	0.05
0.3	14.0 GPa	0.09
0.4	24.0 GPa	0.13
0.5	35.0 GPa	0.17
0.6	48.0 GPa	0.21
0.7	61.0 GPa	0.23
0.8	81.0 GPa	0.27
0.9	97.0 GPa	0.29
1.0	114 GPa	0.33

2.3.4 Generation of Meta-models using DOE

DOE is a traditional and effective methodology based on statistical techniques that supports the analysis of complex processes and systems. DOE allows to establish in a systematic way how changes in the parameters of a system or function affect their outcome, minimizing the uncertainty and the number of required experiments to complete such characterization. DOE covers the whole spectrum, from the planing of the experiments to the statistical analysis of the results [30, 31]. We used DOE techniques to develop meta-models to estimate the von Mises stress in Schwarz Primitive lattice structures.

The von Mises stress σ_{VM} is a material failure criterion used in the design and analysis of lattice structures in various works (e.g. [32–34]). The von Mises stress is defined as per Eq. 2.5:

$$\sigma_{VM} = \sqrt{\sigma_1^2 + \sigma_2^2 + \sigma_3^2 - (\sigma_1\sigma_2 + \sigma_1\sigma_3 + \sigma_2\sigma_3)}, \tag{2.5}$$

where $\sigma_1, \sigma_2, \sigma_3$ are the principal stresses. The criterion states that, for preventing failure, the von Mises stress must be below the tensile strength of the material. However, failure in lattice materials is also governed by buckling instabilities that occur before material failure [15]. For the sake of demonstration of the methodology, this work is limited to the estimation of the von Mises stress, although a more complete failure criterion for lattice structures should consider buckling phenomena.

The procedure to devise meta-models using DOE is summarized into three phases: (1) identification of potential features (also called factors) that may affect the variable of interest, (2) selection of the most influential (main) factors, and (3) development of simple mathematical expressions (meta-models) that relates the main factors and the response variable.

We applied DOE to develop meta-models for the von Mises stress in Schwarz Primitive lattice structures of different relative densities. In an ideal case, we should have attained a meta-model for each relative density $\rho \in (0, 1)$. This computing resource demand makes this option unfeasible. Since we were only seeking approximations of the von Mises stress, we found meta-models for the relative densities $\rho = 0.25, 0.50, 0.75, 1.0$. To find the four meta-models, we used lattice domains formed by a single unit cell of the mentioned relative densities. Below, we describe in detail every stage of the procedure.

Factors Identification

The goal at this stage was to detect features (or factors) $F_V = \{f_1, f_2, \cdots, f_n\}$ that (1) were related to the von Mises stress and (2) could be controlled. Additionally, the features had to be based on the displacements over the lattice, so that they could be retrieved from the FEA simulation over the homogeneous domain Ω^Q.

Our set of factors were initially the strains at the flat faces (extreme faces) of the boundary of each unit cell of the Schwarz Primitive lattice domain. For convenience, the flat faces of the boundary were denoted as $\{X, -X, Y, -Y, Z, -Z\}$. $\{-X, -Y, -Z\}$ were the flat faces at $x = 0, y = 0, z = 0$. $\{X, Y, Z\}$ were the flat faces at $x = L, y = L, z = L$. We defined the strains at the flat faces as:

$$\begin{aligned} \varepsilon_{ij} &= \mathrm{sgn}(i) \cdot \frac{U_{ij} - U_{-jj}}{L}, \\ i &= \pm X, \pm Y, \pm Z, \quad j = x, y, z, \end{aligned} \tag{2.6}$$

where U_{ij} represented the average displacement in j direction of the face i. For instance, U_{-Xx} was the displacement in x direction of the flat face at $x = 0$. The normal strains at the flat faces corresponded to $\{\varepsilon_{-Xx}, \varepsilon_{Xx}, \varepsilon_{-Yy}, \varepsilon_{Yy},$
$\varepsilon_{-Zz}, \varepsilon_{Zz}\}$. However, from Eq. 2.6, $\varepsilon_{-Xx} = \varepsilon_{-Yy} = \varepsilon_{-Zz} = 0$, which prevented the introduction of false strains due to pure translation of the Schwarz Primitive cell.

In Eq. 2.5 we can see that the von Mises stress depends on the shear stress and, therefore, it is influenced by the shear strain. We conducted preliminary tests considering shear strains at the flat faces of the cell but our results overestimated the von Mises stress by a large factor. We found that the shear strain interaction is not fully understood at the level of DOE. Consequently, our set of factors was reduced to the normal strains at the flat faces of the cell $\{\varepsilon_{Xx}, \varepsilon_{Yy}, \varepsilon_{Zz}\}$.

Factors Selection

In the context of DOE, the goal at this stage is to reduce the number of considered factors, selecting those factors that affect the most the response variable. Mature techniques do exist for this task, such as full or fractional factorial or Plackett-Burman designs [30,31]. However, we considered only 3 factors, so we decided to develop the meta-models using all of them.

Meta-model Development

The goal at this stage was to develop efficient and simple mathematical expressions that expressed the von Mises stress in Schwarz Primitive lattice domains in terms of $\{\varepsilon_{Xx}, \varepsilon_{Yy}, \varepsilon_{Zz}\}$.

We used Response Surface methodologies, specifically central composite face-centered design (CCF), to efficiently devise the meta-models. The shape of the devised meta-models for Schwarz Primitive cells of relative densities $\rho \in \{0.25, 0.5, 0.75\}$ was

$$\hat{y} = \left(\beta_0 + \sum_{i \leq j} \beta_{ij} \varepsilon_{ii} \varepsilon_{jj}\right)^2, \tag{2.7}$$

and the shape of the meta-model for $\rho = 1.0$ was

$$\hat{y} = \sqrt{\beta_0 \left(\sum_i \varepsilon_{ii}^2 - \sum_{i<j} \varepsilon_{ii} \varepsilon_{jj}\right)}. \tag{2.8}$$

We used `R` [35] to perform the regression analysis to estimate the coefficients (β_i, β_{ij}) of the meta-models (see Table 2.2).

To evaluate the meta-models, we ran 100 random simulations for each of the four domains and compared the experimental (result of FEA) and predicted (result of the meta-model) von Mises stress. The values of the Young's modulus and Poisson's ratio used for the simulations with the homogeneous domains were the ones reported in Table 2.1. For the cell of density $\rho = 0.75$, we used $E^Q = 71.0$ GPa and $\nu^Q = 0.25$, which resulted by interpolating the corresponding moduli of the cells of densities $\rho = 0.7$ and $\rho = 0.8$. We used the displacements on the homogeneous domains to calculate the normal strains at the flat faces ε_{ij} and used them as inputs for the meta-models in Eqs. 2.7 and 2.8.

Table 2.2: Values of the coefficients β in the fitted meta-models. Average and maximum relative errors between FEA and our approach for 100 random simulations.

Relative density	β_0	β_{12}	β_{13}	β_{23}	β_{11}	β_{22}	β_{33}	Average relative error	Max. relative error
0.25	0.0438	0.0010	0.0013	0.0005	0.0089	0.0075	0.0067	19%	370%
0.50	0.0369	0.0019	0.0021	0.0019	0.0076	0.0073	0.0074	20%	298%
0.75	0.0419	0.0041	0.0039	0.0036	0.0089	0.0098	0.0091	21%	255%
1.0	0.4036	N/A	N/A	N/A	N/A	N/A	N/A	0%	0%

The boundary conditions imposed on the four domains were prescribed displacements in the normal direction of the flat faces of the domains. The size of the cell used was $L = 1.0$ cm, so that the imposed displacements were equivalent to normal strains at the flat faces (ε_{ij}).

Our analysis was limited to the elastic zone of the material. The range of the variables was $\varepsilon_{ij} \in 10^{-5} \times [-1.0, 1.0]$. The value of the variables was coded in the range $[-1, 1]$ to be in concordance with the procedures found in the literature [31]. To ensure that the strains in the flat faces were in the working range $\left(\varepsilon_{ij} \in 10^{-5} \times [-1.0, 1.0]\right)$ and to explore it evenly, the values of the imposed normal strains at the flat faces were generated from a uniform distribution in the interval $(-1.0 \times 10^{-5}, 1.0 \times 10^{-5})$.

Figure 2.4 displays the aforementioned comparison for each cell. We can see that the meta-models for the densities $\rho \in \{0.25, 0.50, 0.75\}$ tend to overestimate the von Mises stress at low stress conditions. This is due to the term β_0 in Eq. 2.7, which impedes the meta-model to predict small values of von Mises stress. Table 2.2 gives the average and maximum relative error of the predicted vs. the experimental von Mises stress. The maximum relative errors are associated to low stress conditions, mainly influenced by the value of β_0 in Eq. 2.7 (as previously discussed). It is clear that the meta-models are not well-suited for low stress conditions. The average and maximum relative errors in the estimations show that this methodology is not applicable in very sensitive processes where high accuracy is required.

2.4 Results

2.4.1 Validation of the Proposed Methodology

To evaluate our methodology, we compared the results of the FEA simulation and our methodology for six Schwarz Primitive lattice domains. Three of the six domains (Figs. 2.4.1–2.4.1) were formed by 8 unit cells of uniform density $\rho = 0.25, 0.50, 0.75$, respectively. The other three domains were formed by unit cells of graded density, that is, the isovalue t was not a constant but a function $t : \mathbb{R}^3 \to \mathbb{R}$. The resultant surfaces are the solutions to the equation $F(x, y, z) = t(x, y, z)$ (see Eq. 2.1). The domain of 24 unit cells in Fig. 2.4.1 was taken from Ref. [9] and corresponded to the result of mapping the results of topology onto Schwarz Primitive cells [9]. The domains of 8 cells displayed in Figs. 2.4.1–2.4.1 were also taken from [9]. The isovalue functions associated with these two domains are:

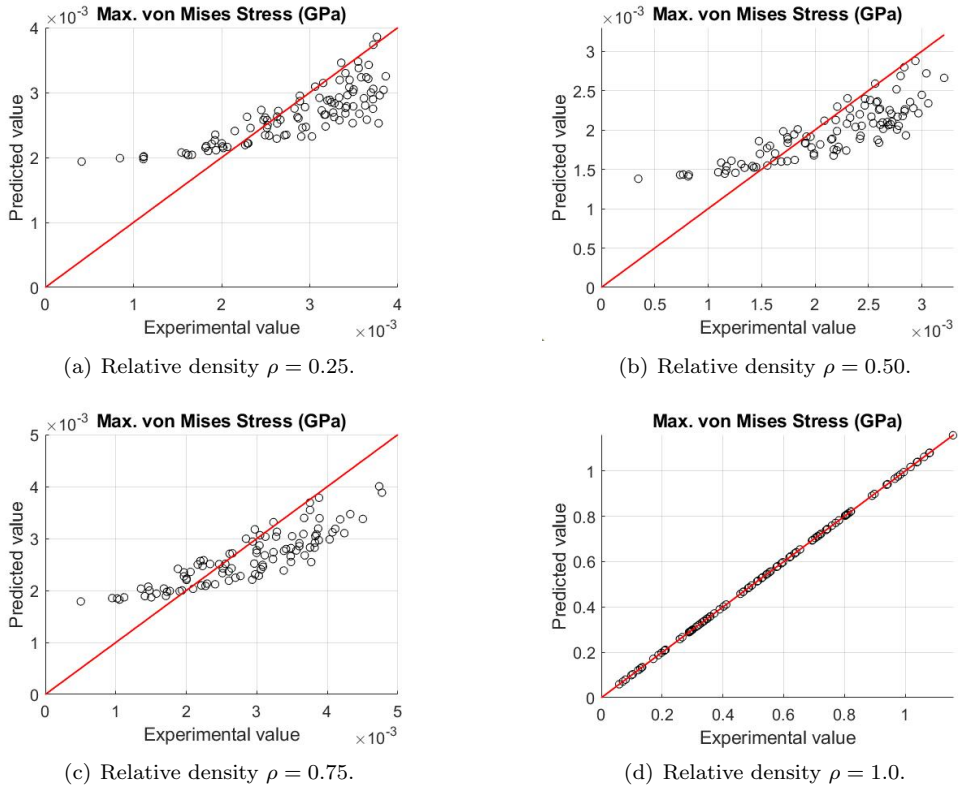

(a) Relative density $\rho = 0.25$.

(b) Relative density $\rho = 0.50$.

(c) Relative density $\rho = 0.75$.

(d) Relative density $\rho = 1.0$.

Figure 2.4: Evaluation of the meta-models to estimate the von Mises stress in Schwarz Primitive lattices. Fitted values vs. Experimental values.

$$t(x,y,z) = \begin{cases} -\frac{5}{2}\left(\frac{3x}{2L}\right)^2 + 2 & ,0 \leq x \leq \frac{2L}{3}, y, z \in \mathbb{R} \\ -\frac{1}{2} & ,\frac{2L}{3} < x \leq \frac{4L}{3}, y, z \in \mathbb{R} \\ \frac{3}{2L}x - \frac{5}{2} & ,\frac{4L}{3} < x \leq 2L, y, z \in \mathbb{R} \end{cases} \tag{2.9}$$

$$t(x,y,z) = 3\left(\frac{x}{L} - 1\right)^2 - \frac{1}{2}, \quad 0 \leq x \leq 2L., y, z \in \mathbb{R} \tag{2.10}$$

The six domains were subjected to uniaxial compression (see Fig. 2.5). The magnitude of the load was such that the resultant strains in the flat faces of the boundary of the cells lied in the range of analysis $\varepsilon_{ij} \in 10^{-5} \times [-1.0, 1.0]$. First, we compared the displacements field of the lattice and homogeneous domain (Section 2.4.1). Secondly, we applied our DOE-based methodology using the displacement results from the homogeneous domain to get the maximum von Mises stress in every cell. Finally, we compared the maximum von Mises stress obtained via (1) direct FEA of the lattice domain and (2) our proposed methodology (Section 2.4.1).

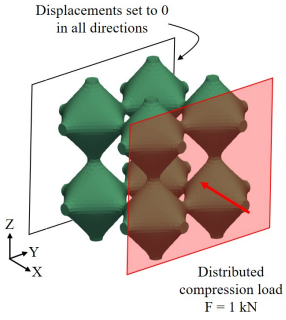

[8 cells. Uniform density $\rho = 0.25$.]

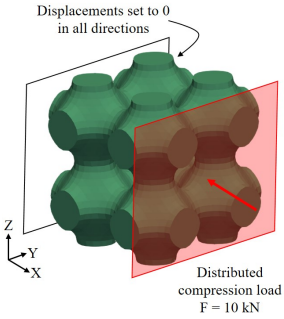

[8 cells. Uniform density $\rho = 0.50$.]

[8 cells. Uniform density $\rho = 0.75$.]

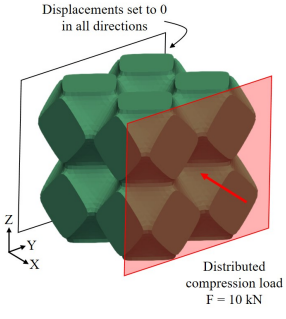

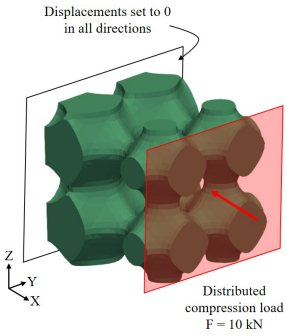

[8 cells. Graded density as per Eq. 2.9.]

[8 cells. Graded density as per Eq. 2.10.]

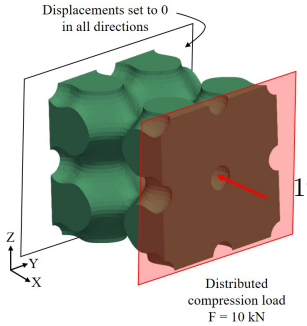

[24 cells. Graded density as per Ref. [9].]

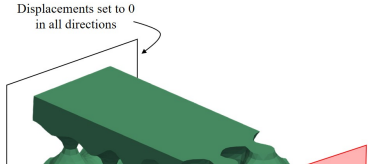

The FEA simulations of the lattice and homogeneous domains were executed in ANSYS. The lattice models were meshed in ANSYS using tetrahedral elements (`SOLID285`). The material properties of the lattice models correspond to the bulk material properties ($\rho = 1.0$ in Table 2.1). On the other hand, given the regular shape of the homogeneous domains, we used cubic elements (`SOLID185`) for the respective meshes. Each cubic sub-domain was isotropic and its material properties were assigned according to its relative density and the properties reported in Table 2.1. The homogeneous domain was then a regular 3D array of isotropic cubic sub-domains. Since the properties of each sub-domain could be different, the homogeneous domain resulted to be anisotropic.

FEA simulations were executed using different hardware settings and different operative systems, therefore, it was not possible to compare execution times between different simulations in equal conditions. To overcome this difficulty, we used the number of elements in the mesh as a measurement of computational expense in each domain. The number of elements required for each lattice and homogeneous domain are reported in Fig. 2.6 and Table. 2.3. It is noticeable that the FEA meshes of lattice domains required more elements than the homogeneous domains. Another important aspect to highlight is that the number of elements of the homogeneous domain only depend on the number of cells (particularly, we chose a mesh of $10 \times 10 \times 10$ elements per unit cell). On the other hand, the number of elements for the lattice domains does not completely depend on the number of cells. Notice that 5 out of the 6 domains are conformed by 8 unit cells. However, the number of elements (Fig. 2.6 and Table. 2.3) is different for each domain. These variations are mainly influenced by the shape of the domain, which affects the corresponding meshing algorithms of the FEA software (ANSYS).

After conducting the FEA simulations, we proceeded to compare the resultant displacements of the lattice and homogeneous domains. Figure 2.8 (1) contrasts the nodal displacement in the load direction X for the six load cases and (2) shows the absolute difference between the X displacement predicted by the lattice and homogeneous approaches. The reader may observe the similarity in

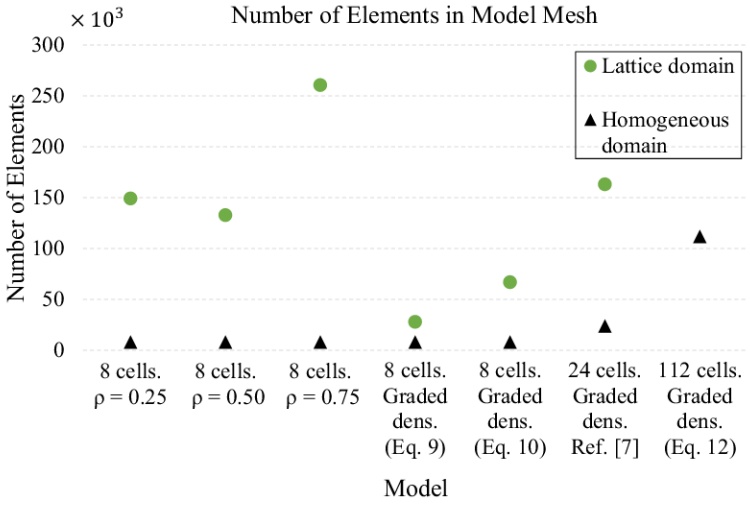

Figure 2.6: Number of elements in the FE meshes of lattice and simplified homogeneous domains.

both the distribution and magnitude of the displacements field of the lattice and homogeneous domains. Figure 2.8 also shows that the maximum value of the absolute error is in all cases approximately 10 times smaller than the maximum displacement. From these results we conclude that material homogenization is an accurate tool to estimate the displacements in lattice structures and its efficiency allow its application in large lattice domains.

Table 2.3: Number of elements in FE meshes of lattice and simplified homogeneous domains.

Domain	Figure number	No. of elements in Lattice domain	No. of elements in Homogeneous domain
8 cells. Uniform density with $\rho = 0.25$	Fig. 2.4.1	149090	8000
8 cells. Uniform density with $\rho = 0.50$	Fig. 2.4.1	132710	8000
8 cells. Uniform density with $\rho = 0.75$	Fig. 2.4.1	260610	8000
8 cells. Graded density as per Eq. 2.9	Fig. 2.4.1	27863	8000
8 cells. Graded density as per Eq. 2.10	Fig. 2.4.1	66890	8000
24 cells. Graded density as per Ref. [9]	Fig. 2.4.1	163080	24000
112 cells. Graded density as per Eq. 2.12	Fig. 2.11(a)	N/A	112000

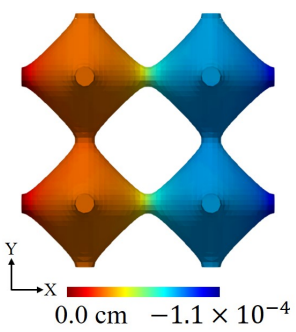

(a) $\rho = 0.25$. Min. displacement: -1.1×10^{-4} cm.

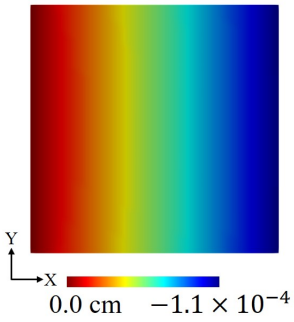

(b) $\rho = 0.25$. Min. displacement: -1.1×10^{-4} cm.

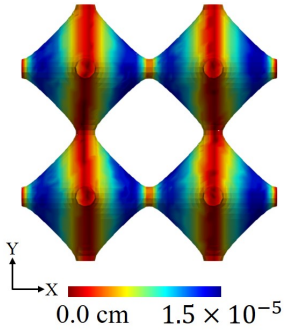

(c) $\rho = 0.25$. Absolute error.

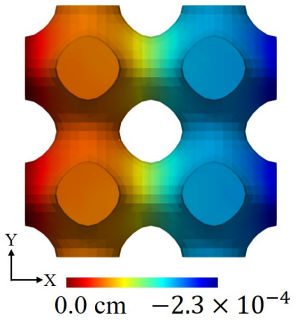

(d) $\rho = 0.50$. Min displacement: -2.3×10^{-4} cm.

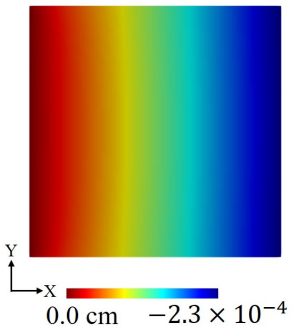

(e) $\rho = 0.50$. Min displacement: -2.2×10^{-4} cm.

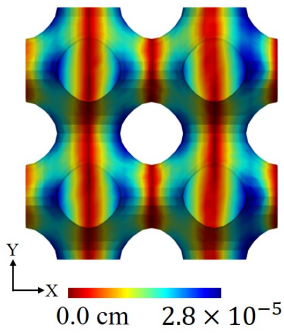

(f) $\rho = 0.50$. Absolute error.

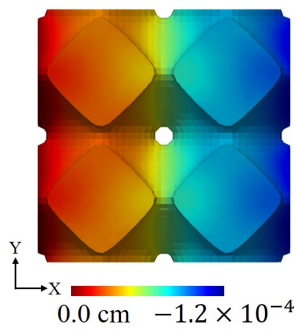

(g) $\rho = 0.75$. Min displacement: -1.2×10^{-4} cm.

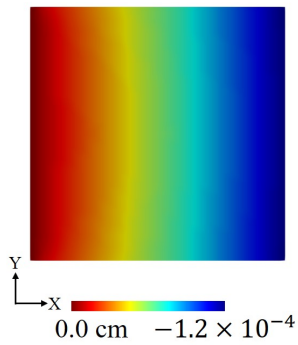

(h) $\rho = 0.75$. Min displacement: -1.1×10^{-4} cm.

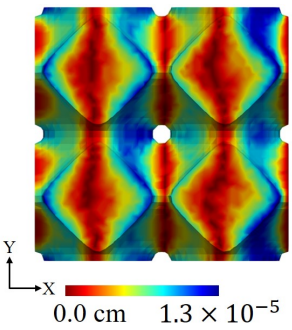

(i) $\rho = 0.75$. Absolute error.

Figure 2.7: *Cont.*

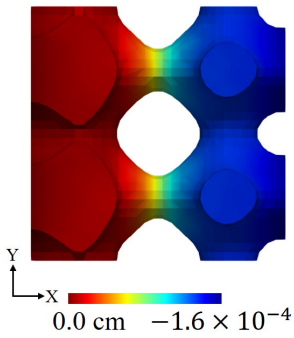

(j) Graded density Eq. 2.9. Min displacement: -1.6×10^{-4} cm.

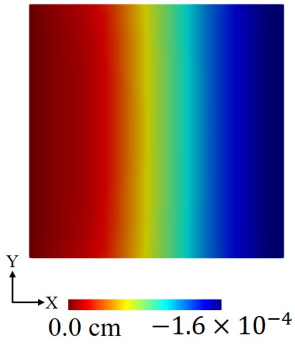

(k) Graded density Eq. 2.9. Min displacement: -1.6×10^{-4} cm.

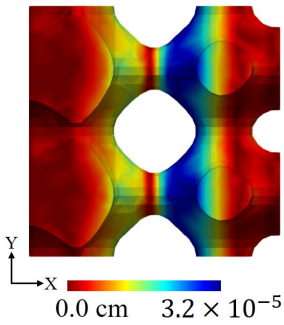

(l) Graded density Eq. 2.9. Absolute error.

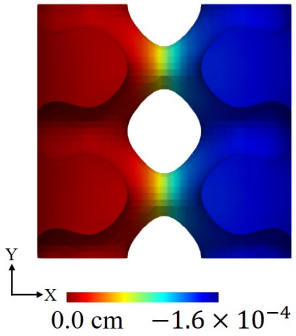

(m) Graded density Eq. 2.10. Min. displacement: -1.6×10^{-4} cm.

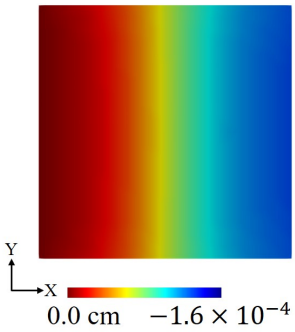

(n) Graded density Eq. 2.10. Min. displacement: -1.3×10^{-4} cm.

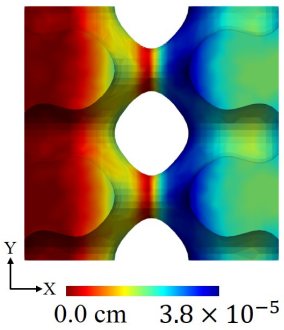

(o) Graded density Eq. 2.10. Absolute error.

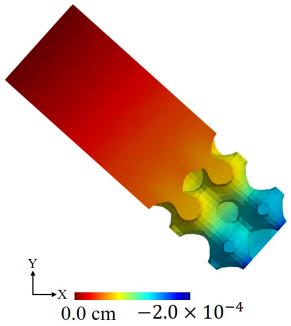

(p) Graded density Ref. [9]. Min displacement: -1.8×10^{-4} cm.

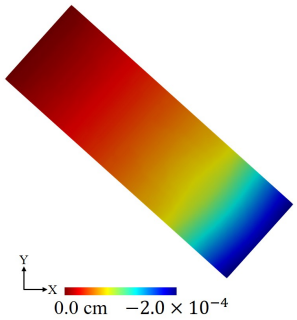

(q) Graded density Ref [9]. Min displacement: -2.0×10^{-4} cm.

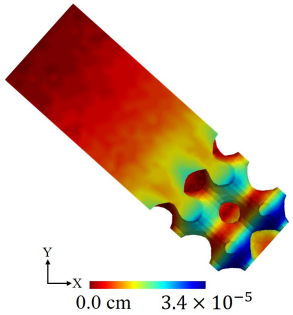

(r) Graded density Ref [9]. Absolute error.

Figure 2.8: Results of X compression test. X displacement. Comparison of lattice ((a), (d), (g), (j), (m), (p)) vs. homogeneous ((b), (e), (h), (k), (n), (q)) domains. Absolute error distribution ((c), (f), (i), (l), (o), (r)). Domains of 8 cells (a)-(o). Domain of 24 cells (p)-(r).

Comparison between FEA and Our Methodology

We used the displacements on the homogeneous domains obtained in the previous stage to extract the inputs of our meta-models: the normal strains on the boundary of each cell. Then, we used the meta-models presented in Section 2.3.4 to estimate the maximum von Mises stress in each cell. To apply the meta-models, we calculated the average relative density of each cell of the non-uniform (graded) density domains. Since we had only meta-models for the relative densities $\rho \in \{0.25, 0.50, 0.75, 1.0\}$, we used linear interpolation to do the approximations for the intermediate values of density ρ. For instance, $\left(\sigma_{VM}^{(0.4)}\right)$, the von Mises stress for a relative density $\rho = 0.4$ is approximated as

$$\sigma_{VM}^{(0.4)} = \frac{2}{5}\sigma_{VM}^{(0.25)} + \frac{3}{5}\sigma_{VM}^{(0.5)}, \tag{2.11}$$

where $\sigma_{VM}^{(0.25)}$ and $\sigma_{VM}^{(0.50)}$ denote the von Mises stresses for the cells of densities $\rho = 0.25$ and $\rho = 0.50$. $\sigma_{VM}^{(0.25)}$ and $\sigma_{VM}^{(0.50)}$ are retrieved using Eq. 2.7 with the corresponding coefficients of Table 2.2.

Figures 2.9 and 2.10 show (i) the von Mises stress of the FEA simulation, (ii) the maximum von Mises stress of every cell retrieved from the FEA simulation of the lattice domain, and (iii) the maximum von Mises stress of every cell calculated with our methodology. In addition, Table 2.4 lists, for each domain, the global maximum von Mises stress using (a) FEA simulation of the lattice domain and (b) our methodology. We measured the relative error of our methodology with respect to the FEA simulation of the lattice domain. These results are reported also in Table 2.4.

In Figures 2.9 and 2.10, we can see that the maximum von Mises stress given by our methodology (third column of the figures) is very uniform along all the cells. When compared with the maximum von Mises stress of the FEA methodology (second column of the figures), it is clear that our methodology is not able to capture all the variation of the maximum von Mises stress per cell (see Figs. 2.10(h) and 2.10(i)). However, we can see the correspondence between the most stressed zones using FEA simulation and our methodology. Note that our implementation often predicts the most stressed cell.

In terms of the accuracy of our methodology, we can see in Table 2.4 that (1) the error in the estimations with our methodology is between 16% and 42% and (2) our methodology tends to underestimate the maximum von Mises stress. These results show that our methodology can only do rough estimations (with errors above 20%) of the maximum von Mises stress in Schwarz lattice structures.

We have identified three critical aspects that can improve the accuracy of our methodology:

1. To consider more displacement-based features located inside the cell, not only on the boundary of the cell.

2. To develop meta-models for more relative densities. Currently, it is limited to meta-models of density $\rho \in \{0.25, 0.50, 0.75, 1.0\}$.

3. To enlarge the range of analysis of the displacement-based features, since in a single load case, the magnitude of the deformation of the lattice domain varies in every zone. Currently, the allowed normal strains are currently limited to the interval $10^{-5} \times [-1.0, 1.0]$.

Table 2.4: Maximum von Mises stress values of direct FEA of the lattice domain vs. our methodology.

Domain	Figure number	Max. σ_{VM}: FEA (MPa)	Max. σ_{VM}: our method (MPa)	Rel. error
8 cells. Uniform density with $\rho = 0.25$	Fig. 2.4.1	3.6	2.4	33%
8 cells. Uniform density with $\rho = 0.50$	Fig. 2.4.1	4.5	3.6	20%
8 cells. Uniform density with $\rho = 0.75$	Fig. 2.4.1	3.4	2.4	29%
8 cells. Graded density as per Eq. 2.9	Fig. 2.4.1	3.1	3.6	16%
8 cells. Graded density as per Eq. 2.10	Fig. 2.4.1	3.4	2.8	17%
24 cells. Graded density as per Ref. [9]	Fig. 2.4.1	3.1	1.8	42%

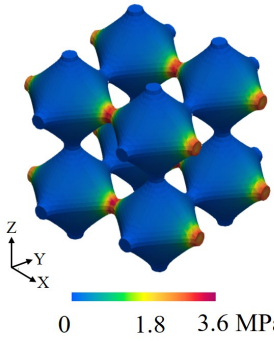

(a) Lattice domain, $\rho = 0.25$. Von Mises stress.

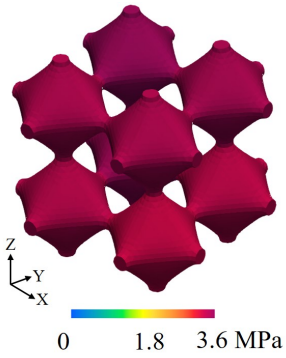

(b) Lattice domain, $\rho = 0.25$. Max. von Mises stress per cell.

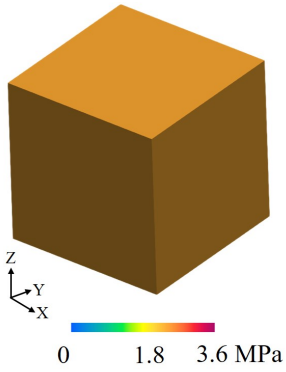

(c) Homogeneous domain, $\rho = 0.25$. Max. von Mises stress per cell.

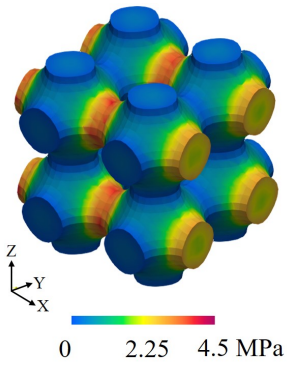

(d) Lattice domain, $\rho = 0.50$. Von Mises stress.

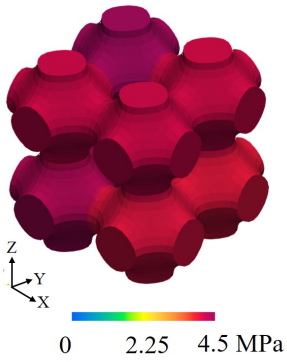

(e) Lattice domain, $\rho = 0.50$. Max. von Mises stress per cell.

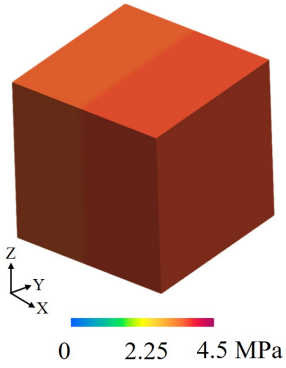

(f) Homogeneous domain, $\rho = 0.50$. Max. von Mises stress per cell.

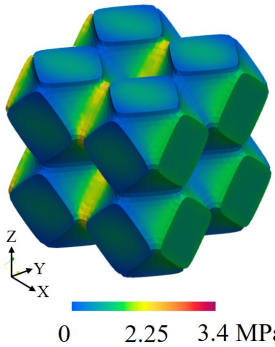

(g) Lattice domain, $\rho = 0.75$. Von Mises stress.

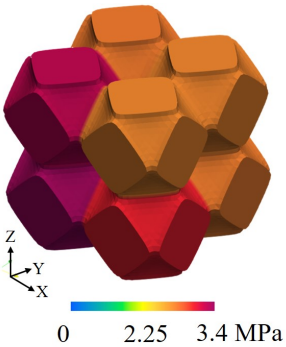

(h) Lattice domain, $\rho = 0.75$. Max. von Mises stress per cell.

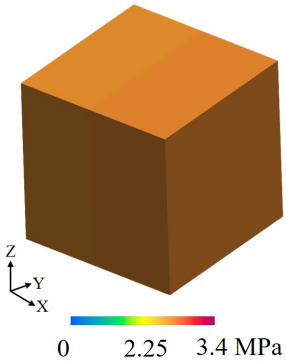

(i) Homogeneous domain, $\rho = 0.75$. Max. von Mises stress per cell.

Figure 2.9: Comparison of the maximum von Mises stress in direct FEA (lattice) and our methodology for Schwarz Primitive structures. 8 cells domains of uniform density. Detailed results in Table 2.4.

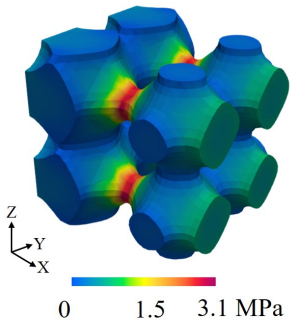

(a) Lattice domain. Graded density Eq. 2.9. Von Mises stress.

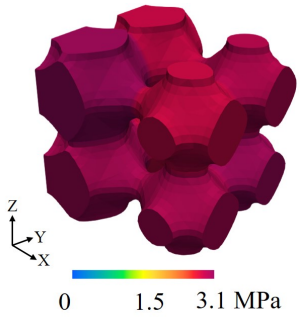

(b) Lattice domain. Graded density Eq. 2.9. Max. von Mises stress per cell.

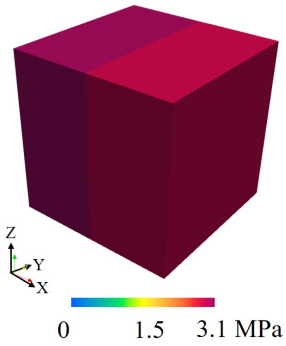

(c) Homogeneous domain. Graded density Eq. 2.9. Max. von Mises stress per cell.

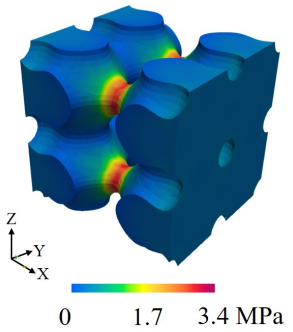

(d) Lattice domain. Graded density Eq. 2.10. Von Mises stress.

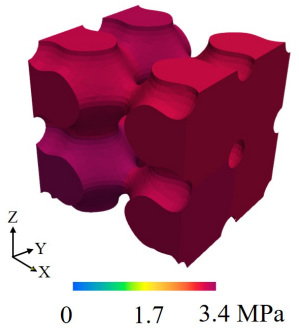

(e) Lattice domain. Graded density Eq. 2.10. Max. von Mises stress per cell.

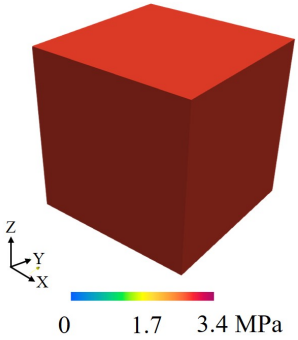

(f) Homogeneous domain. Graded density Eq. 2.10. Max. von Mises stress per cell.

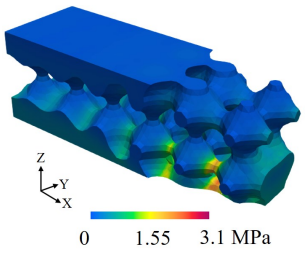

(g) Lattice domain. Graded density Ref. [9]. Von Mises stress.

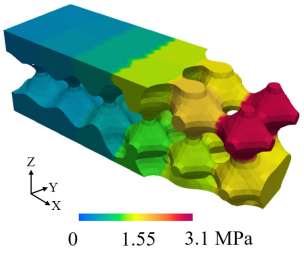

(h) Lattice domain. Graded density Ref. [9]. Max. von Mises stress per cell.

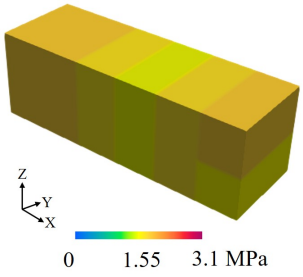

(i) Homogeneous domain. Graded density Ref. [9]. Max. von Mises stress per cell.

Figure 2.10: Comparison of the maximum von Mises stress in direct FEA (lattice) and Our Methodology (homogeneous) for Schwarz Primitive domains of graded density. Domains of 8 cells (a)-(f). Domain of 24 cells (g)-(i). Detailed results in Table 2.4.

2.4.2 Application of Our Methodology to Large Lattice Domains

To demonstrate the potential of our methodology to be applied in the roughly estimation of the von Mises stress in larger lattice structures, we generated a domain of 112 ($7 \times 4 \times 4$) cells of graded density. We tested it under uniaxial compression in X direction (Fig.2.11(a)). The isovalue function associated to this domain is:

$$t(x, y, z) = 2.5 - \frac{0.3}{L}(x + y). \tag{2.12}$$

First, we produced the homogeneous domain and conducted the FEA simulation. The number of elements of the mesh was 112000 ($10 \times 10 \times 10$ elements per cell). Secondly, using the displacements field (Fig. 2.11(b)), we extracted the normal strains on the boundary of each of the 112 cells. Finally, we used the meta-models of Section 2.3.4 along with linear interpolation to estimate the maximum von Mises stress in each cell. The results of this estimation are shown in Fig. 2.11(c).

Due to the large number of cells (117), the FEA directly on the lattice domain was unfeasible. However, it is possible to show the computational efficiency of our approach: to mesh a lattice domain of 24 cells, 160k elements were required (6.6k elements per cell), while for the homogeneous domain of 112 cells, 112k elements were used (1.0k elements per cell). This example has shown the computational efficiency of our approach in comparison with direct FEA simulation. It shows that our approach has the potential to be employed in the estimation of the stress/strain response of large lattice domains.

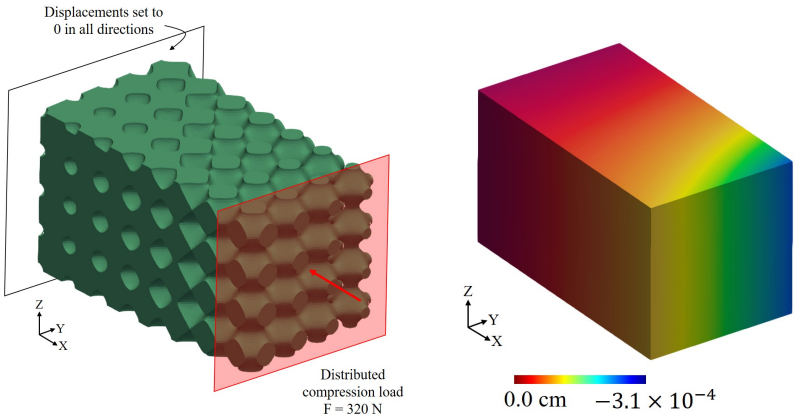

(a) Lattice domain. Boundary conditions.

(b) Homogeneous domain. Displacement in X direction.

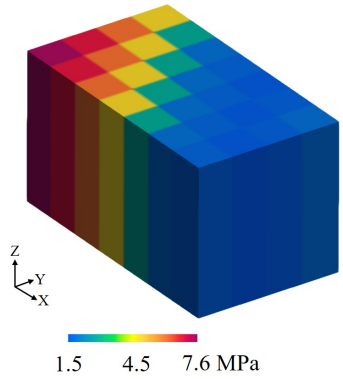

(c) Homogeneous domain. Max. von Mises stress per cell.

Figure 2.11: Application of our methodology to a large Schwarz Primitive domain of 112 cells of graded density as per Eq. 2.12.

2.5 Conclusions

In this article we present a methodology that integrates material homogenization and design of experiments (DOE) to estimate the stress/strain response in large lattice domains reducing the computational cost with respect to direct FEA simulation. On the one hand, material homogenization is used to efficiently approximate the displacements on the lattice domains. On the other hand, DOE is applied to produce simple mathematical expressions to express the stresses in the lattice as functions of the displacements obtained through homogenization. In comparison with related approaches, this methodology is easy to implement, can be applied with different families of lattices (strut or surface based) and offers an efficient alternative to retrieve the stress/strain response of complex lattice domains. However, it is less accurate and produces only rough estimations.

We implemented the proposed methodology to estimate the von Mises stress in Schwarz Primitive lattice structures. Material homogenization proved its suitability for the approximation of the displacements in large lattice domains. Results have also shown that the proposed methodology is an efficient tool with potential applications in the *coarse* estimation of the von Mises stress in large lattice domains. The average errors in the estimations are between 20% and 40%, which *are not acceptable* in sensitive processes where high accuracy is required. However, these results are encouraging when it is considered that we estimated meta-models for only four densities ($\rho \in \{0.25, 0.50, 0.75, 1.0\}$) for a narrow range of strains on the boundary of the cells $10^{-5} \times [-1.0, 1.0]$. Our methodology has shown potential for the pre-evaluation of designs, where less precision is needed.

The methodology presented in this paper can be applied to other types of lattice structures (different to the Schwarz Primitive). It would be necessary to develop meta-models for the lattice structure of interest and, consequently, to perform material homogenization to obtain the Young's and Poisson's moduli associated to the relative density.

2.5.1 Future Work

Future work is needed to improve the accuracy of the estimations of the von Mises stress. Efforts should be focused on the fitting of more robust meta-models that use more information from the displacements field obtained via material homogenization.

This paper considers the von Mises stress as a failure criterion for lattice domains. However, lattice structures at low densities experience buckling instabilities. This phenomenon should be considered to analyze failure in lattice structures.

Author Contributions: D.M-Z., D.A.A. and O.R-S. conceptualized and designed the algorithm. D.M-Z.and J.P-C. implemented the algorithm and executed the simulations. D.A.A. and A.M. supervised the Design of Experiments and Statistical aspects of this research. C.C., J.P and O.R.-S. supervised the Computational Geometry and Computational Mechanics aspects of this research. All the authors contributed to the writing of the article.

Funding: This research received no external funding.

Conflicts of Interest: The authors declare no conflict of interest.

3

Reconfigurable 3D CAD Feature Recognition Supporting Confluent n-Dimensional Topologies and Geometric Filters for Prismatic and Curved Models

Juan Pareja-Corcho[1,2], Oscar Betancur-Acosta[3], Jorge Posada[2], Antonio Tammaro[2], Oscar Ruiz-Salguero[1] and Carlos Cadavid[4]

[1] Laboratory of CAD CAM CAE, Universidad EAFIT, Cra 49 no 7-sur-50, 050022 Medellín, Colombia

[2] Vicomtech Foundation, Basque Research and Technology Alliance (BRTA), Mikeletegi 57, 20009 Donostia-San Sebastian, Spain

[3] Integration and Engineering Construction Services S.A. de C.V., Av. Eugenio Garza Sada Sur 427, Alta Vista, 64840 Monterrey, Mexico

[4] Mathematics and Applications Group, Department of Mathematical Sciences, Universidad EAFIT, Cra 49 no 7-sur-50, 050022 Medellín, Colombia

an Open Access Journal by MDPI

Context

Reconfigurable 3D CAD Feature Recognition Supporting Confluent n-Dimensional Topologies and Geometric Filters for Prismatic and Curved Models. Juan Pareja-Corcho, Oscar Betancur-Acosta, Jorge Posada, Antonio Tammaro,Oscar Ruiz-Salguero, Carlos Cadavid. Journal Mathematics, MDPI, ISSN 2227-7390, 2020, 8(8), 1356 (This article belongs to the Special Issue Modern Geometric Modeling: Theory and Applications). url= https://www.mdpi.com/2227-7390/8/8/1356, doi= https://doi.org/10.3390/math8081356, Published online: 13 August 2020.

Indexing: ISI (Q1), SCOPUS (Q3), Publindex (A1)

Abstract

Feature Recognition (FR) in Computer-aided Design (CAD) models is central for Design and Manufacturing. FR is a problem whose computational burden is intractable (NP-hard), given that its underlying task is the detection of graph isomorphism. Until now, compromises have been reached by only using FACE-based geometric information of prismatic CAD models to prune the search domain. Responding to such shortcomings, this manuscript presents an interactive FR method that more aggressively prunes the search space with reconfigurable geometric tests. Unlike previous approaches, our reconfigurable FR addresses curved EDGEs and FACEs. This reconfigurable approach allows enforcing arbitrary confluent topologic and geometric filters, thus handling an expanded scope. The test sequence is itself a graph (i.e., not a linear or total-order sequence). Unlike the existing methods that are FACE-based, the present one permits combinations of topologies whose dimensions are two (SHELL or FACE), one (LOOP or EDGE), or 0 (VERTEX). This system has been implemented in an industrial environment, using icon graphs for the interactive rule configuration. The industrial instancing allows industry based customization and itis faster when compared to topology-based feature recognition. Future work is required in improving the robustness of search conditions, treating the problem of interacting or nested features, and improving the graphic input interface.

Keywords: Computer-aided Design; Computer-aided Manufacturing; feature recognition; 3D CAD.

3.1 Introduction

Computer-aided Process Planning (CAPP) refers to the use of computational tools to automate and optimize the manufacturing planning process of an industrial product. To automatically determine the manufacturing techniques to be used in a certain product, it becomes necessary to be able to efficiently extract geometric features from the standarized version of the Computer-aided Design (CAD) model, a process known as Automated Feature Recognition".

An essential part in the efforts in CAD-CAPP systems research is the development of efficient and effective automated feature recognition algorithms. Features can describe form (form features), tolerances and finishing (precision features) or material treatment, and grade and properties (manufacturing features). Feature recognition algorithms focus on successfully identifying a region of a part with some interesting geometric or topological properties (form features). Precision and manufacturing features are out of the scope of such algorithms. Given that feature recognition is a problem whose computational burden is intractable (NP-hard)[36], geometric information from the CAD-based part model is used to prune the search space.

A number of feature recognition algorithms have been successfully implemented on boolean combinations of prismatic shapes, but most of the current algorithms fail to treat curved geometries and interacting features. This manuscript presents an extension of the reconfigurable feature recognition method introduced in [2] to allow for the treatment of different curved geometries using curvature-based filters. We also show an industry-based implementation (including its interactive graphic user interface) and the recognition process results.

In this manuscript, Section 3.1 introduces the industrial relevance of the problem and reviews the available relevant literature, highlighting the advantages and disadvantages of the existing methods of Feature Recognition. Section 3.2 presents and discusses the Methodology implemented, including the performance comparison with respect to other methods and the industrial instancing. Section 3.3 presents the results of the industrial implementation. Section 3.4 concludes the manuscript and discusses possible future developments.

3.1.1 Industrial Relevance

CAD three-dimensional (3D) Models are nowadays ubiquitous in many engineering contexts: in the automotive industry, for instance, more than 30.000 different parts are needed for complete vehicle, and most of them have a 3D CAD representation. These CAD models are created in different software packages (such as CATIA, SolidEdge, etc.) and by many companies working together (Tier-1 and Tier-2 system and component providers, Car OEM manufacturers, etc.). These CAD software packages have internal powerful tools to work in design, change, inspection, and assembly tasks, but in collaborative work using CAD models from different CAD systems, a standard 3D CAD Model representation is needed. For this, the STEP (ISO 10303-21 [37]) and the IGES standards [38] are widely used, not only to accomplish the transfer of models between CAD systems, but also to provide a vendor-independent 3D CAD model representation that can be used by any software tool.

In this sense, the ability to inspect the topology and the geometry of a standard 3D CAD representation model (such as STEP) is of high importance. More particularly, feature recognition is a task where this model inspection is relevant for engineers and designers, since they can easily find features of interest that are related with specific tasks: optimization, planning of additional manufacturing processes, detection of design errors, etc. However, the way to specify a feature

recognition strategy is not evident, since it involves not only a geometry or topology intrinsic characteristics, but often also a meaning (a semantic level) [39], which is related to the application need. Several approaches for feature recognition have been proposed in the literature (as discussed in the literature review). Our approach allows the user to define reconfigurable arbitrary confluent tests with topologic and geometric filters, configured in a directed acyclic graph, thus offering the flexibility to define simple sequences or chains, but also more complex logic tests to be performed.

Several problems arise from the export of 3D CAD models to STEP or IGES standards. These problems are not intrinsically related with the ISO STEP [37] specification, but to the implementation of the export functionalities in the most common CAD systems. Most of them are related to the "semantic loss", as originally formalised by Posada [1]. This includes losses of hierarchical structure, parameters, part catalogue information, PDM attachment, relationships, functional operators and naming structure, among others (Figure 3.1).

Other kinds of problems that 3D converted files present in STEP include wrong or inappropriate geometrical or topological descriptions. Some of the most common errors that use to appear in this category are: (i) wrong description of cylindrical or rectangular holes as solid cylinders or solid cuboids, (ii) description of simple geometric primitives in terms of more complex structures: a typical case is the conversion of Cylinders, Cones, Toroid sections, or Planar FACES to non-uniform rational basis spline curves (NURBS), adding unnecessary complexity to the converted model, and (iii) conversion of auxiliary structures used in the CAD system for internal purposes as if they were intrinsic geometric parts of the 3D model (e.g., dimension LINES, axis LINES, etc.).

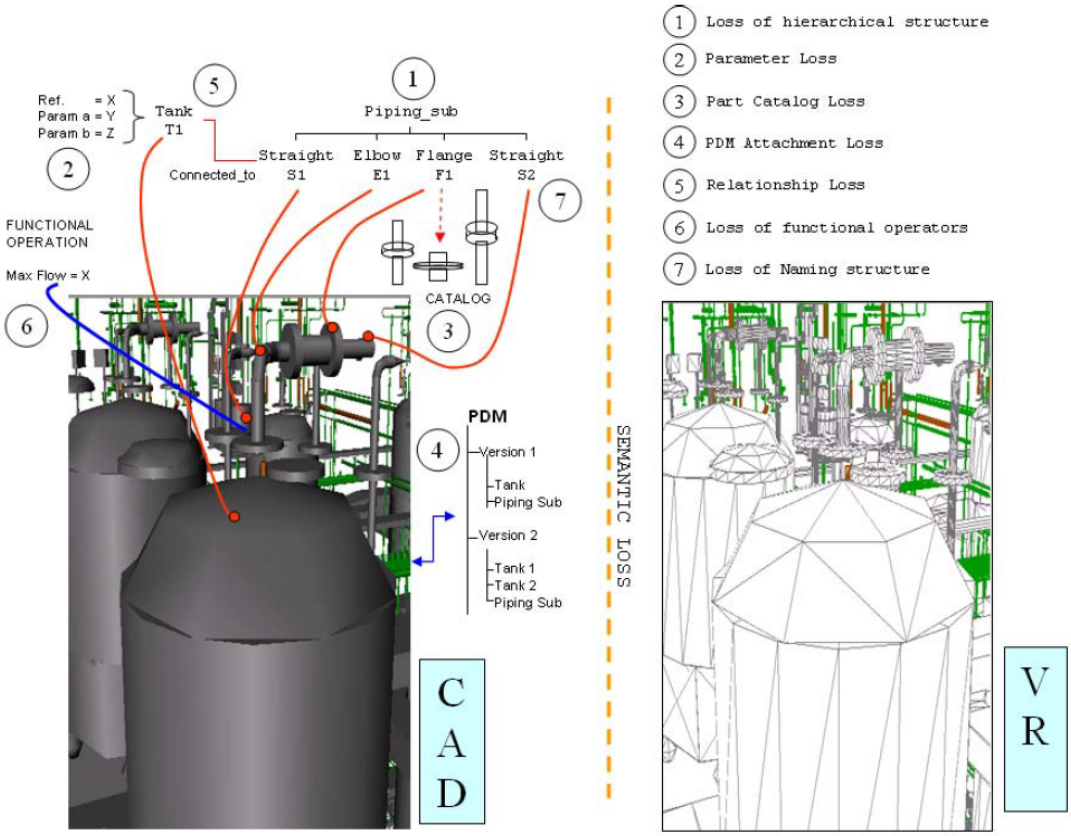

Figure 3.1: Examples of "Semantic loss" of three-dimensional Computer-aided Design (3D CAD) Models conversion to STEP (for various purposes, such as Virtual Reality visualization and interaction with the model). Adapted from [1].

There are real industrial problems that originate in these conversion processes. Our proposed methodology can help the engineer or designer to tackle many of these errors, as it provides a way to specify fast geometric and topological tests that can be interactively specified. To mention a few:

1. Adaptation of 3D CAD complex models for optimal visual inspection and interaction in Virtual Reality (as explained in [40]).
2. Reconstruction of semantic features of converted parts (as in [41]).
3. Geometric simplification of the model.
4. Automatic detection of rounder corners and chamfers.
5. Automatic detection of holes. This is a very relevant and frequent case, used to prepare industrial procedures, such as workpiece painting, part drilling, robotic manipulation, structural optimization, etc.

Following an early approach similar to our method, Posada et al. [1,39] showed how the problems (i), (ii), and (iii) could be solved in the context of the problems (1), (2) and (3) above, specifically in the case of large 3D CAD models of chemical plants and automotive factories (example in Figure 3.2), using the STEP ISO 10303-21 standard to recover structure and meaning of the models.

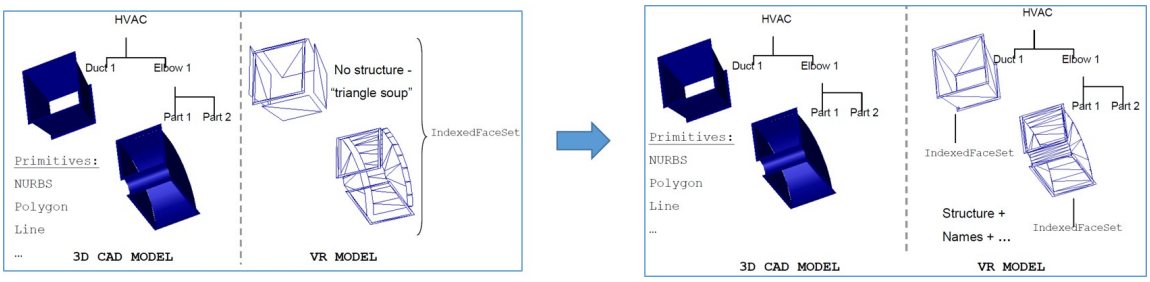

Figure 3.2: Example of recovering structure and meaning of 3D CAD model while using feature recognition and the STEP standard in the early approach of Posada et al. [1].

Our approach is more systematic in the interactive formalisation of the graph structure for the geometric pruning and it is more comprehensive in terms of the geometric filter algorithms and the support of topologic primitives.

Industrial Case

In the industrial case presented in this article, we show in detail how the problem of automatic detection of holes can be tackled with our new approach (problem 5. above). The industrial problem described is the following: a specialized engineering company handles thousands of 3D CAD models of sheet metal parts (Figure 3.3) for automotive and aeronautic industries. One important operation that they perform on the models is the painting planning strategy for each part, and this requires the automatic location of holes in the CAD model as a critical step. They have many providers that use different CAD systems, and they work on the common basis of the 3D CAD models exported as STEP models.

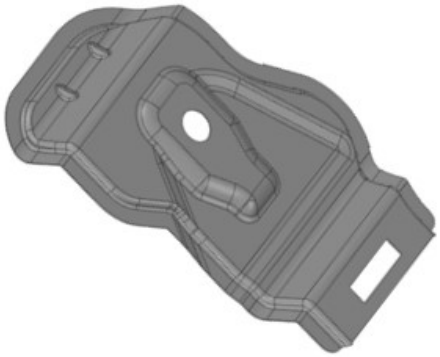

Figure 3.3: Example of sheet metal parts used in the industrial case.

However, the reality is that many of those exported models have insufficient specification of the holes (as explained above), so the STEP model inspection has to perform a combined geometry and topology test to correctly identify the holes. For instance, a common semantic loss that appears in these models is that hole geometries and topologies are incorrectly described in the STEP file. The use of our interactive method allows for a straightforward solution the problem, since our feature recognition system was well suited for this task. It allows to perform the required test as a feature recognition task that not only identify correctly holes in well-exported models, but also overcomes potential problems in the description of some exported models. A software system implementing the presented methodology was successfully deployed at the company engineering department. We will now present our method, and show its implementation and validation results.

3.1.2 Literature Review

Syntactic Pattern approaches for Feature Recognition (FR) [42–44] use a description language based on semantic (manufacturing) primitives to express the workpiece and then compare the syntax of the primitive expression against a grammar that defines a particular feature. These approaches cover a small domain of features (2D prismatic, rotational, turning, and revolution).

Logic Rule FR [45–47] use a rule set that defines a particular feature, using a FACE as seed. The rules specify the number and type of bounding FACEs. These methods are more robust than Syntactic Pattern FR. However, they (a) present ambiguities in the feature definition, and (b) have a reduced domain (only prismatic solids).

Graph-based FR [48–51] creates an Attribute Adjacency Graph (AAG) which contains the topology connectivity of FACEs in a given Solid Boundary Representation (B-Rep) and matches subgraphs of the AAG to a database of diverse (feature) patterns. The shortcomings of graph-based FR are: (a) the extensive pre-processing to build the graphs representation of the workpiece and of each feature primitive, and (b) missing parts in the graph to be matched, caused by nested or inter-acting features. Positive outlooks for these methods are the new graph algorithms that apply AI (such as Hybrid Graph-Rule FR), which address interacting or nested features.

Feature Vector FR [52] extends the simple graph-based approach by applying a new EDGE

classification scheme, allowing for the treatment of curved FACEs. The approach is based on a unique method to represent any given feature, called feature vector, which can be generated directly from the B-Rep modeller. The use of feature vectors in the recognition process allows for polynomial time performance for any Attribute Adjacency Graph (AAG).

Volume Decomposition FR [53,54] determines a polyhedral convex hull circumscribed around the workpiece and define the boolean differences between the convex hull and the workpiece as an alternant union or subtraction of volumes. Volume Decomposition FR is a heuristic method. Thus, there is no guarantee of the feature being correctly expressed by the volume decomposition. It is (as all FR algorithms) computationally expensive.

An **Access Direction** FR [55] is based on the directions from which access to the feature is possible. This particular work is implemented on STEP-based platform, thus rendering independence from proprietary formats. This approach is limited to features machinable in 3-axis centres.

Declarative Feature Language FR [36, 56] defines the CAD features using a declarative language based on base entities (FACEs, EDGEs, etc...) and relations among them. Afterwards, the feature definition is translated into a database query for the CAD modeler database. A naive translation from the declarative language to the database query results in an unfeasible time complexity for any realistic number of entities, therefore, database optimization techniques are applied to reduce the time complexity of the method [36]. The main advantage of this approach lies in the superior performance with respect to other approaches when treating complex geometries and large data sets. The main disadvantage is that it relies heavily on the correctness of the CAD modeler database; therefore, incapable to treat semantic loss problems.

Another STEP-based approach is presented in [57], which describes FR with non planar surfaces (cylinder, cone, sphere, torus, B-spline, swepts). This approach is similar to Volume Decomposition in that it identifies volumes to be removed in order to manufacture the feature. The FACE and EDGE-based topological and geometrical information is collected in a first pass. In the second pass, the non-planar FACE- based featured are extracted. A drawback of this approach is that it relies on a EDGE-based search, expensive with complex curved surfaces.

Reconfigurable FR [58] obeys to the fact that a feature is an inherently subjective denomination, which may correspond to different topological/geometrical B-Rep neighborhoods, according to the field and application of the workpiece. This work presents a feature declaration language and underlying geometric reasoning server, which allow a more efficient FR, at the price of each user re-configuring his/her FR declaration and underlying filters.

3.1.3 Conclusions of Literature Review

Generally, previous approaches to the Feature Recognition problem present three major shortcomings: (i) a reduced domain of application, mostly restricted to boolean combinations of prismatic shapes or turning parts; (ii) reliance on FACE or EDGE search and classification, therefore excluding other useful geometric information; and, (iii) inability to treat the semantic loss problem in STEP-based methods. The interested reader may refer to the survey in Ref. [59], to complement our review.

In response to some of the existing shortcomings in FR, here we present the design and implementation of an interactive re-configurable graph search method for FR. Our approach prunes the B-Rep search space with user-prescribed geometric tests. An early reduced version of this work is presented in the short paper [2]. Therefore this manuscript is an extension of [2] with considerable additional contributions. The present manuscript contains the following elements, absent in [2]:

(i) analysis of the industrial relevance of the approach, (ii) complexity analysis of the algorithm, (iii) details about the implementation and the Graphic User Interface for interactive Feature Recognition, (iv) search graph construction strategies, (v) additional curvature-based geometric filters, and (vi) industrial instancing with more examples. In the current manuscript, we fully discuss the construction methodology for the search graph structure and introduce the curvature-oriented geometric filters that allow for curved-geometry identification. In [2], we discussed the method's performance with respect to the number of nodes in the search graph. In the current manuscript, we extend such discussion to include a complexity analysis of our method. Our approach admits topologies of the types 0 (VERTEX), 1 (EDGE or LOOP), and 2 (FACE or SHELL). It is implemented on STEP [37] B-Rep standard, which facilitates its migration to other modelers.

3.2 Materials and Methods

Our implementation includes a *Parsing stage* and a *Domain Depuration stage*, as follows (Figure 3.4).

Parsing stage. This stage parses two inputs: (a) an user-defined unstructured search graph, and (b) part STEP file containing geometry and topology information of the workpiece. Process (a) is written in C++ and translates into a graph structure of geometrical tests which includes the target topologies. The test enforcement order is implicit in the pruning graph structure. In the parsing stage, each pruning node is equipped with geometry or topology boolean test functions. At the domain depuration stage, the relevant test is triggered and a boolean FALSE would result in the elimination of the tested topologies from the search space. In this manner, the FR parsing stage produces the pruning test graph, with its nodes loaded with the geometry test functions and pruning actions, Process (b) part STEP file parsing is achieved by using Open Cascade [RC12] platform. The Open Cascade Processor populates a Boundary Representation (B-Rep) database by parsing the workpiece STEP file, thus producing the initial search domain Ω_0.

Domain Depuration stage. This stage executes upon the B-Rep Ω_0 domain the boolean tests implicit in the pruning graph, progressively reducing the domain. Following the graph structure of the pruning process, the output of a pruning node is the input of the following one. The geometrical/topological condition of the current iteration is applied to all target topologies of the current search domain and those topologies who fail the test are purged from the search domain, hence reducing its size in after enforcing each node conditions. Once all conditions in the sequence are enforced, the resulting search domain corresponds to the topologies that constitute the desired features.

3.2.1 Search Graphs

A domain pruning graph is a directed acyclic graph (DAG). Although in many cases this pruning graph is a simple sequence (i.e., a chain), it must be realized that more involved domain reductions require general DAGs. Each node in such graphs contains the specification of the topologies to be tested and the nature of the test. The DAG for search domain pruning is general enough to allow diverse boolean test sequences. However, as said before, in the majority of cases the manufacturing engineer or technician specifies a chain sequence (e.g., Figure 3.5).

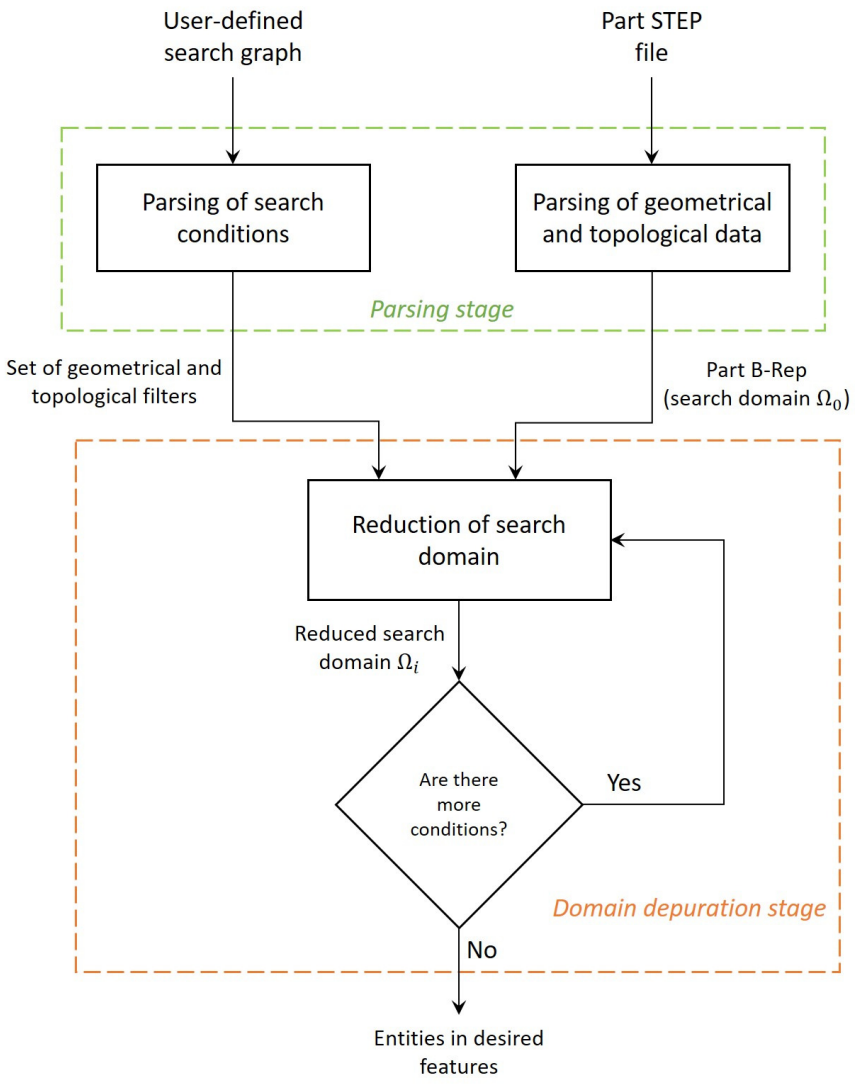

Figure 3.4: Original flowchart of recognition process (adapted from [2]).

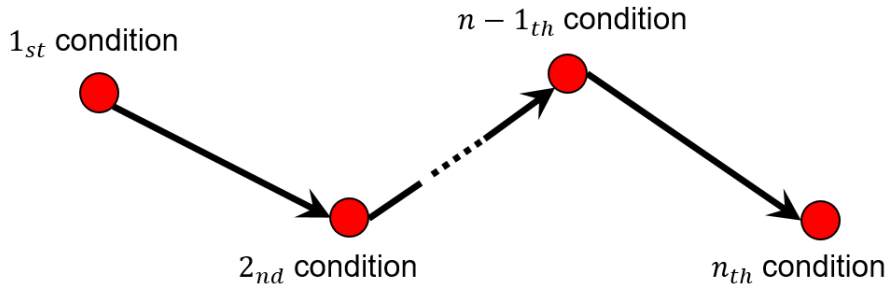

Figure 3.5: General scheme of the proposed search graph.

In a Domain Pruning Graph, nodes can be classified into three types: (1) Topologies, (2) Geometry Tests, and (3) Topology Tests. (1) Topologies are the 0-, 1-, and 2-manifold sets SHELL, FACE, LOOPE, EDGE, VERTEX, represented by Programming Objects or classes. (2) Geometry Tests are the boolean queries responded by querying the underlying Geometries of the Topologies (Parametric Surfaces and Curves, and Points). (3) Topology Tests are also boolean queries, stated on one or more Topologies, which are not solved by geometric arguments. An approximate grammar for a Pruning Graph is:

$$
\begin{aligned}
&\langle pruning\_graph\rangle \longrightarrow \langle serial\_test\rangle\ AND\ \langle pruning\_graph\rangle\\
&\langle pruning\_graph\rangle \longrightarrow \langle serial\_test\rangle\\
&\langle serial\_test\rangle \longrightarrow \langle atomic\_test\rangle\ OR\ \langle serial\_test\rangle\\
&\langle serial\_test\rangle \longrightarrow \langle atomic\_test\rangle\\
&\langle atomic\_test\rangle \longrightarrow \langle topology\_test\rangle \mid \langle geometry\_test\rangle\\
&\langle topology\_test\rangle \longrightarrow \langle topology\rangle\langle topo\_relation\rangle\langle topology\rangle\\
&\langle topology\rangle \longrightarrow SHELL \mid FACE \mid LOOP \mid EDGE \mid VERTEX\\
&\langle topo\_relation\rangle \longrightarrow CONTAINED \mid CONTAINS \mid IS\_ADJACENT\\
&\langle geometry\_test\rangle \longrightarrow \langle topology\rangle\langle geometry\_property\rangle\\
&\langle geometry\_test\rangle \longrightarrow \langle topology\rangle\langle geometry\_property\rangle\langle topology\rangle\\
&\langle geometry\_test\rangle \longrightarrow \langle topology\rangle\langle geometry\_property\rangle\langle value\rangle\\
&\langle geometry\_property\rangle \longrightarrow CYLINDRICAL \mid CIRCULAR \mid PARALLEL\\
&\qquad\qquad\qquad\qquad\qquad\qquad PLANAR \mid DEAD\_END\\
&\langle value\rangle \longrightarrow \langle real\_number\rangle
\end{aligned}
$$

It must be stated that, in our implementation, this grammar is implemented by driving the user actions through the Graphic User interface and not by parsing a description file (although it would be also possible).

Figure 3.6 presents examples of pruning graphs built while using the grammar mentioned above. Notice that the effectiveness in reducing the search space directly depends on the precision and consistency of the pruning graph. An inconsistent graph would end in a null solution space, independent from what Ω_0 is. A too lax pruning graph would allow for a large search space, thus failing to execute FR.

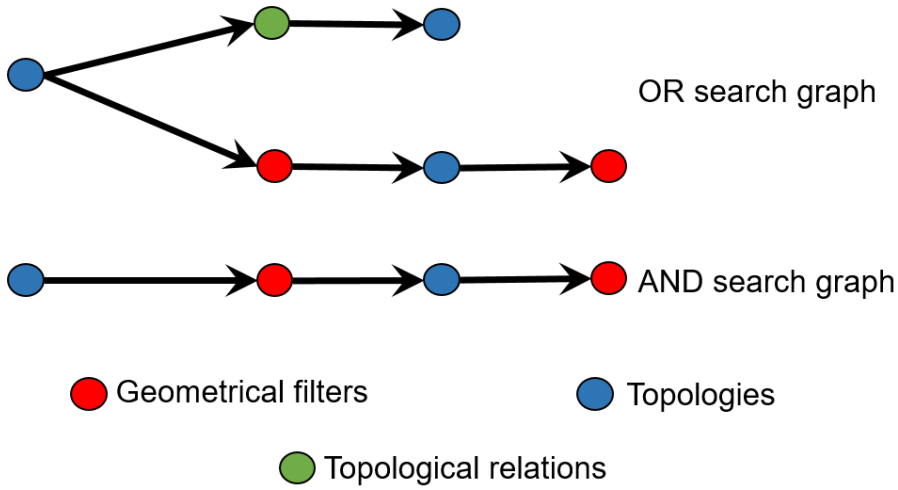

Figure 3.6: Examples of search graph building.

3.2.2 Topology-Geometry Data Structure

A geometry-topology data structure is needed to efficiently store and manage all geometric and topological information of the solid workpiece in order to explore and reduce the search domain. The data structure implemented is based on the *OpenCascade* [60, 61] platform and it resembles a B-Rep data structure. Figure 3.7 shows the implemented data structure.

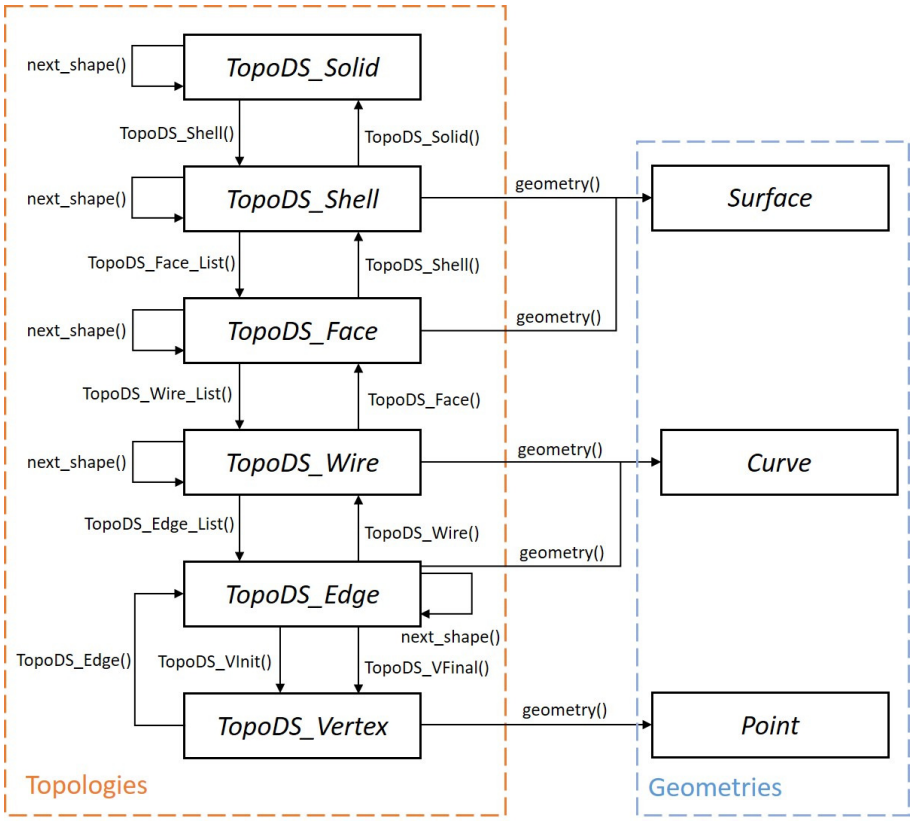

Figure 3.7: Original geometry-topology data structure, using OpenCascade™ data names (which differ but are mathematically equivalent to ACIS™ terms)-see Ref. [2] from same authors.

The hierarchical organization of the data structure allows for exploration of the topology-space of the workpiece and access to the geometrical properties of any topology. As usual, Topology connectivity relations among entities, while Geometry refers to positions, sizes, and underlying shapes. Geometric filters are applied on geometrical entities, not directly on topologies. Therefore, access to the geometric entities underlying the topologies is required to apply the geometric filters. All geometry and topology classes are derived from the base *TopoDS* class in the *OpenCascade*™ library.

3.2.3 Topological Relations

Topological Tests assess whether the given topologies comply with the inquired role (CONTAINED, CONTAINS, IS_ADJACENT). These interrogations are answered using the structure implicit in the B-Rep data structure (Figure 3.7), instanced in the particular workpiece at hand. Figure 3.8 shows examples of the implemented topological tests.

Figure 3.8a shows the adjacency relation, which determines whether two FACEs are adjacent to each other (i.e., their border LOOPs share an EDGE). Figure 3.8b shows the containment relation,

which determines whether an EDGE is contained in any of the border LOOPs of the given FACE. This test is also applied to LOOPs containing an EDGE. The use of topological relations in the search graph allow for greater flexibility in the FR process taking advantage of the hierarchical organization of topologies and their relations to one another.

3.2.4 Geometrical Filters

Geometrical Filters assess whether or not a subset of the B-Rep satisfies a given geometric condition. Failure to pass the filter eliminates such a B-Rep subset from the search space, therefore, reducing the search space for the next filters. New geometrical tests specially suited to treat curved geometries underlying 2- and 1-topologies are required to identify features containing curved geometries. Examples follow.

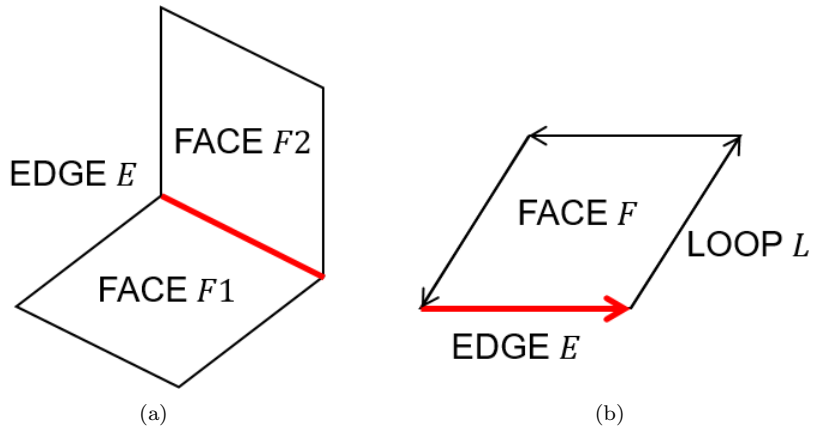

Figure 3.8: Examples of Topological Tests. (**a**) FACEs $F1$ and $F2$ are adjacent (through EDGE E), (**b**) FACE F contains EDGE E.

Cylindrical FACE Test

The goal of this test is to determine whether a FACE topology is carried by a cylinder geometry (within user-specified error margins). Ruiz et al. proposed the method in use [62], and it goes as follows (Fig. 3.9):

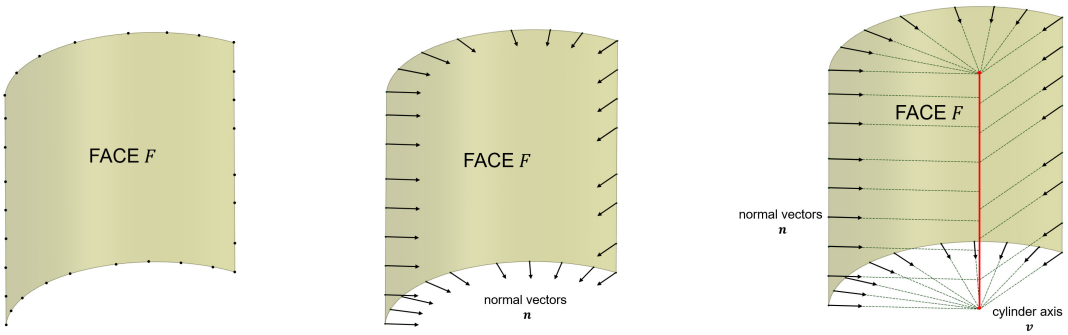

(a) (b) (c)

Figure 3.9: Cylindrical FACE geometrical filter. (**a**) Initial surface underlying FACE F, (**b**) Normal vectors $\vec{n}$ on surface, and (**c**) Cylinder's axis $\vec{v}$ estimation.

Denote $\vec{P}$ as the set of Points in the underlying surface of a FACE topology:

1. For each point $p \in \vec{P}$, calculate the normal vector $\vec{n_p}$ of a plane tangent to the surface in p.
2. By crossing each other two line segments defined by a point and its associated normal vector, a set of points $\vec{C_p} = \{q_1, q_2, q_3, ...\}$ near the cylinder's axis $\vec{v}$ is obtained. Notice that, even when two line segments do not intersect, a crossing point can still be obtained as the midpoint of the line segment corresponding to the shortest distance between the two initial line segments.
3. The technique of Principal Component Analysis (PCA) is used to obtain an approximation of the cylinder's axis $\vec{v}$ and its pivot point v_p from set $\vec{C_p}$.
4. For each point $p \in \vec{P}$, the distance to the cylinder's axis $\vec{v}$ is calculated. The surface resembles a cylinder if all calculated distances are similar within a specified tolerance range.

Circular EDGE Test

Using a similar strategy, the goal of this test is to determine whether an EDGE topology is carried by a circle geometry (within user-specified error margins). The method in use is a modification of the method that was proposed by Ruiz et al. [62]:

Denote $\vec{P}$ as the set of Points in the underlying curve of an EDGE topology:

1. For each point $p \in \vec{P}$ calculate the normal vector $\vec{n_p}$ of a plane tangent to the curve in p.
2. By crossing each other two line segments defined by a point and its associated normal vector, a set of points $\vec{C_p} = \{q_1, q_2, q_3, ...\}$ near the circle's origin O is obtained. In this case, any two line segments will always intersect, since they are coplanar.
3. The circle's origin O is defined as the point which coordinate values are the average values of the coordinates of points in set $\vec{C_p}$.
4. For each point $p \in \vec{P}$, the distance to the circle's origin O is calculated. The curve resembles a circle if all the calculated distances are similar within a specified tolerance range.

Another set of implemented geometrical filters is based on the surface curvature supporting the FACE topology (Fig. 3.10). For every point of the surface is possible to compute the principal curvatures values κ_{max}, κ_{min} and directions $\vec{u_{max}}$, $\vec{u_{min}}$, which are descriptors of how much and in which directions the surface bends in a specific location [63]. Different conditions on those geometric entities can be tested to identify the underlying nature of the surface [64]. Additionally, in the spherical and cylindrical surface tests, it is possible to define an optional constraint on the value of the curvature radius. All of the following tests are implemented in the *Geomlib SDK* [65] and they are based on the *OpenCascade* library.

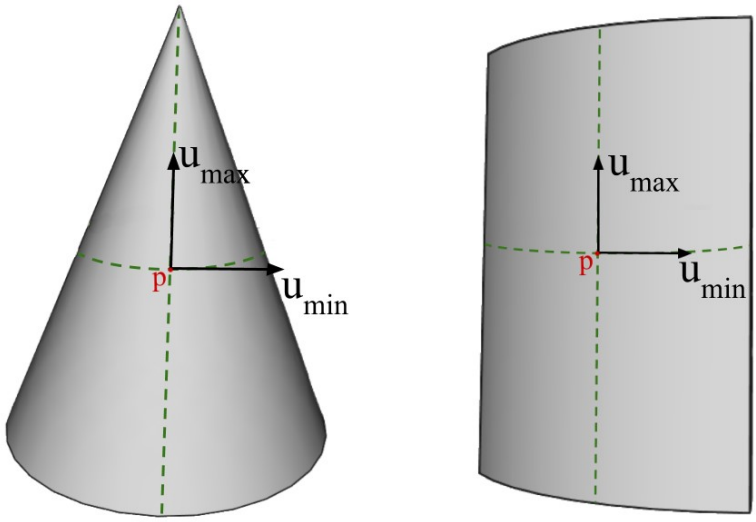

Figure 3.10: Example of maximum and minimum curvature directions in a generic point $\boldsymbol{p}$. The curvatures $\vec{u}_{min}$ and $\vec{u}_{max}$ are perpendicular, while their values are $k_{min} = 0$ and $k_{max} = const$ in both cases.

Planar FACE Curvature Test

The goal of this test is to determine whether the FACE topology is carried by a planar geometry. For every point of a plane, the two principal curvature values are equal to zero and the normal vector is constant in direction and orientation. Denote $\vec{P}$ as the set of points obtained by sampling the surface continuous parametric uv space with $u_{samples}$ and $v_{samples}$ number of samples in the two dimensions.

1. For each point $p \in \vec{P}$, calculate the normal vector $\vec{n_p}$ of a plane tangent to the curve in p.
2. For each point $p \in \vec{P}$ calculate the principal curvature values κ_{p_min} and κ_{p_max}.
3. The underlying geometry is planar if $\vec{n_p} = const$, $\kappa_{p\_min} = 0$ and $\kappa_{p\_max} = 0$ for every $p \in \vec{P}$ within a specified tolerance range.

Spherical FACE Curvature Test

The goal of this test is to determine whether the FACE topology is carried by a spherical geometry. For a sphere the two principal curvature values are equal and constant and not zero throughout all the surface. Denote $\vec{P}$ as the set of points obtained by sampling the surface continuous parametric uv space with $u_{samples}$ and $v_{samples}$ number of samples in the two dimensions.

1. For each point $p \in \vec{P}$, calculate the principal curvature values κ_{p_min} and κ_{p_max}.
2. The underlying geometry is spherical if $\kappa_{p\_max} = \kappa_{p\_min} = const$, $\kappa_{p\_min} \neq 0$ and $\kappa_{p\_max} \neq 0$ for every $p \in \vec{P}$ within a specified tolerance range.
3. Optionally compute the radius of curvature $R_p = \frac{1}{\kappa_{p\_max}}$ and control that is equal to a specified value within a tolerance range

Cylindrical FACE Curvature Test

The goal of this test is to determine if the FACE topology is carried by a cylindrical geometry. Differently from the previous tests, in this one, we also take into consideration the direction of the principal curvatures. As a matter of fact, for every point of a cylinder, the minimum curvature direction is constant and its corresponding value is zero, while the maximum curvature is constant and different from zero. An additional condition on the curvature radius is imposed to distinguish the geometry from a cone or a free-form surface. Denote $\vec{P}$ as the set of points obtained by sampling the surface continuous parametric uv space with $u_{samples}$ and $v_{samples}$ number of samples in the two dimensions.

1. For each point $p \in \vec{P}$ calculate the principal curvature values κ_{p_min}, κ_{p_max} and directions $u_{\vec{p\_min}}$, $u_{\vec{p\_max}}$.
2. Test for all of the points that the minimal curvature direction $u_{\vec{p\_min}}$ is constant, its corresponding value κ_{p_min} is zero and the maximum curvature value κ_{p_max} is constant and different that zero within a specified tolerance range.
3. For each point $p \in \vec{P}$, compute the radius of curvature $R_p = \frac{1}{\kappa_{p\_max}}$.
4. Test that the radius is constant throughout all the surface $R_p = const$ within a specified tolerance range.
5. Optionally control that the radius of curvature R_p is equal to a specified value within a tolerance range.

Conical FACE Curvature Test

The goal of this test is to determine whether the FACE topology is carried by a conical geometry. The procedure is similar to the previous one but with no curvature radius test and an additional fitting stage. Denote $\vec{P}$ as the set of points obtained by sampling the surface continuous parametric uv space with $u_{samples}$ and $v_{samples}$ number of samples in the two dimensions. Additionally, define a smaller set of points $\vec{P_{sub}} \in \vec{P}$ obtained with an evenly spaced sub-sampling of $\vec{P}$. It is important that this set is small in order to ensure that the execution time remains small.

1. For each point $p \in \vec{P}$ calculate the principal curvature values κ_{p_min}, κ_{p_max} and directions $u_{\vec{p\_min}}$, $u_{\vec{p\_max}}$.
2. Test for all the points that the minimal curvature direction $u_{\vec{p\_min}}$ is constant, its corresponding value κ_{p_min} is zero and the maximum curvature value κ_{p_max} is constant and different that zero within a specified tolerance range.
3. For each point $p \in \vec{P}$ compute the radius of curvature $R_p = \frac{1}{\kappa_{p\_max}}$ and test that its value is not constant within a specified tolerance range.
4. Use the RANSAC algorithm [66] to fit a cone to $\vec{P_{sub}}$. If the algorithm succeeds the FACE supports a conical geometry.

3.2.5 Complexity and Performance

The overall performance of the presented methodology is mainly influenced by two aspects: (i) the number of entities in the model and (ii) the number of nodes in the search graph and the performance of the filter itself. Regarding the number of entities, a larger model will negatively impact the performance of the algorithm, since the initial search domain is larger and requires more evaluations of the geometric filter in each step of the search process. One must understand the trade-off that takes place to assess the performance consequences of introducing new nodes to the search graph: a new filter adds new operations to the execution sequence and at the same time reduces the search domain for the next filter. Thus, if a new filter is inserted in the search graph, in general the subsequent filters will experience a reduction of the number of operations to perform, since the search domain is reduced by the insertion of the new filter. Therefore, adding a new filter might actually improve performance if the number of saved operations is larger than the number of operations added by the insertion of the new filter. The type of filter is also important to assess performance, since not all filters reduce the search domain by the same amount and this depends on the characteristic of initial data and desired feature. Therefore, adding a filter with high reduction somewhere in the search graph will have positive effects on the performance of the algorithm.

The currently accepted theoretical algorithm for the graph isomorphism problem (which is the underlying problem in most of the methods found in literature) has a time complexity of $2^{O\left(\sqrt{n \log n}\right)}$ [67]. More recently, a quasipolynomial time algorithm [68] was announced with a time complexity of $2^{O((\log n)^c)}$ for some fixed $c > 0$.

In order to calculate the time complexity of our algorithm, we assume a survival rate α, which is, after each iteration α percent of entities survive the filter. We denote n as the length of the initial geometry-topology data and M the number of filters in the search graph. We assume the filters to be a constant-time operation, since it is applied to an individual topology and does not depend on the length of the initial data set. Time complexity T of the algorithm is then estimated as:

$$T(n, M) = \alpha^0 n + \alpha^1 n + \alpha^2 n + \alpha^3 n + ... + \alpha^M n \tag{3.1}$$

Subsequently, we can express the time complexity of the algorithm as:

$$T(n, M) = O(Mn \log n) \tag{3.2}$$

In order to compare the computational resources savings of our method with respect to other approaches found in literature, Table 3.1 summarizes the time complexity of different methodologies.

Notice that complexities are expressed for a model of n entities, but the basic operation used to measure complexity in each method may be different; or the method could require additional processes not taken into account in the complexity measurement.

Table 3.1: Time complexity comparison between Feature Recognition (FR) approaches for a model with n entities.

Method	**Claimed Complexity**	**References**	**Comments**
Graph Matching	$O\left(n^k\right)$	[36, 69]	k: number of nodes in feature graph
Feature Vector	$O\left(n^3\right)$	[52]	Requires additional geometric processes that may affect performance
Volume Decomposition	$O\left(n^k\right)$	[69]	k: number of cells generated for each feature
Naive Language	$O\left(n^k\right)$	[70]	k: number of entities in the feature
Optimized Language	$O\left(n\right)$	[36, 56]	Linear Complexity is achieved only for simple features
Our method	$O\left(Mn\log n\right)$	Current Manuscript	M: number of filters in the search graph.

3.2.6 Graphic User Interface

The proposed method has been implemented in an industrial environment while using a Graphic User Interface (GUI) based on icon graphs for the search graph construction with default pre-programmed geometrical filters. The GUI allows for further user customization by allowing the expansion of the geometrical filters library. Figure 3.11 shows the Graphic User Interface developed while using C++ graphic libraries.

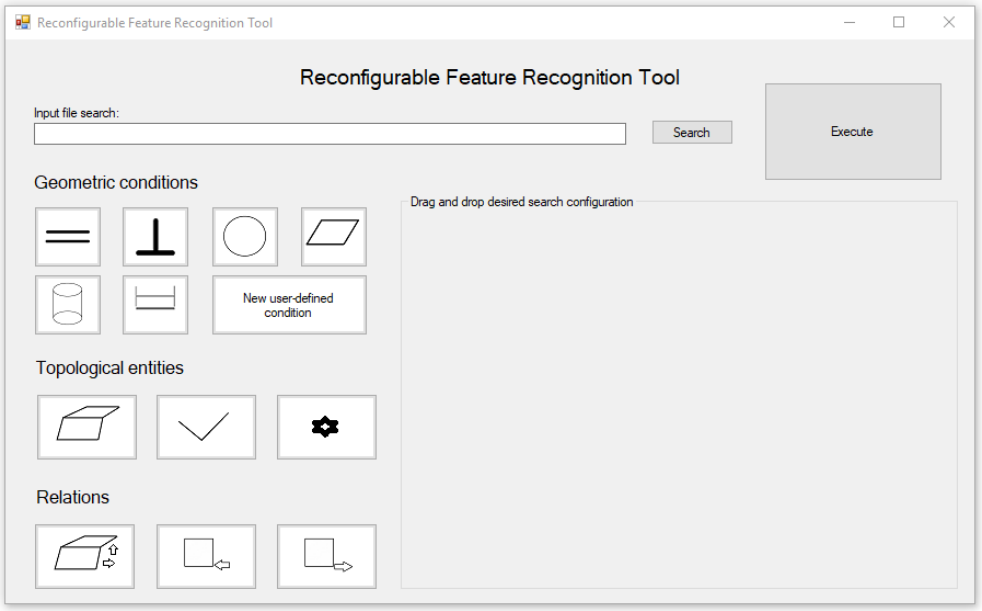

Figure 3.11: Tool's Graphic User Interface.

The GUI consists of two panels: left panel contains the graphic icons for the topologies, geometric filters, and topological relations currently implemented, the right panel is an interactive environment where the user can drag and drop the desired icons to build a search graph following the previously presented rules. The Graphic User Interface (GUI) includes, as usual, the functionality to import a neutral format part file (STEP [37]). At the present time, our application does not import IGES [38] format.

Figure 3.12 shows the topologies, topological relations, and geometrical tests currently implemented in the industrial instancing. This library can be further expanded by the user using DLLs to link personalized geometrical filters or topological relations.

Figure 3.13 shows an example of a search graph built using the graphical tool. The GUI does not actively enforce the search graph construction rules, therefore, check of search graph structure validity is left to the user. Figures 3.14–3.17 show the output of the Graphical User Interface after running the feature identification process.

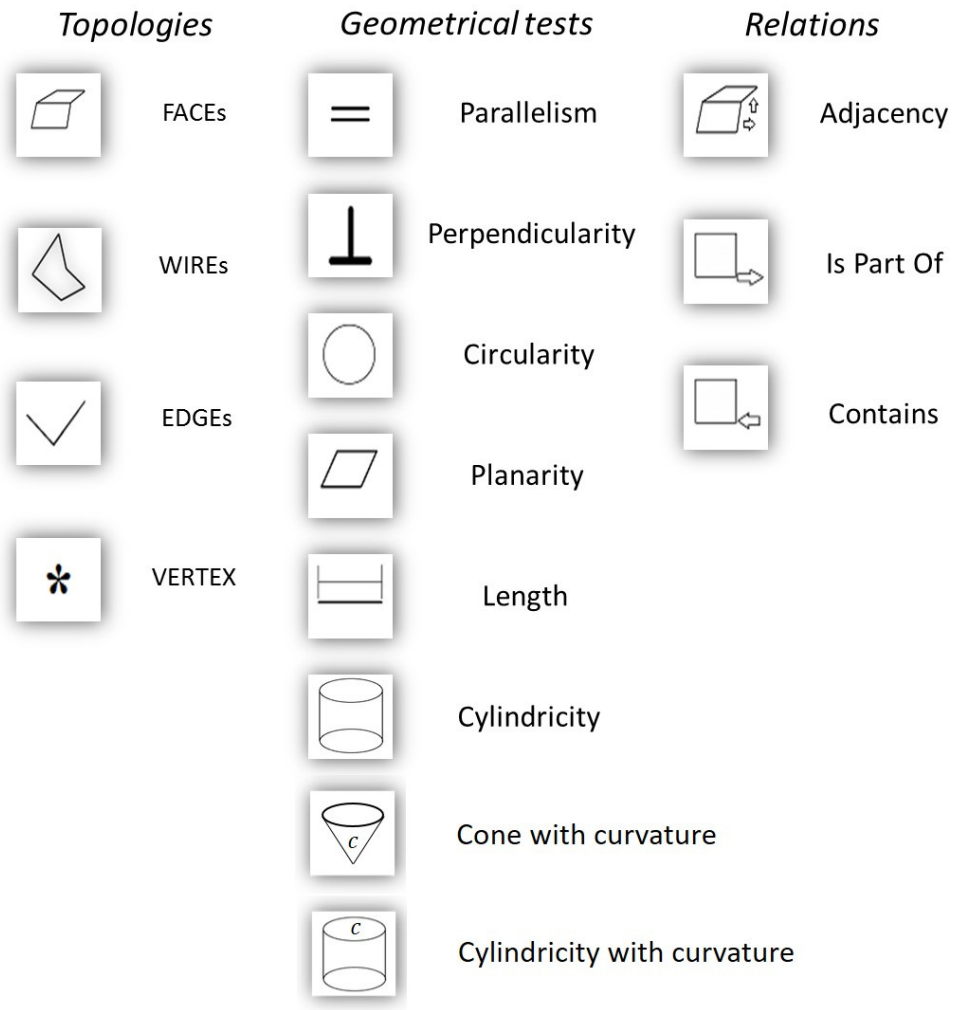

Figure 3.12: Topologies, topological relations and geometrical tests implemented.

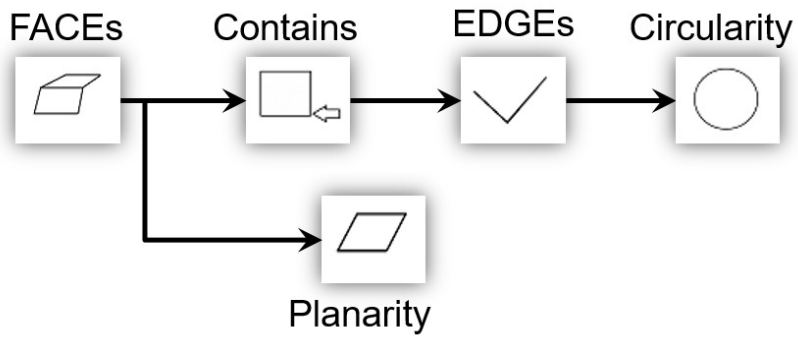

Figure 3.13: Example of search graph as built in the Graphic User Interface.

3.3 Results

To test our interactive FR method, we present four application examples in different workpieces, as shown in Figures 3.14–3.17. In the first two examples, the goal is to identify circular hole features on metal sheet workpieces given that the thickness of the sheet is known. In the third example, the goal is to identify square hole features on a metal sheet workpiece, also with the thickness of the sheet as known data. In the last use case the goal is to identify the chamfer surface of a car disc brake holes, i.e., the conical surface situated on top of the hole cylinders. In the presented examples, we choose a search graph strategy that includes a known dimension (thickness in this case) because it suits our available data, other search graph strategies could be used to execute the FR process for the same feature. Initial search space is denoted as Ω_0 in all cases.

The reduced domain Ω_1, as shown in Figures 3.14a and 3.15a, is the result of pruning the correspondent initial search space Ω_0 with the geometric filter configuration in search graph G_1, as shown in Figure 3.14d (for both data sets). The search graph G_1 applies the CYLINDRICITY condition to all FACEs in the domain Ω_0. Therefore, the reduced domain Ω_1 should only contain cylindrical FACEs, as shown in Figures 3.14a and 3.15a.

The search graph G_2 (Figure 3.14d) is an extension of graph G_1; therefore, further pruning domain Ω_1 by applying extra geometric filters according to the configuration of graph G_2. Graph G_2 preserves from domain Ω_1 all FACEs that are related to an EDGE with a length value specified by the user; in this case, the specified length value is the sheet's thickness t. Resulting reduced domain Ω_2, only contains cylindrical FACEs related to an EDGE of length t, as shown in Figures 3.14b and 3.15b.

The domain Ω_2 contains the desired hole features and other undesired FACEs, therefore, an additional condition is necessary to prune undesired FACEs from domain Ω_2. Search graph G_3 (Figure 3.14d) is an extension of search graph G_2 and further prunes domain $\Omega_2$by only preserving FACEs that are adjacent (share and EDGE with) to a cylindrical FACE in Ω_1. Hence, applying the conditions that result from graph G_3 to the domain Ω_2, results in a reduced domain Ω_3 (Figures 3.14c and 3.15c) only containing FACEs of hole features, ending the process with the desired FACEs. Notice that the further pruning applied by graph G_3, successfully removes the undesired FACEs because of the configuration of these particular hole features. In this cases, hole features are composed of two opposed cylindrical faces (as shown in Figures 3.14c and 3.15c), but is not a general rule for

hole features in all cases.

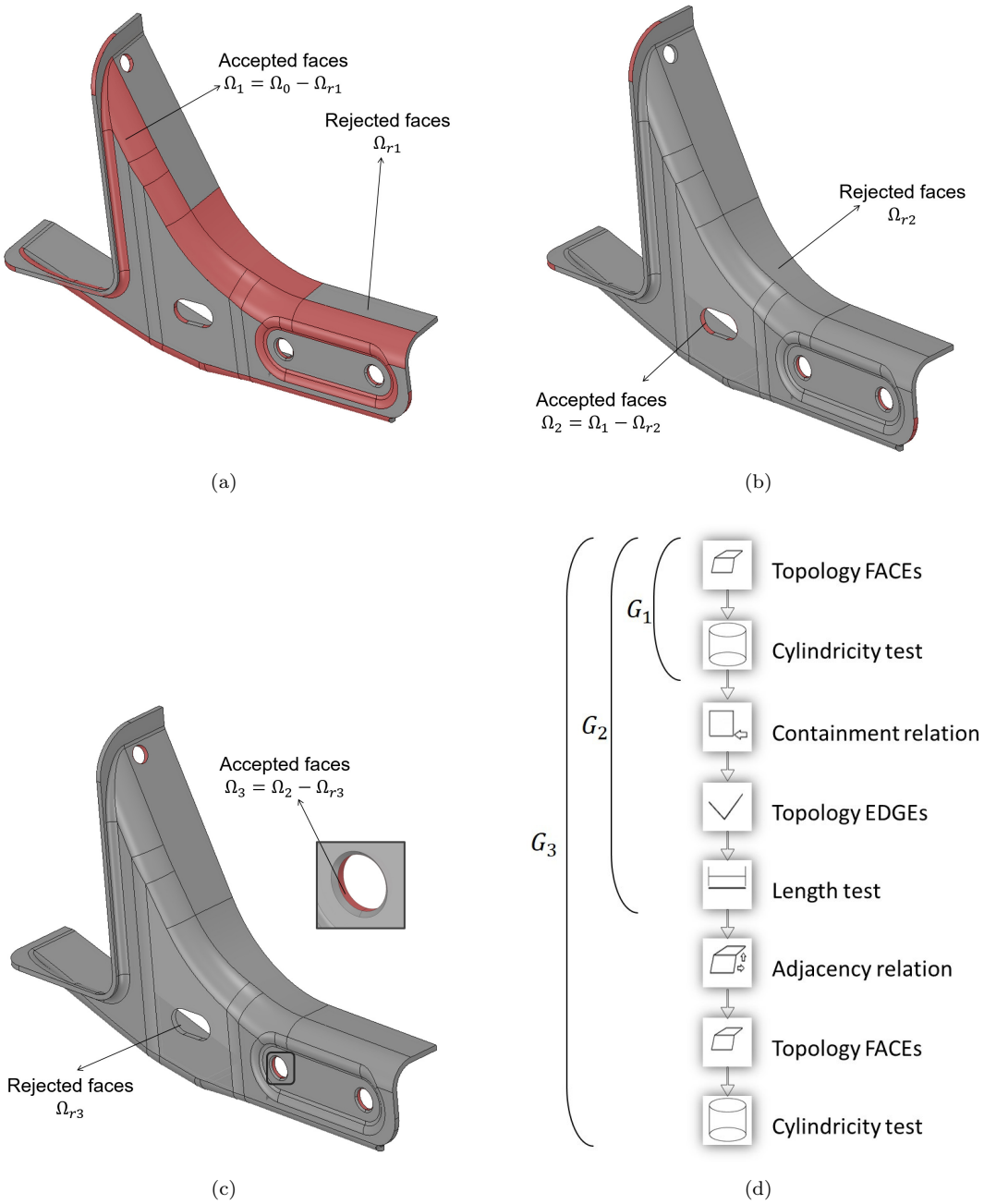

Figure 3.14: Results of Example 1: recognition of hole feature in data set 1 (see Ref. [2] from same authors). (**a**) Reduced domain $\Omega_1 \subset \Omega_0$, (**b**) Reduced domain $\Omega_2 \subset \Omega_1$, (**c**) Reduced domain $\Omega_3 \subset \Omega_2$, and (**d**) Search graphs G_1, G_2 and G_3.

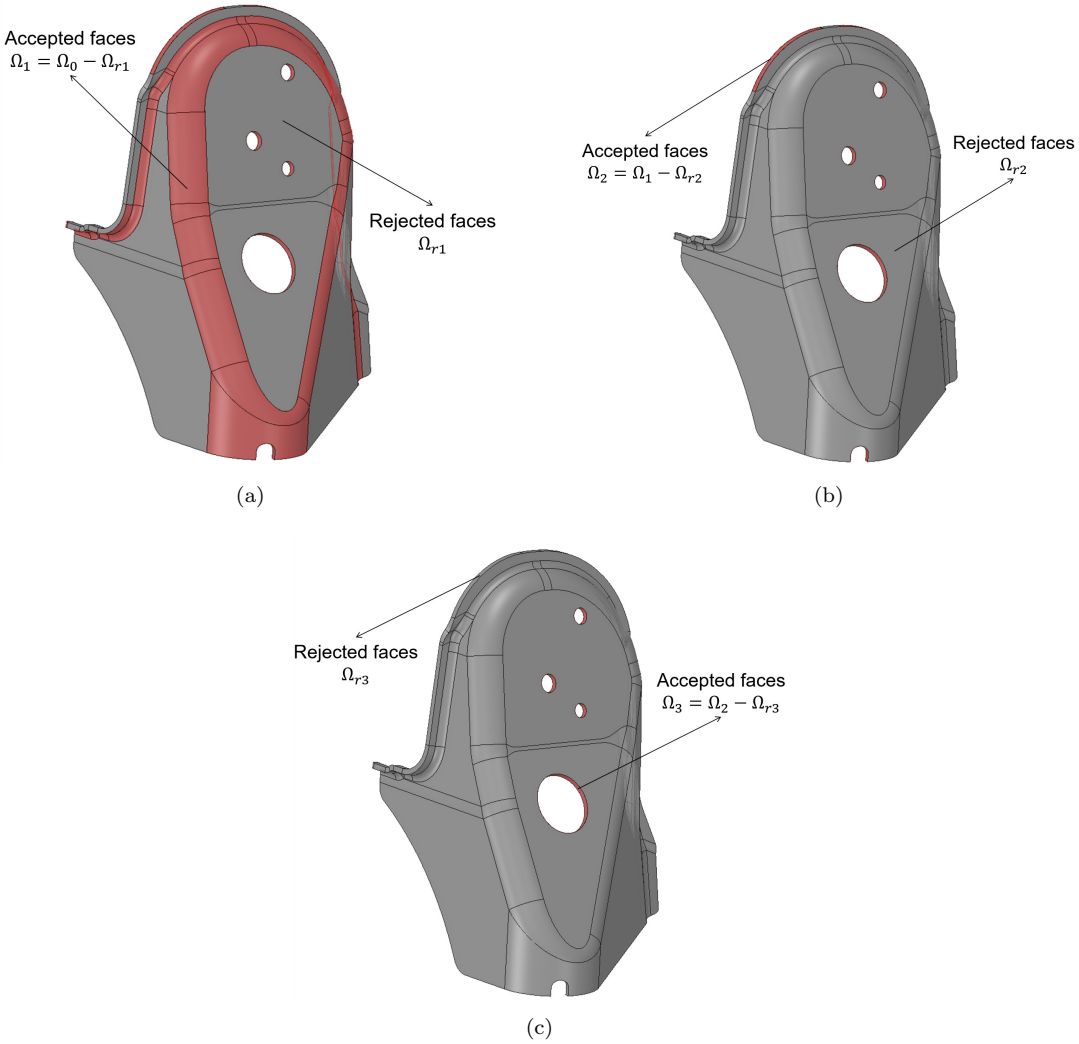

Figure 3.15: Results of Example 2: recognition of hole feature in data set 2. (**a**) Reduced domain $\Omega_1 \subset \Omega_0$, (**b**) Reduced domain $\Omega_2 \subset \Omega_1$, and (**c**) Reduced domain $\Omega_3 \subset \Omega_2$.

In a similar fashion, we present the result of square hole recognition in a sheet metal part in Figure 3.16. Figure 3.16a shows the initial data set Ω_0 and we follow the same search graph strategy from FR in Examples 1 and 2, only changing the CYLINDRICAL geometric filter for the PLANAR geometric filter. Figure 3.16d shows the domain $\Omega_1 \subset \Omega_0$ consisting of all planar FACEs present in initial domain Ω_0 (FACE planar geometric filter). Figure 3.16c shows the domain $\Omega_2 \subset \Omega_1$ consisting of all FACEs part of the square hole feature; domain Ω_2 preserves from domain Ω_1 all FACEs which are related to an EDGE with a length value specified by the user; in this case, the sheet's thickness t. FR for square holes is successfully executed on data set 3.

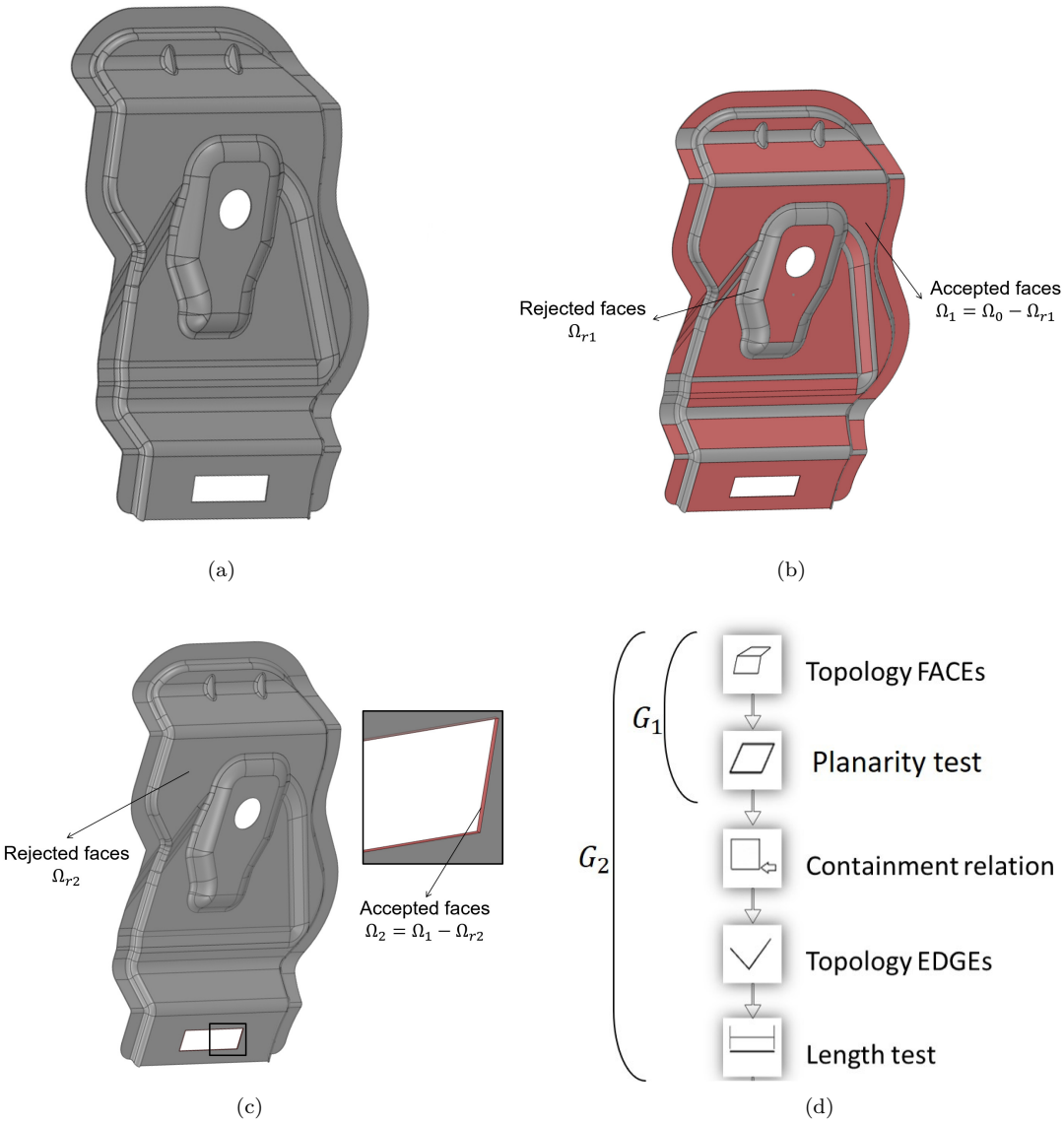

Figure 3.16: Results of Example 3: recognition of square hole feature in data set 3. (**a**) Initial data set Ω_0, (**b**) Reduced domain $\Omega_1 \subset \Omega_0$, (**c**) Reduced domain $\Omega_2 \subset \Omega_1$, and (**d**) Search graphs G_1 and G_2.

Following the same concepts of previous examples, Figure 3.17 shows the process to identify the chamfer surface of all countersunk holes drilled in the object. The model was taken from dataset [71], and is a disc brake of a car. In this case, the search graph is composed of a cone surface test by curvature to isolate all conical FACEs, followed by an adjacency test to all cylindrical FACEs with a known radius, also done with curvature analysis. This reflects the fact that the target surfaces are

always situated on top of the hole cylinders. Figure 3.17a represents the initial data set Ω_0, while, in Figure 3.17b, we have the data domain Ω_1 resulting from a conical surface filter by curvature and the corresponding search graph G_1 (Figure 3.17e). It should be pointed out that not all of the identified FACEs belong to the countersunk holes, for instance the central part of the disc; therefore, more filters are needed. In Figure 3.17c is shown the intermediate result Ω_2 obtained with the cylindricity filter with known radius. Defining the radius value is important to extract only the FACEs belonging to the target holes. In conclusion, the final domain Ω_3 corresponding to the desired result is presented in Figure 3.17d along with the complete search graph G_2 (Figure 3.17e). The target surfaces are extracted from the Ω_1 domain by using the adjacency topological relation with Ω_2.

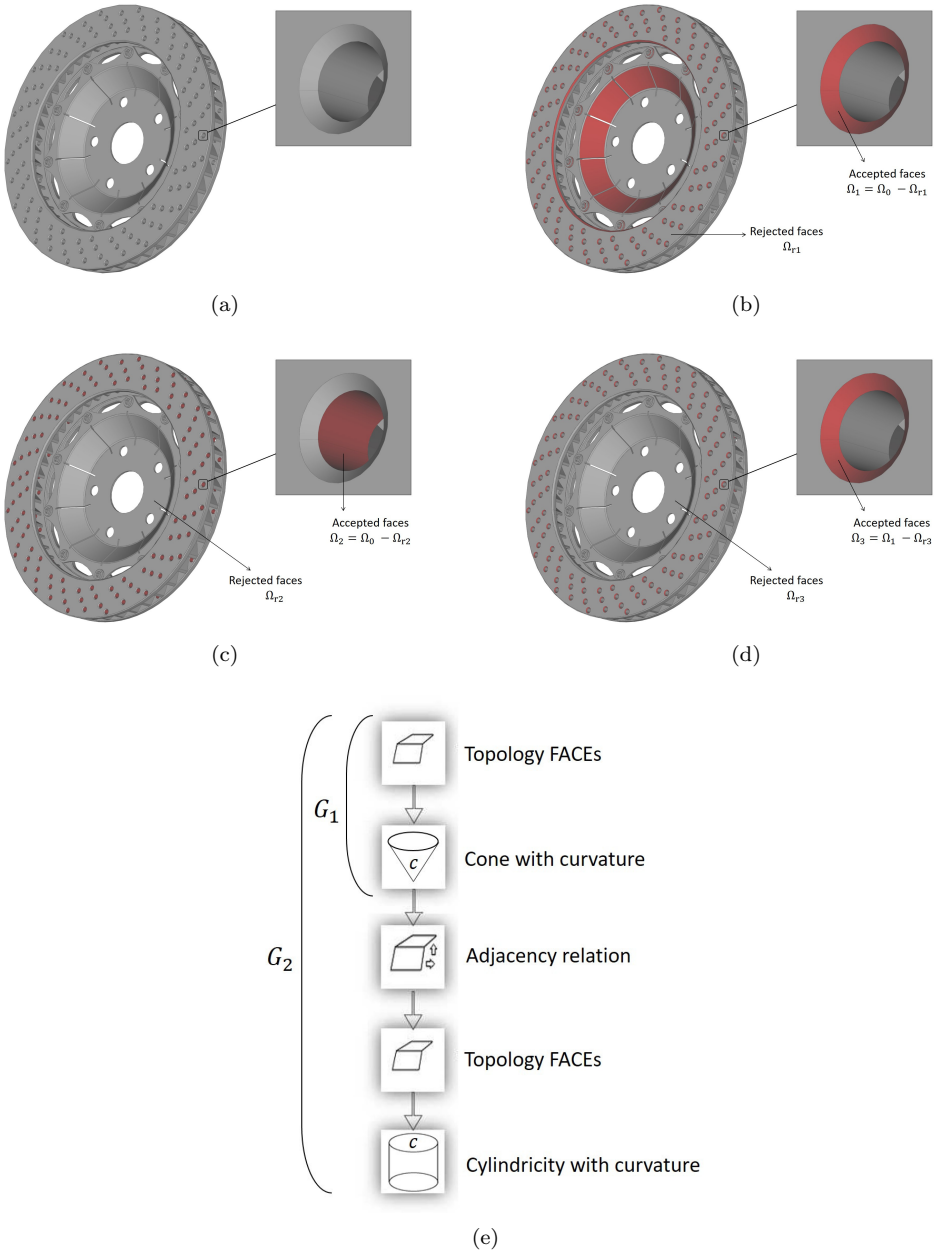

Figure 3.17: Results-Example 4: Recognition of holes chamfer surface in data set 4. (**a**) Initial data set Ω_0, (**b**) Reduced domain $\Omega_1 \subset \Omega_0$, (**c**) Reduced domain $\Omega_2 \subset \Omega_1$, (**d**) Reduced domain $\Omega_3 \subset \Omega_2$, and (**e**) Search graphs G_1 and G_2.

3.4 Discussion and Future Work

This manuscript presents the extension of the methodology for interactive user-reconfigurable FR introduced by the authors in [2], discussing the following aspects absent in [2]: complexity analysis and performance comparison with respect to other approaches in terms of time complexity, interactive graphic user interface, graph construction grammar, geometric filters development for the treatment of curved geometries (with examples), and industrial application with several examples. Our method prunes the search domain by extracting useful geometric information from topologies whose dimensions are 2, 1, or 0. The application of our methodology in an industrial process involving sheet metal parts for the automotive industry shows that: (i) the capacity of tuning the search graph to the specific definition of the objective feature allows for an efficient albeit specific feature recognition process; (ii) the presented work implies an improvement with respect to previous attempts of geometry-pruned Feature Recognition, which are limited to dimension two topologies mounted on prismatic geometries or do not use the geometric information of topologies other than FACEs; and, (iii) the use of geometric filters instead of STEP feature definitions allows for addressing the semantic loss problem. Our method is able to perform specific feature recognition in 3D CAD models with both planar and curved surfaces with an easy-to-use interactive methodology that allows the end-user to make use of previous knowledge of the part and features to improve the efficiency of the search.

Future work is required in the following aspects to improve the FR process: (a) deal with the problem of ambiguous definition of the search graph (from the user); (b) search graph building flexibility in the GUI; (c) robustness of graph parsing; and, (d) improving and expanding the geometric filters available. These improvements should precede the application of our method to the problem of identification of interacting features, which is not considered in this manuscript.

Author Contributions: Conceptualized and designed the algorithm, J.P.-C., O.B.-A., O.R.-S. and C.C; implemented the algorithm, J.P.-C. and O.B.-A; supervised the industrial application of the algorithm, J.P. and O.R.-S; implemented the geometrical aspects of this research, J.P.-C. and A.T. All the authors contributed to the writing of the article. All authors have read and agreed to the published version of the manuscript.

Funding: This work has been partially funded by the basic oriented research project LANGILEOK, financed by the Basque Government under the ELKARTEK program.

4

Digital Twin Tool for Fast pre-CFD Simulation and Visualization of Gerotor Pumps

Juan Pareja-Corcho[1,2], Aitor Moreno[2], Bruno Simoes[2], Asier Pedrera-Busselo[3], Oscar Ruiz-Salguero[1] and Jorge Posada[2*].

[1] Laboratory of CAD CAM CAE, Universidad EAFIT, Cra 49 no 7-sur-50, 050022 Medellín, Colombia

[2] Vicomtech Foundation, Basque Research and Technology Alliance (BRTA), Mikeletegi 57, 20009 Donostia-San Sebastian, Spain

[3] Egile AeroTransmissions, Kurutz-Gain Polígono Industrial Pol., 12, 20850, Gipuzkoa, Spain

applied sciences

IMPACT FACTOR 2.217

an Open Access Journal by MDPI

Context

A Virtual Prototype for Fast Design and Visualization of Gerotor Pumps. Juan Pareja-Corcho, Aitor Moreno, Bruno Simoes, Asier Pedrera-Busselo, Ekain San-Jose, Oscar Ruiz-Salguero , Jorge Posada Journal Applied Sciences, MDPI, ISSN 2076-3417, 2021, 11(3), 1190, (This article belongs to

the Special Issue 'Digital Twins in Industry'). url= https://www.mdpi.com/2076-3417/11/3/1190, doi= https://doi.org/10.3390/app11031190, Published online: 28 January 2021.
Indexing: ISI (Q2), SCOPUS (Q1), Publindex (A1)

Abstract

In the context of generation of lubrication flows, gear pumps are widely used, with gerotor-type pumps being specially popular, given their low cost, high compactness, and reliability. The design process of gerotor pumps requires the simulation of the fluid dynamics phenomena that characterize the fluid displacement by the pump. Designers and researchers mainly rely on these methods: (i) computational fluid dynamics (CFD) and (ii) lumped parameter models. CFD methods are accurate in predicting the behavior of the pump, at the expense of large computing resources and time. On the other hand, Lumped Parameter models are fast and they do not require CFD software, at the expense of diminished accuracy. Usually, Lumped Parameter fluid simulation is mounted on specialized black-box visual programming platforms. The resulting pressures and flow rates are then fed to the design software. In response to the current status, this manuscript reports a virtual prototype to be used in the context of a Digital Twin tool. Our approach: (1) integrates pump design, fast approximate simulation, and result visualization processes, (2) does not require an external numerical solver platforms for the approximate model, (3) allows for the fast simulation of gerotor performance using sensor data to feed the simulation model, and (4) compares simulated data vs. imported gerotor operational data. Our results show good agreement between our prediction and CFD-based simulations of the actual pump. Future work is required in predicting rotor micro-movements and cavitation effects, as well as further integration of the physical pump with the software tool.

Keywords: digital-twin, gerotor pump, hydraulic-systems, simulation, computer-aided design.

Abbreviations

LP	Lumped Parameter.
CFD	Computational Fluid Dynamics.
P_i	Pressure at chamber i.
A_i	Area at chamber i.
V_i	Volume at chamber i.
Q_i	Net flowrate at chamber i.
$A_{i,out}$	Shared area between chamber i and output port.
$A_{i,in}$	Shared area between chamber i and input port.
C_d	Discharge coefficient.
$C_{d,max}$	Maximum discharge coefficient.
β_{eff}	Effective bulk's modulus of working fluid.
ρ_{eff}	Effective density of working fluid.
ν	Kinematic viscosity of working fluid.
μ	Dynamic viscosity of working fluid.
Re	Reynold's number.
Re_{crit}	Critical Reynold's number.
Dh	Hydraulic diameter.
p_{in}	Pressure at input port.
p_{out}	Pressure at output port.
ω	Angular speed of inner gear.

4.1 Introduction

Gerotor pumps play an important role in the aerospace industry, particularly in the processes of cooling, lubrication, and fuel boost and transfer. In other sectors, the gerotor pumps are operated in a wide range of applications, such as dosing and filling technologies in pharmacy and medicine, dispensing technologies and coating applications in manufacturing, among others. The popularity of such pumps in industrial applications arises from the fact that gerotor pumps represent a reasonable compromise in terms of compactness, reliability, cost, and versatility [72]. The working principle of a gerotor pump is based on the interaction between a pair of toothed gears with trochoidal envelope profiles. The relative movement between the profiles generates a series of chambers with varying volume that perform a cycle of suction and delivery actions (in interaction with input and output ports), thus effectively producing a volumetric flow (see Figure 4.1).

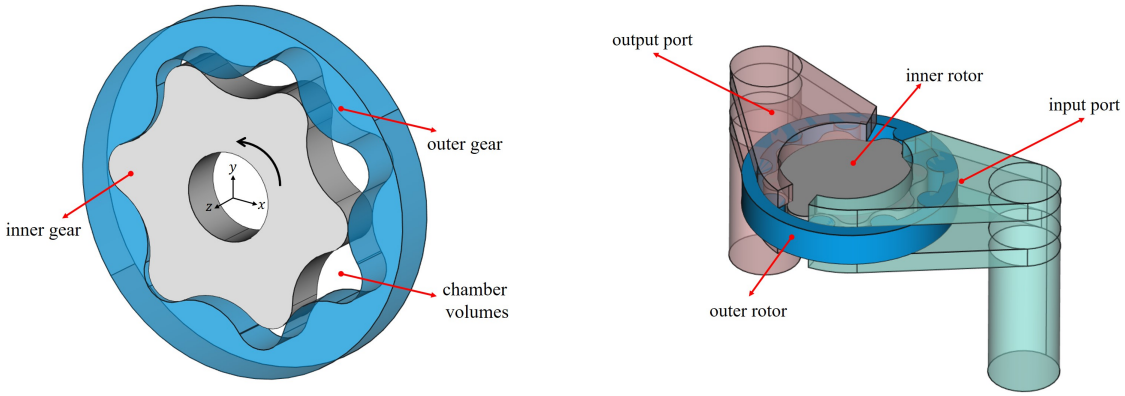

(a) (b)

Figure 4.1: Gerotor pump general architecture: (**a**) inner and outer gear, (**b**) inlet/outlet disposition in pump.

The current design process for gerotor pumps commonly involves: (i) a *geometric modeling* step in a CAD environment, (ii) a *design verification* phase using fluid mechanics simulations to validate the efficiency and other desired characteristics of the pump, and (iii) a *physical testing* phase to verify the predicted characteristics of the pump in a real test bench once the design has been validated through a simulation tool. This process can be considerably time-consuming, due to the large amount of time that is required in the design verification stage. The design engineer must mesh the complex geometry of the volume chambers each time that the design is changed and perform a time-consuming simulation. In most design cases, the simulation of a geometric configuration takes up to a day to generate results. The described workflow hinders the effectiveness of rapid design methodologies or the easy testing of a large number of geometric configurations of the pump in a reasonable time.

Implementation. In this manuscript, we present the implementation of a virtual prototype of a Gerotor pump designed to be integrated with data measured in an experimental setup in order to improve the established design process. Our implementation does not constitute a full Digital Twin, but rather will be a step towards a fully functional Digital Twin tool that reproduces the behavior of the real pump. This virtual prototype allows for a rough design condition vs. performance appraisal, thus enabling the design and testing scenarios. Once the designer is satisfied with this approximated design vs. performance ratio, a more precise CFD simulation process would take place. An important current feature of the virtual prototype tool presented is the import and display of the sub-sequent CFD simulation results and experimental data measured in a real pump, for the benefit of the designer manufacturer and client. This feedback of the CFD simulation results might be included in a numerically oriented closed loop at the design stage. At the present time, we only report visual CFD data feedback. The implemented tool is able to use data that were measured in the experimental setup to feed the fast virtual prototype. Differences between the virtual prototype state variables and measured state variables allow for several activities: (a) to modify the pump design, (b) to control the actual pump, and (c) to feed satisfactory virtual prototype parameters into parametric or constraint-driven CAD models to obtain a full Boundary Representation of the Gerotor pump. Notice that (c) streamlines the design-for-gerotor process and

avoids the need for a external CAD application.

The manuscript is divided, as follows: the Section 4.2 reviews the available literature in the context of physical simulation of gerotor pumps and Digital Twin implementations. Section 4.3 introduces the experimental setup of the pump, the lumped parameter model, and the virtual prototype tool. Section 4.4 presents the comparison between our predictions and a Computational Fluid Dynamics simulation used as ground truth. We do not address the comparison with respect to the experimental data, because we cannot measure the comparison variable in our experimental setup. Section 4.5 concludes the manuscript and discusses possible future developments in both the virtual prototype and its integration within a full Digital Twin tool.

4.2 Previous Works

In this section, we review the literature in two dimensions: (a) methods for fluid dynamics simulation in gerotor pumps and (b) implementations of virtual prototypes in Digital Twin oriented tools.

4.2.1 Fluid Mechanical Simulation

Several approaches have been proposed to simulate the performance of gerotor pumps, depending on the level of detail required. Most previous work relies on two methods for the fluid simulation: (i) lumped parameters models (LP) and (ii) computational fluid dynamics models (CFD), with each one exhibiting different performances regarding time and memory complexity.

CFD models: computational fluid dynamics models use specialized software to solve the Navier–Stokes equations in a discretized domain. CFD models can be classified in two categories: (i) two-dimensional (2D) models and (ii) three-dimensional (3D) models. Castilla et al. [73] and Houzeaux et al. [74] presented 2D CFD models for the simulation of rotary pumps that present accurate results with respect to an experimental setup. Recently, 3D simulations of the pump have been performed in order to analyze specific aspects of the pumps design, such as: (a) profile geometry optimization [75, 76], (b) discharge coefficient calculation [77], and (c) fluid leakage due to clearances [78]. The main advantages of CFD based methods are: (i) detailed description of the fluid's behavior inside the cavity of the pump and (ii) very accurate prediction of the effect of cavitation and fluid–body interaction on performance. The main disadvantages of CFD methods are: (i) large simulation time and memory requirements, (ii) the requirement to remesh the entire domain in each step of the solution, and (iii) the difficulty to mesh appropriately the inter-teeth clearance domain [73].

LP models: lumped parameter models discretize the pump in a number of control volumes, where each CV (control volume) corresponds to a cavity of the pump. The mass and energy conservation equations are used to integrate the pressure in each control volume. The pressure inside each control volume will depend on the instantaneous volume of the chamber and net flowrate of fluid through its surface. Pellegri et al. [79,80] presented a simple lumped parameter model that was mounted on AMESIM software, coupled with a geometric module that calculates the instantaneous areas and volumes of the chambers. The results show good agreement between predicted and measured data. Shah et al. [81] presented a lumped parameter model in AMESIM software for the prediction of cavitation effects on the pump simulation; the results show that the model is accurate in predicting the effect of cavitation phenomena on the overall performance of the system. The main advantages of the lumped parameter approach are: (i) the low time and memory complexity and (ii) the flexibility to integrate with larger hydraulic circuits [72, 79, 80]. The main disadvantages of the lumped parameter approaches are: (i) the results are coarse with respect to CFD methods and (ii)

calibration of the model vs. experimental data is needed, which makes this approach unsuitable for detailed analysis of local behavior of fluid [82].

4.2.2 Digital Twins and Virtual Prototypes in Gerotor Applications

Digital Twins are virtual abstractions of physical products, processes, or phenomena very commonly used in the context of Industry 4.0 [83]. Digital Twins are a valuable tool in digital design and manufacturing, as they allow for prediction of system performance and simulation/optimization. Relatively few applications of Digital Twin methodology are found in industrial contexts [84], opening opportunities for wider adoption of Digital Twins in industries, such as fluid power systems. The use of accelerated coarse simulations for fast decision making, although not being entirely similar to the concept of Digital Twin, is being explored in other industrial contexts, such as quality control in manufacturing [85, 86].

The lumped-parameter models that have been cited in the previous sections are usually implemented in specialized commercial software. This restriction limitates their feasibility towards a fully functional Digital Twin tool that integrates data from an experimental test bench. In the case of lumped parameter models, the design engineer must express the pump in a CAD environment and then import the geometric data into a differential equation solver (e.g., AMESIM [80]). In the case of CFD models, several commercial codes are used in the solution of the Navier–Stokes equations, including PumpLinux, ANSYS Fluent, and CFX (all appearing in Ref. [82]). So far, we have found no standalone fully-integrated implementations of gerotor pump simulation environments that suits our design needs.

4.2.3 Conclusions of Literature Review

Two approaches are commonly used in the context of gerotor pump simulation: (i) Lumped Parameter (LP) models and (ii) Computational Fluid Dynamics (CFD) models. The lumped parameter models allow for the fast simulation of pump performance at the price of loss of accuracy and detail. CFD models allow for very accurate simulation of pump performance with detailed information regarding in-chamber heterogeneity, at the expense of large simulation time and complexity. Because of its accuracy, it is common to use CFD as a ground truth value for pump experiments when no experimentally obtained comparison data are available. We use CFD as our point of comparison for the reasons expressed above and the availability of CFD software simulation. Furthermore, we found that implementations of both approaches are: (i) dependant on proprietary commercial software and (ii) not easily integrated with other standalone non-commercial design and optimization tools in the context of Digital Twins tools.

As a response to such shortcomings, we present the implementation of a virtual prototype for a gerotor pump, which also allows for the integration of measured data, thus enabling the functioning of a Digital Twin. Our implementation: (1) integrates pump design, fast approximate simulation, and result visualization processes, (2) does not require an external numerical solver platforms for the approximate model (as other approaches do), (3) allows for the fast simulation of gerotor performance, and (4) feeds the simulation model with data measured in an experimental setup to improve the accuracy of the model. Several variables can be used to assess the pump behavior, including, among others, maximum pressure, torque, and power. We use the maximum pressure in the pump as our comparison variable since (1) it is a variable of interest for the pump manufacturer and the variable that our model predicts and (2) the comparison with other variables

(e.g., torque) would require specialized proprietary software. This software is not available to the industry manufacturer. See Implementation in the Introduction section.

4.3 Methodology

For our Digital Twin (DT) implementation, we have defined a three step workflow: (i) the design engineer inputs the values for the parameterization of pump design into the Geometry Configurator, (ii) the geometric model of the pump (inner and outer gears) is generated, and (iii) the virtual prototype performs the fast simulation of the pump with the geometric data and experimental data being measured from the test bench (see Figure 4.2). Please see the Abbreviations section immediately before the References section to find the meaning for the symbols used.

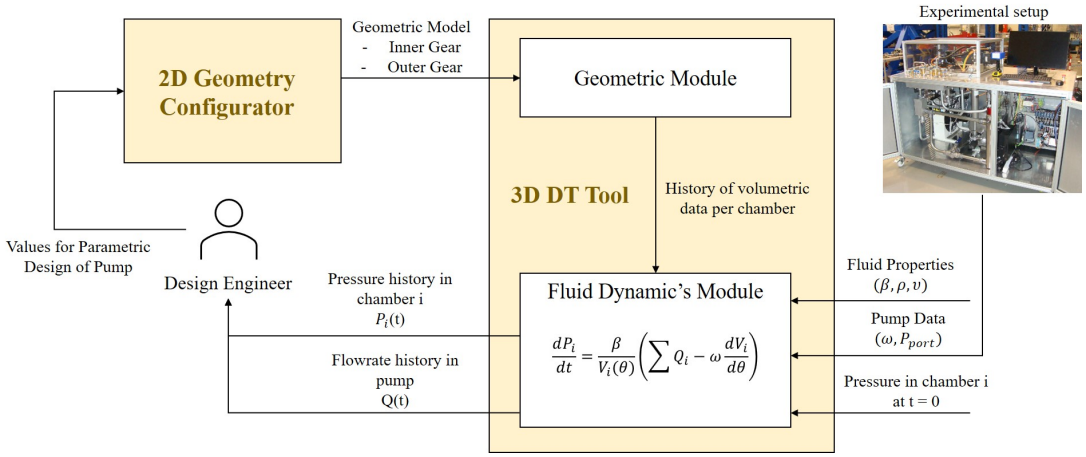

Figure 4.2: Implemented Tool Architecture and Workflow.

This section is divided in three parts: (1) we present the experimental setup where we show the data collection setup used to feed the virtual prototype tool, (2) we explain the geometric model, showing the generation of the gerotor geometric model and the calculation of geometric quantities such as the history of chamber volumes and areas, (3) we present the fluid dynamics module, where we lay out the foundations of the simulation model and (4) we discuss the software tool that integrates the virtual prototype model, including 3D visualization, with the data being collected from the experimental setup and external CFD simulations.

4.3.1 Experimental Setup

The contact point between the physical pump and the computational modeling is the testing bench. The experimental setup hosts the sensors that are used to collect performance data and feed it to the simulation model. Figure 4.3 presents the testing bench setup used and a manufactured pump mounted in the bench with a translucent cover.

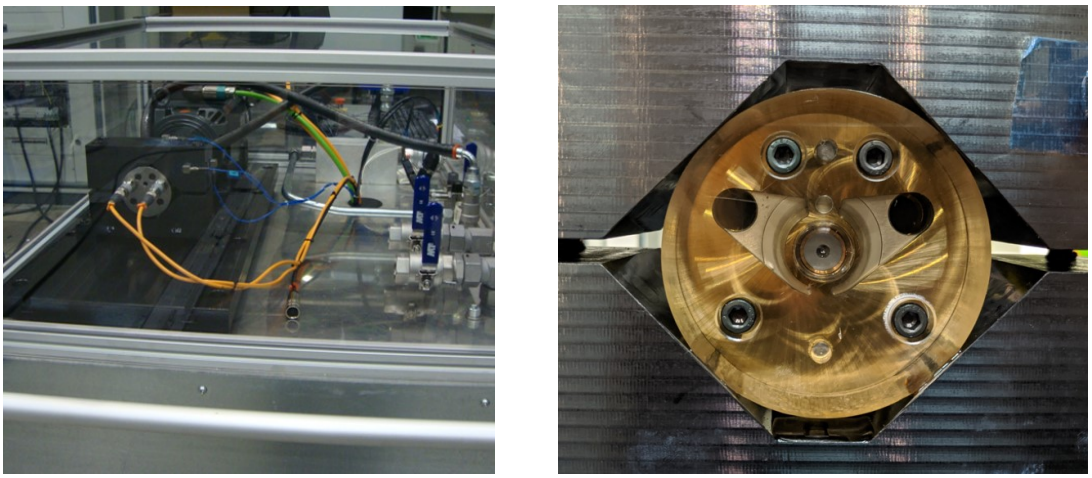

(a) (b)

Figure 4.3: Experimental setup: (**a**) testing bench and (**b**) physical pump mounted on the test setup (translucent cover).

Pressure sensors that are located in the input and output ports measure the pressure value to be fed to the virtual prototype (as shown in Figure 4.2). Further integration of the data that were collected in the testing bench for variables other than pressure with the simulation model is still to be addressed.

4.3.2 Geometric Model

The internal profile of the gerotor is generated according to the parameterization proposed by Ref. [87]:

$$x_i\left(\alpha_{pc}\right) = R_2 \cos\left(\frac{1}{Z-1}\alpha_{pc}\right) \pm e\cos\left(\frac{Z}{Z-1}\alpha_{pc}\right) - \frac{S}{m}\left[R_2\cos\left(\frac{1}{Z-1}\alpha_{pc}\right) \pm r_2\cos\left(\frac{Z}{Z-1}\alpha_{pc}\right)\right] \tag{4.1}$$

$$y_i\left(\alpha_{pc}\right) = -R_2 \sin\left(\frac{1}{Z-1}\alpha_{pc}\right) \mp e\sin\left(\frac{Z}{Z-1}\alpha_{pc}\right) + \frac{S}{m}\left[R_2\sin\left(\frac{1}{Z-1}\alpha_{pc}\right) \pm r_2\sin\left(\frac{Z}{Z-1}\alpha_{pc}\right)\right] \tag{4.2}$$

$$m = \sqrt{r_2^2 + R_2^2 \pm 2r_2R_2\cos\alpha_{pc}} \tag{4.3}$$

where the parameter $\alpha_{pc} \in [0, 2\pi]$ corresponds to the turning angle of the rotor. Figure 4.4 shows the resulting shape of the internal profile as the trace of contact point P', whose position is determined by the radii R_2 and r_2, the eccentricity e, and the number of chambers Z. In Figure 4.4, the external profile is determined by a set of outer circumferences that are truncated by a larger cutting circumference.

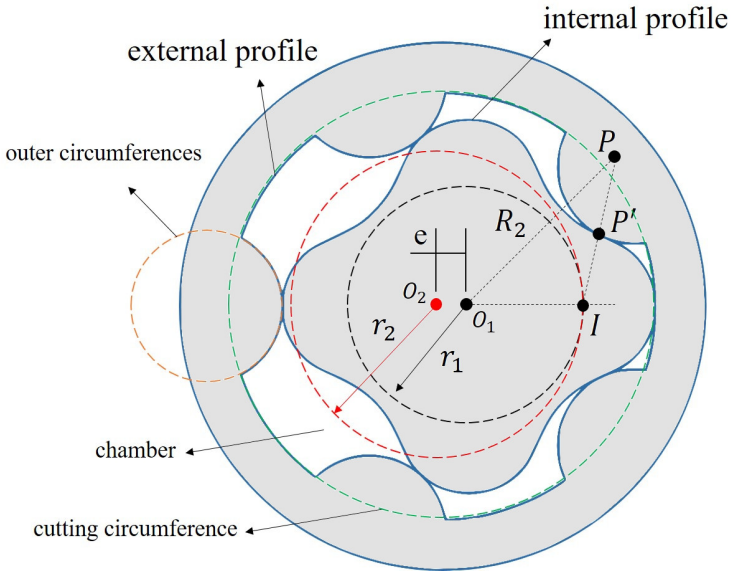

Figure 4.4: Parameterization of internal profile shape as in Equation (4.2).

This construction method of the external profile, even though simple and widely used, limits the performance of the pump, as the resulting shape does not mesh perfectly with the internal profile shape [88]. We have implemented an additional method to build the external profile as the conjugated curve of the internal shape.

Suppose the curve C that corresponds to the internal profile (Equations (4.1) and (4.2)) is put through a series of affine transformations that are defined by the rolling without slipping of the circumference defined by r_1 with respect to the circumference defined by r_2 in Figure 4.4. Subsequently, the external profile shape will be defined as the envelope curve of the locus of C as it moves through the rotation domain.

Figure 4.5 shows the locus of curve C, as generated by the movement of the circumferences. The envelope curve of the locus can be used as the external profile shape, with the advantage that by using this external shape both curves mesh perfectly, hence improving the performance by avoiding fluid recirculation. Once the inner and outer profile shapes are defined, the geometric quantities of each chamber are calculated by sampling both the internal and external curve to form a closed polygon, finding the area A_i and perimeter P_i of the polygon corresponding to chamber i.

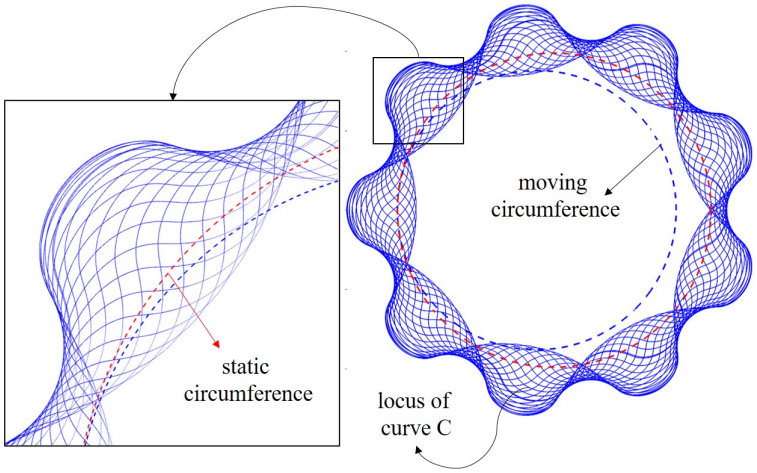

Figure 4.5: Locus of the internal profile curve C.

4.3.3 Fluid Dynamics Module

We discretize the flow domain in several control volumes to obtain a lumped parameter model of the pump, as shown in Figure 4.6. We assume the fluid properties within each control volume (CV) to be homogeneous, but not constant in time, effectively treating each control volume as the basic domain of simulation. Notice that, as the pump rotates, the geometry of the control volumes changes; therefore, the model requires a constant update of the geometric calculations for each control volume (area, perimeter) as the position of the pump changes (see Figure 4.2).

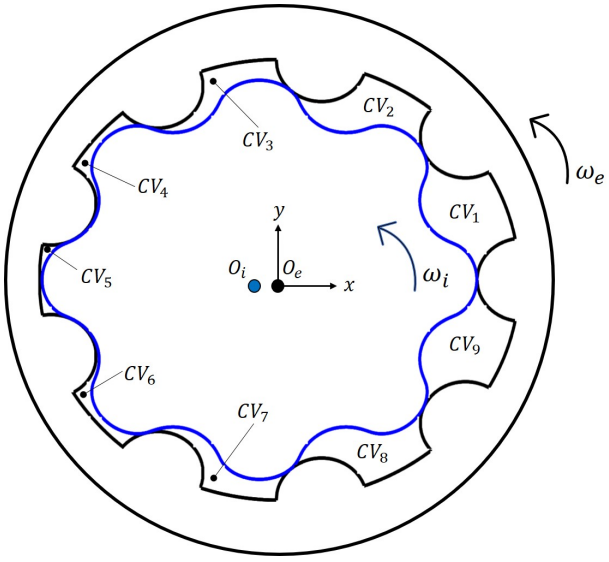

Figure 4.6: Control Volume discretization of the gerotor pump.

By the principle of the conservation of mass and energy, along with Reynold's transport theorem, it is possible to derive an expression for the change of pressure within a control volume:

$$\frac{dp}{dt} = \frac{\beta_{eff}(p)}{V(\theta)} \left(\sum Q_i - \omega \frac{dV}{d\theta} \right) \tag{4.4}$$

We omit the derivation of such an expression, since it is beyond the scope of our paper, the interested reader can find a thorough explanation in Ref. [82]. The net flowrate that flows through the boundary of a control volume needs to be calculated in order to integrate Equation (4.4), and since the volume and volume derivative at angle θ are provided by the geometric module. We consider two types of flows through the boundary of a control volume (Figure 4.7):

1. *Input/Output flow*: fluid flowing from the input port to the inside of the pump (charge) or from the inside of the pump to the output port (discharge).
2. *Fluid leak flow*: fluid flowing from one chamber to another due to imperfect sealing that results from manufacturing defects and design constraints.

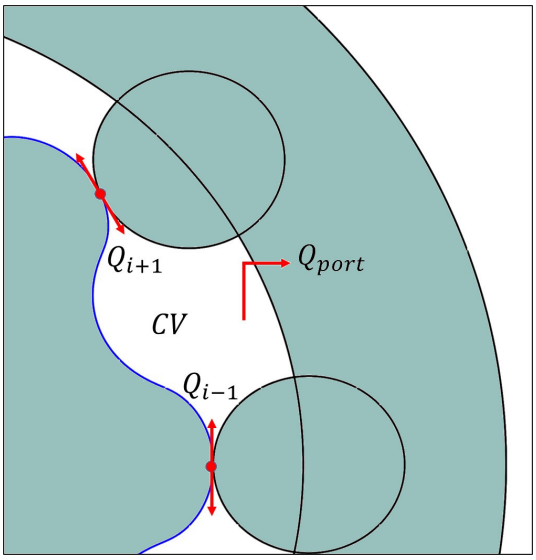

Figure 4.7: Types of flows through the boundary of a control volume.

The flow between the control volume and the input/output port is modeled as the flow through a variable geometry orifice subject to a difference in pressure. The pressure at the input and output ports is fed to the numerical model with data that were collected from the experimental testing bench, while the control volume pressure varies according to Equation (4.4). The flowrate in this situation can be obtained as:

$$Q_{in} = C_d A_{i,in} \sqrt{\frac{2\,(P_i - P_{in})}{\rho_{eff}}} \tag{4.5}$$

$$Q_{out} = C_d A_{i,out} \sqrt{\frac{2\left(P_i - P_{out}\right)}{\rho_{eff}}} \tag{4.6}$$

Notice that, since a control volume only interacts with one of the ports at any given time, the net port flowrate Q for a control volume is equal to Q_{in} or Q_{out}, depending on the position of the control volume at the time of analysis. The calculation of the discharge coefficient C_d depends on the value of the Reynold's number Re and the hydraulic diameter D_h at such a time. The hydraulic diameter D_h and the Reynold's number Re are calculated, as follows:

$$D_h = \frac{4A_i(\theta)}{P_i(\theta)} \tag{4.7}$$

$$R_e = \frac{D_h}{\nu} \sqrt{\frac{2\Delta P}{\rho_{eff}}} \tag{4.8}$$

Finally, the discharge coefficient C_d is estimated while using an experimental expression (Ref. [82]):

$$C_d = C_{d\,\max} \tanh\left(\frac{2R_e}{R_{ecrit}}\right) \tag{4.9}$$

where $C_{d\,\max}$ is the maximum discharge coefficient and R_{ecrit} is the critical Reynolds number, which indicates the transition between laminar and turbulent regime. Values for constants $C_{d\,\max}$ and R_{ecrit} can be found in the literature as a function of conditions of the pump [79]. This flow between adjacent control volumes that should be nominally tight is enabled by the small gap between the rotors at their maximal approximation position. These gaps are necessary for ensuring rotation and limit friction and wear. The resulting fluid migration between adjacent chambers is caused by:

1. Difference of pressure between adjacent control volumes (Poiseuille flow).

2. Difference in angular speed between inner and outer rotor (Couette flow).

Typically, the gap between rotors at contact points is very small when compared to the overall size of the pump. The curvature radii at the throat are much larger than the throat gap. Therefore, (1) and (2), above, may be modeled by assuming that the approaching teeth form a constant clearance gap between two parallel plates (Figures 4.8 and 4.9).

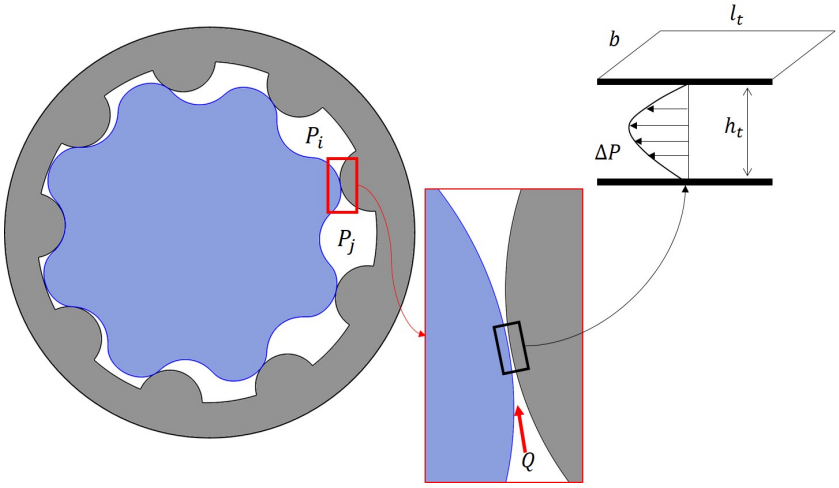

Figure 4.8: Pouiseuille flow between adjacent control volumes.

Figure 4.8 shows the working principle of the Poiseuille flow in the pump case, where two static plates of length l_t and width b are separated by a distance h_t. The difference in pressure between adjacent control volumes induces a flow Q_p that can be obtained as:

$$Q_p = b\frac{\Delta P(\frac{h_t}{2})^3}{12\mu L} \tag{4.10}$$

Notice that width b corresponds to the length of the pump profiles in the z direction. The distance h_t is estimated by the geometric module as it may vary for each contact point throughout the rotation of the rotors. As length l_t cannot be directly measured in the geometric model, we estimate l_t as a function of h_t. Starting from the point of minimum distance h_t, we move outwards through the profile curves to the point where the distance between rotors is $h_t* = (1+\epsilon)h_t$. Once such points are found, the length l_t is assumed to be the Euclidean distance between the points found. This approximation has shown to be effective for values of ϵ around 0.1 [79].

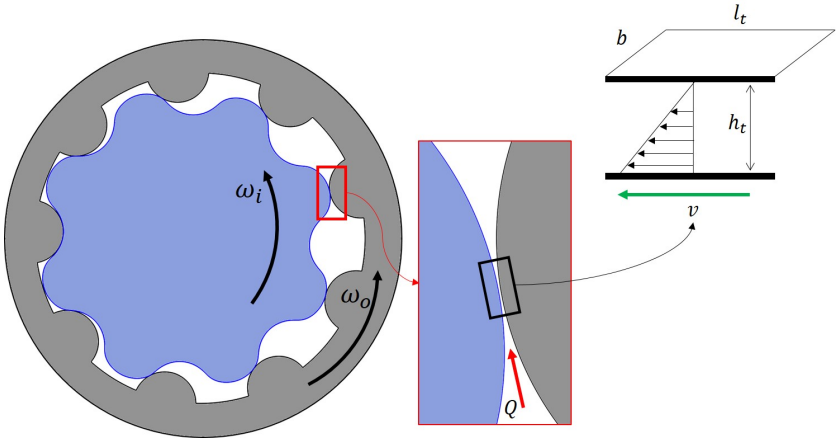

Figure 4.9: Couette flow between adjacent control volumes.

Figure 4.9 shows the working principle of the Couette flow. Two parallel plates having relative velocity with respect to each other produce a flowrate between them through the viscosity of the fluid and shear stress induced by the relative movement of the plates. The Couette and Poiseuille flows (Figures 4.8 and 4.9) both result in a fluid exchange between adjacent control volumes, therefore affecting the net flowrate through their borders and their pressures. Finally, as the pump usually operates in a low pressure range, the variance of effective fluid properties (bulk modulus, density) in hydraulic oil with respect to the instantaneous pressure [89] inside a control volume must be taken into account:

$$\beta_{\text{ef}} = \frac{\beta_{\text{oil}}}{1 + \alpha \cdot \left(\frac{p_0}{p}\right)^{\frac{1}{\kappa}} \cdot \left(\frac{\beta_{\text{oil}}}{\kappa \cdot p} - 1\right)} \tag{4.11}$$

$$\rho_{\text{ef}} = \frac{\alpha \cdot \rho_{\text{air},0} + (1-\alpha) \cdot \rho_{\text{oil},0}}{\alpha \cdot \left(\frac{p_0}{p}\right)^{\frac{1}{K}} + (1-\alpha) \cdot \left(1 + \frac{m \cdot (p - p_0)}{\beta_{oil}}\right)^{-\frac{1}{m}}} \tag{4.12}$$

where β_{oil}, ρ_{air}, and ρ_{oil} are the properties of the oil and air at atmospheric conditions, respectively. p_0 is the atmospheric pressure, α is the void fraction, and κ is the polytropic constant of air.

4.3.4 Software Tool

The Digital Twin (DT) tool implements two functionalities: a *2D geometry configurator* and a *3D data tool*. The 2D geometry configurator allows for the design engineer to define a new geometry for the profiles of the inner and outer gears according to a set of parametric variables. The 3D data tool converts the model that is defined in the 2D geometry configurator to a full B-Rep model for simulation and visualization purposes of both (i) data simulated from our pre-CFD simulation model and (ii) data imported from CFD simulations or test bench.

Figure 4.10 shows the visualization of the parameterized pump in the interface of the 2D geometry configurator tool. The tool allows for the design engineer to input the desired set of values for the parametric variables of Equation (4.2). Our application automatically generates both the

conjugated design (Figure 4.10a) and the classic design (Figure 4.10b). Both types of design, as well as other geometric configurations, are easily explorable in the 2D visualization canvas.

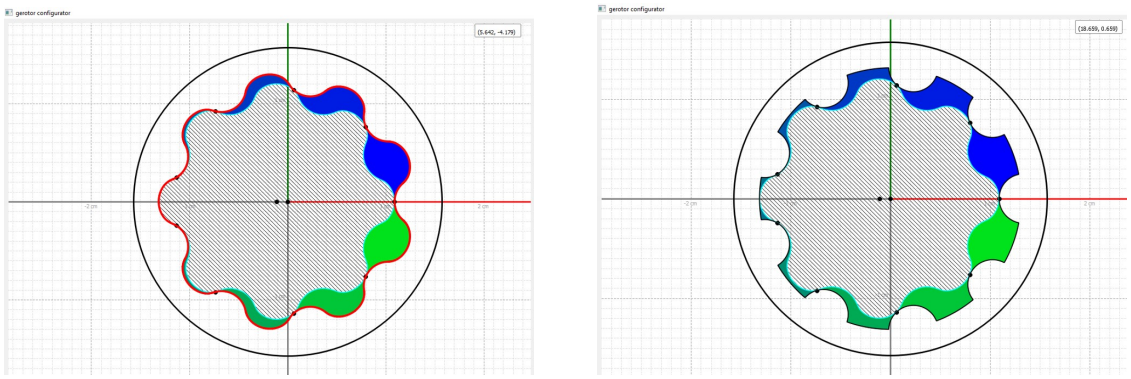

(a) (b)

Figure 4.10: Visualization of parameterized pump in the two-dimensional (2D) geometry configurator interface: (**a**) pump with conjugated external profile and (**b**) pump with classic external profile.

In addition to the discretized geometric model of the inner and outer gears, the geometry configurator calculates the shape of the resulting chambers for any given angle of the rotation of the pump. The configurator allows the user to interactively rotate the pump position with a slider, as well as to visualize and record the change in the area of each one of the chambers.

The ports and chambers geometries must be well-aligned for the correct calculation of the intersection area between the chambers and the ports. The geometry of the input/output ports (shown in Figure 4.11) of the pump is calculated from the geometry of the inner and outer gear geometries in order to ensure the alignment. The geometries calculated by this application (gear, chamber, and port geometry) are automatically imported into the 3D data tool for simulation purposes. The CAD models are also exported to external files.

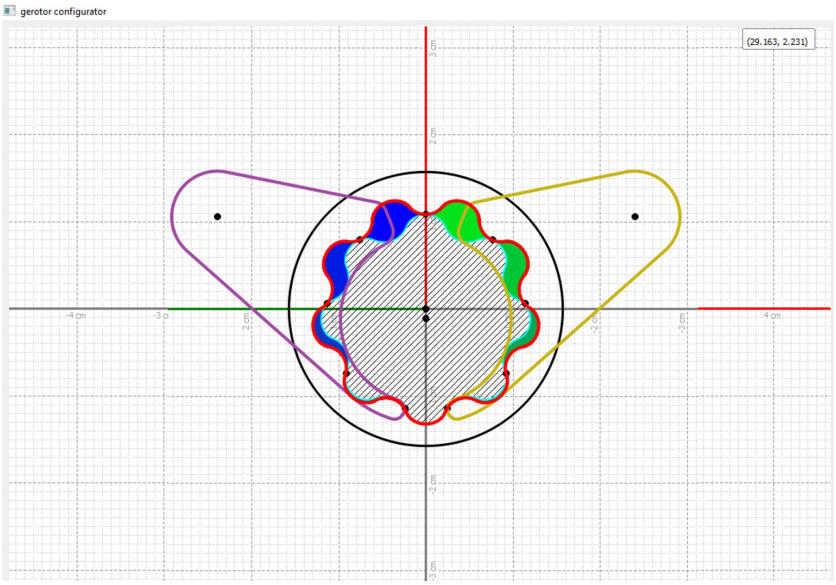

Figure 4.11: Gerotor design with input/output ports.

Figure 4.12 shows the interface that is devised for the toolkit that was introduced in [90,91] to enable the virtual prototype. The interface is built with Qt™ library and it comprises several panels: (i) the *3D visualization panel*, which allows for the visualization of the pump geometry (gears, ports, and chambers) and the animation showing the rotation of the pump through a pumping cycle, (ii) a *hierarchy panel* that shows the hierarchy tree of the geometric model and allows the user to select and highlight geometric entities, (iii) a *settings panel* in which the user inputs the fluid properties, operating conditions, and initial pressure conditions that are necessary to perform the fast pre-CFD simulation (see Figure 4.2), iv) a *simulated data panel* that displays the results from the fast simulation model, and v) a *measured data panel* that displays the results of the variables that are imported to the virtual prototype tool, whether measured in the test bench or simulated by the CFD software.

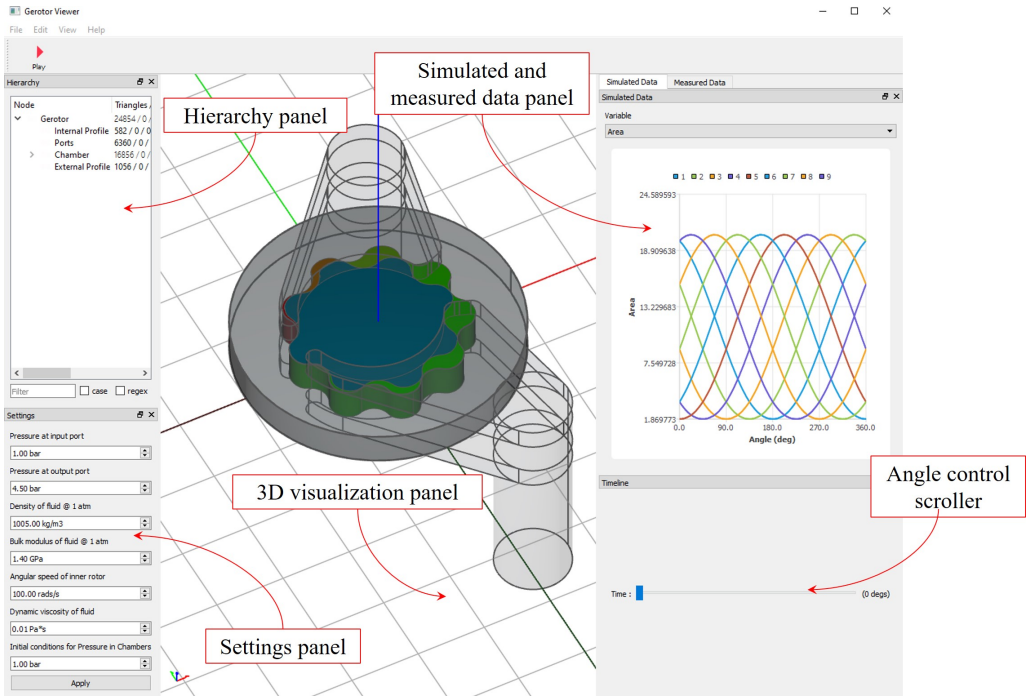

Figure 4.12: Three-dimensional (3D) data tool interface.

The 3D visualization panel enables design engineers to examine the three-dimensional behavior of the pumps for the parameters that are defined in the Geometry Configuration interface. Notice that the shape of the chambers must be recalculated each time the pump is set to a new angle position. Figure 4.13 shows the high degree of flexibility that can be achieved in the visualization of the different components of the pump geometry.

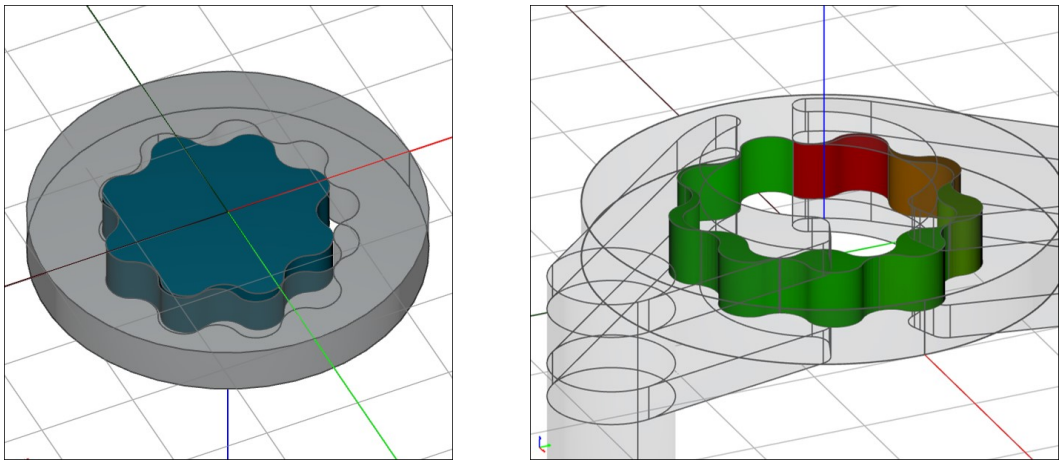

(a) (b)

Figure 4.13: Geometry visualization: (**a**) inner and outer gear of the pump, (**b**) fluid chambers with transparent ports.

In Figure 4.13b, the color of each chamber is related to the pressure that is calculated by the simulation model. The tool also allows for the design engineer to import data from the CFD simulations and test bench tests with the objective of integrating and comparing performance data (both predicted and measured) in the same software environment. Figure 4.14 shows the data for a measured variable that was imported from an external CFD simulation, as visualized within the software tool. It is possible to import external data in the form of the widely used CSV format or while using a special text formatting that was specifically tuned for our application.

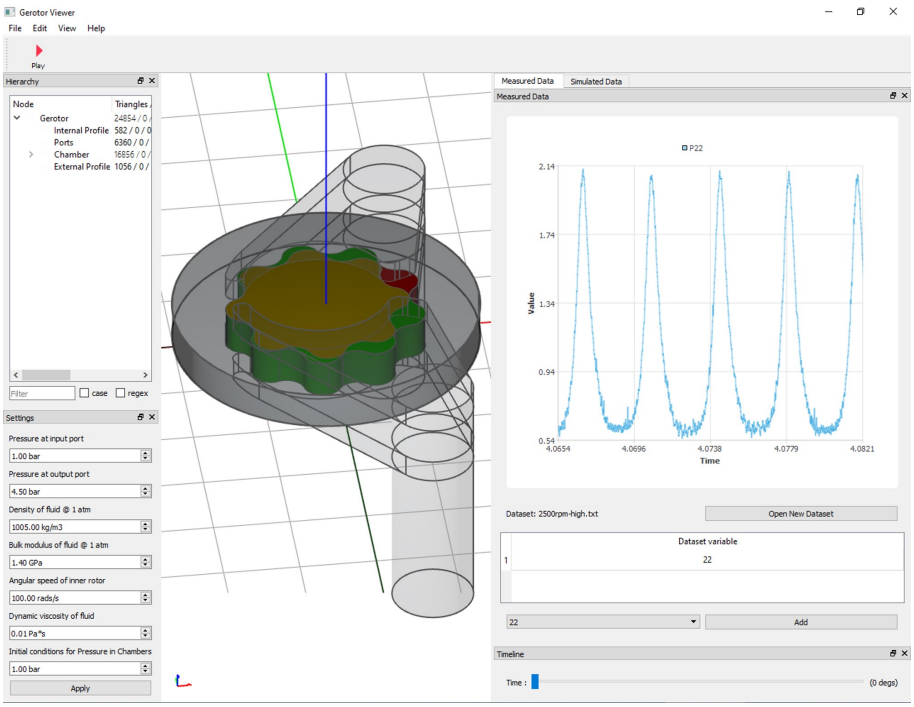

Figure 4.14: Example of the pressure data collected from the experimental setup sensors.

4.4 Results

We present the results of a design case while using the presented virtual prototype tool to design and simulate a gerotor pump. We also compare the obtained results with the data imported from an external CFD simulation for the same geometry, fluid properties, and operating conditions. Figures 4.15 and 4.16 present the volumetric data that were calculated by our tool for the pump design used in this test run.

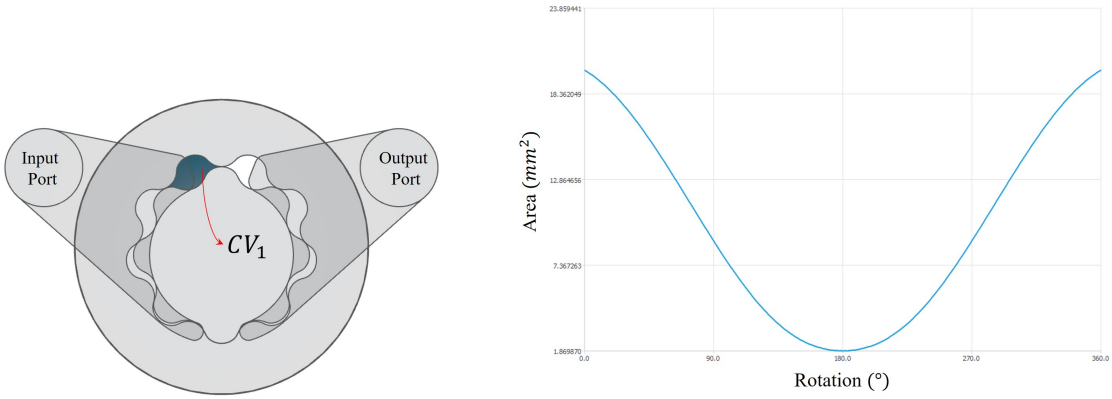

(a) (b)

Figure 4.15: Volumetric data results from the virtual prototype: (**a**) profile of geometry with highlighted chamber (CV_1) and (**b**) history of area in a z-cut for selected chamber.

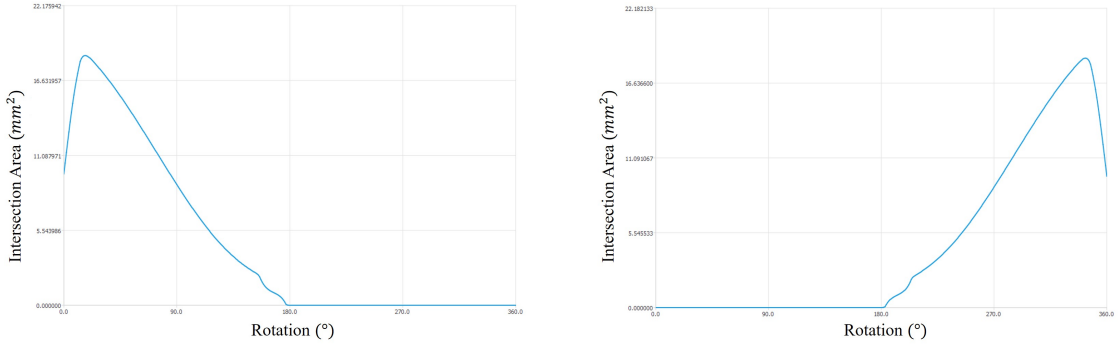

(a) (b)

Figure 4.16: Volumetric data results from the virtual prototype: (**a**) history of intersection area between chamber CV_1 and input port and (**b**) history of intersection area between chamber CV_1 and output port.

Figure 4.15a shows the selected analysis chamber. In this case, we have selected the maximum volume chamber when the pump is at initial position $t = 0$, even though our tool can perform the geometric analysis of all chambers simultaneously. Figure 4.15b shows the area evolution for the analysis chamber. Notice that it starts with the maximum value and diminishes until it reaches the minimum value for chamber area around halfway through a revolution. The minimum value for the area is not exactly zero because of the gaps in the meshing between the internal and external rotors described in the previous section. The area then rises until it reaches the maximum value once the revolution of the pump is completed. Figure 4.16a shows the intersection area between the analysis chamber and the input port (area through which the working fluid enters the pump). Notice that the intersection area increases at first, because, at initial position, the port and the

chamber are only partially overlapped (as seen in Figure 4.15a). When the chamber is no longer overlapping with the input port and has started discharging fluid (overlapping with the output port), the intersection area with the input port becomes zero. The same analysis corresponds to the intersection area between the chamber and output port shown in Figure 4.16b. Figure 4.17 shows the history of areas for all chambers in the pump; the periodicity is explained by the cyclic design of the pump.

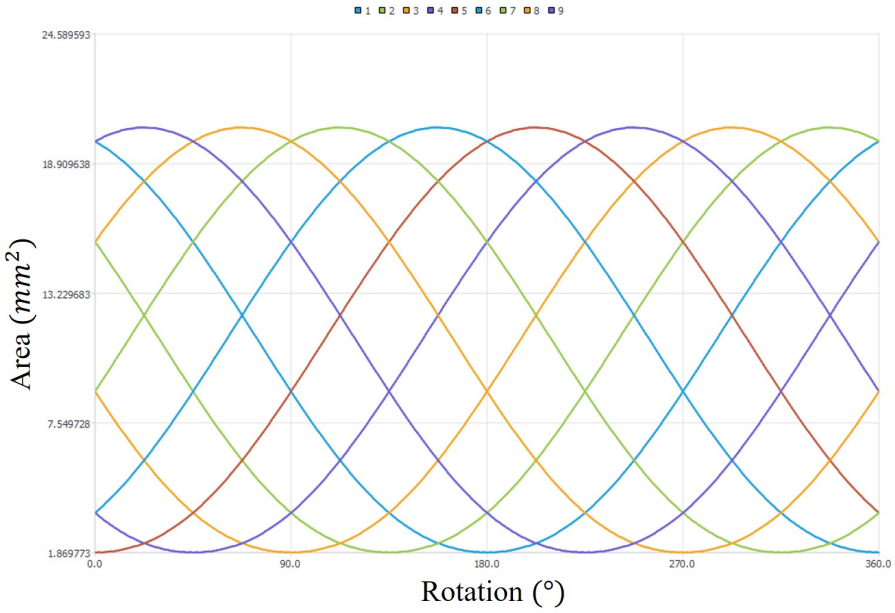

Figure 4.17: History of area for all 9 chambers in the pump.

We now discuss the results of a fluid dynamics simulation with our virtual prototype tool. The fluid properties, operating conditions and initial pressure conditions that are used for the simulation presented, are described in Table 4.1:

Figure 4.19 shows the history of calculated pressure inside an analysis chamber. Notice that the analysis chamber CV_1 (Figure 4.19a) is initially near the maximum volume position and, therefore, the initial pressure $P_{t=0}$ will be low (near input port pressure). As the pump rotates, the volume of the chamber reduces and increases the pressure inside the chamber. The maximum value of the pressure in chamber is reached in the minimum volume position and, once the analysis chamber enters the discharge cycle, the pressure starts to reduce as a result of the discharge of fluid and increase in volume of the chamber itself.

Table 4.1: Simulation conditions for test operating point.

Variable	**Value**	**Units**
Pressure at input port (p_{in})	1	bar
Pressure at output port (p_{out})	4.5	bar
Density of fluid at 1 atm (ρ_{oil})	1005	kg/m^3
Bulk modulus of fluid at 1 atm (β_{oil})	1.4	GPa
Angular speed of inner rotor (ω)	100	rad/s
Dynamic viscosity (μ)	0.01	Pa*s
Pressure in chambers at $t = 0$	1	bar

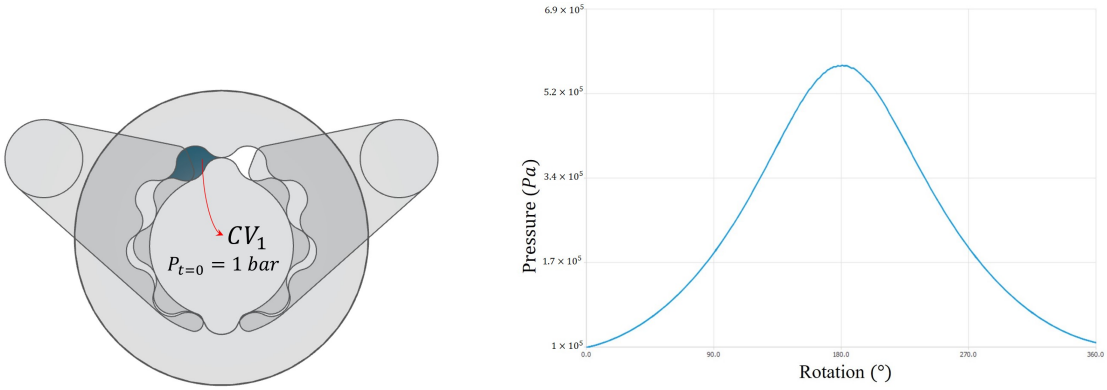

(a) (b)

Figure 4.18: *Cont.*

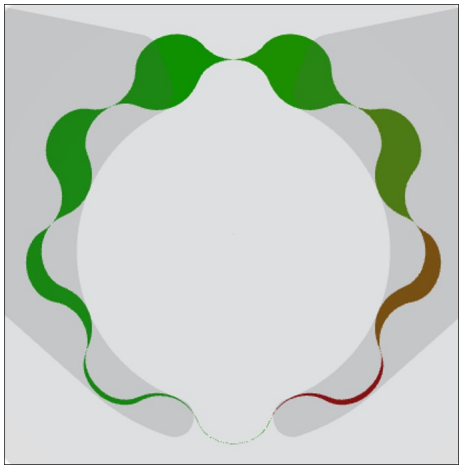

(c)

Figure 4.19: Pressure results from virtual prototype: (**a**) profile of geometry with highlighted chamber (CV_1), (**b**) history of pressure in chamber CV_1, and (**c**) pressure distribution in pump after a full revolution, as seen in Digital Twin (DT).

Figure 4.19c shows the pressure distribution in pump after a full revolution. Notice that there is a peak in pressure in the chambers near the minimum volume position and the pressure starts decreasing after the chamber intersects with the output port and goes through the discharge cycle. The discretization that was used in our virtual prototype allows for the tracking of the history of pressure for each individual chamber. However, the discretization used in the CFD methods make it impossible to track the history of pressure for an individual chamber. This is because, in CFD, the entire discretization (mesh) is updated in every time step (remeshing) to meet convergence requirements [92]. Therefore, for the purposes of comparison against a benchmark (i.e., CFD data), we use the maximal pressure across the entire fluid domain (all chambers). The CFD simulations are currently used in most of the design processes as an accurate prediction of the pump's performance. Therefore, they are a valid point of comparison for our implementation. Figure 4.20 shows the results of maximum pressure in pump, as predicted by both CFD simulation and by our implementation.

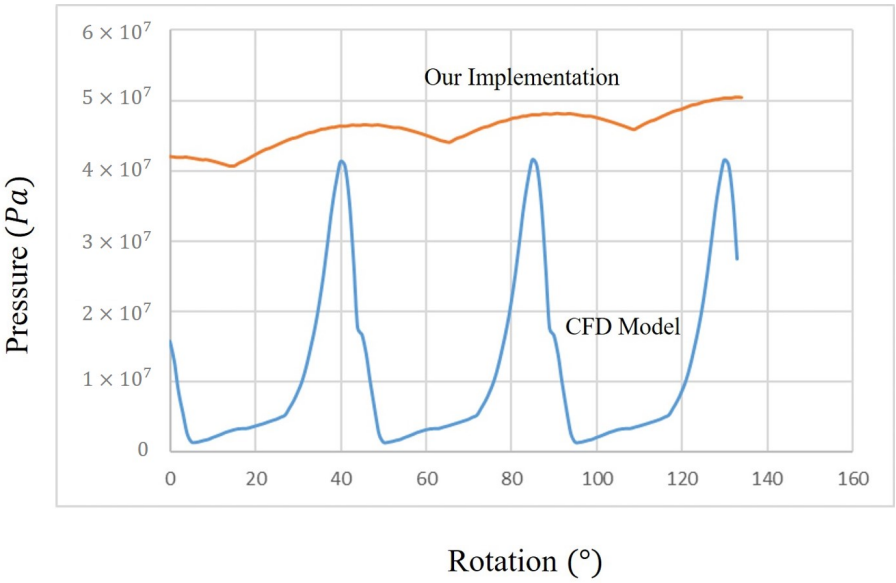

maximum predicted pressure in gerotor pump.

Figure 4.20: Virtual Prototype vs. computational fluid dynamics models (CFD)

Our implemented virtual prototype is able to estimate the maximum pressure within the pump with a relative error of 21%. Our virtual prototype fails to reproduce the amplitude of the pressure oscillation in the pump. We believe that this shortcoming is due to the used assumption of homogeneous pressure in each one of the control volumes. The CFD model does not need such an assumption, and it is able to take into account variations of pressure within the chambers. Still, the maximum pressure in the pump as it rotates through an entire revolution is an important indication of the pump's performance, and it is reasonably estimated by our virtual prototype.

Table 4.2 shows a comparison of pre-processing and simulation times for both a CFD simulation and a simulation with our virtual prototype. The pre-processing time of the CFD simulation includes the generation of CAD models and mesh generation. The pre-processing time in our virtual prototype includes the parameter input for the geometry configuration tool and the automatic generation of B-Rep models. The main advantage of our virtual prototype is the much lower processing and simulation time, while still providing valuable performance information to the design engineer. The economic impact of our prototype upon the maker's functioning is not available at the present time, because of the fact that the design process, at the maker's facilities, is intertwined with other products and processes.

Table 4.2: Comparison of pre-processing and simulation times for the CFD simulation and our virtual prototype.

Task	**CFD Time**	**Our Implementation Time**
Pre-Processing of Geometry	1h	<5 min
Simulation	9 h	<5 min

4.5 Conclusions and Future Work

In this manuscript, we have presented the implementation of a virtual prototype tool in the context of gerotor pump design, a component that has been widely used in different industries and that usually requires time-consuming tasks in the design workflow. Our implementation is a first step towards a fully functional Digital Twin of a gerotor pump. Our implemented tool allows for the integration of data that are collected from an experimental setup with a virtual prototype model. The collected data are fed to the numerical model in order to improve the accuracy of the performance predictions. This allows the engineer to have a fast overview of the performance of the pump and allows him to discard unsuitable geometric configurations in an efficient manner. The presented implementation integrates a 2D design interface with an interactive parameterized model of the pump and a 3D interface. The 3D tool allows for the visualization of the 3D model that corresponds to the previously defined 2D geometry. Our initial tests show that the implemented model to perform fast pre-CFD simulations approaches the result of more detailed and time-consuming simulations within an acceptable margin of error. Our implemented tool also integrates, in a single application, the geometry data and simulation data, which are otherwise treated in different environments. Our virtual prototype is not suitable if a detailed prediction of the behavior inside each chamber of the pump is required.

Future work is needed in the improvement of both the software implemented and the fast simulation model in order to achieve a fully functional Digital Twin tool of the pump. Efforts regarding the 3D tool should be focused on data visualization and the creation of a data structure for simulation profiles of different geometric configurations. A needed improvement of the pre-CFD simulation may be achieved by modeling (a) cavitation and (b) micro-movements in the rotors, due to induced pressure at the chambers. A further integration of experimental data with the simulation model is needed to improve the accuracy of the predictions.

5 Conclusions

This work presents a compilation of publications in applications of Computational Mechanics in which Computational Geometry and Numerical Simulation have a central role. Likewise, tools from mathematics, data structures, algorithms and programming fundamentals are essential for the developed approaches.

This compendium shows a novel method based on the use of design of experiments (DOE) to devise meta-models that adequately estimate the mechanical response of lattice domains. The obtained meta-models correctly fit the data used for their generation. It also shows that the proposed methodology is suitable for the coarse mechanical characterization of large lattice domains, with average errors between 20% and 40%. The proposed approach is also appliable to other types of lattice domains other than Schwarz Primitive.

This document also contributes in the area of Feature Recognition of CAD models. It presents a methodology for the recognition of curved features using geometric filters that allows for a fast albeit specific identification of the desired features. The presented methodology is used in an industrial context within the automotive industry and several examples are presented.

Finally, this manuscript presents a novel implementation in the context of Digital Twins for the design and test of gerotor pumps. The proposed implementation allows for a fast design and test of the different geometric configurations possible for a gerotor pump. Our methodology estimates the maximum pressure within the pump by using a mathematical model and data from a physical test bank.

Finally, the different contributions presented here can be further extended. Therefore, future research can be focused on: (1) the suitability of the best features to approximate the von Mises stress of Schwarz Primitive cells, (2) the development of more robust meta-models that use more information from the displacement fields and consider buckling instabilities, (3) the robustness of the graph search tool and deal with the problem of ambiguous definition of the search graph in

the Feature Recognition tool and (4) the further integration between the digital twin tool and the physical pump.

Bibliography

[1] Jorge-León Posada-Velásquez. *A methodology for the semantic visualization of industrial plant CAD models for virtual reality walkthroughs*. PhD thesis, Technische Universität, 2006.

[2] Juan Camilo Pareja-Corcho, Oscar Mauricio Betancur-Acosta, Oscar E. Ruiz, and Carlos Cadavid. (Short Paper) User-reconfigurable CAD Feature Recognition in 1- and 2-topologies with Reduction of Search Space via Geometry Filters. In *Spanish Computer Graphics Conference (CEIG)*. The Eurographics Association, 2019.

[3] J. Posada, C. Toro, I. Barandiaran, D. Oyarzun, D. Stricker, R. de Amicis, E. B. Pinto, P. Eisert, J. Döllner, and I. Vallarino. Visual Computing as a Key Enabling Technology for Industrie 4.0 and Industrial Internet. *IEEE Computer Graphics and Applications*, 35(2):26–40, 2015.

[4] Mark Helou and Sami Kara. Design, analysis and manufacturing of lattice structures: an overview. *International Journal of Computer Integrated Manufacturing*, 31(3):243–261, 2018.

[5] Camilo Cortés, Maria Osorno, David Uribe, Holger Steeb, Oscar Ruiz-Salguero, Iñigo Barandiaran, and Julián Flórez. Geometry simplification of open-cell porous materials for elastic deformation FEA. *Engineering with Computers*, 35(1):257–276, 2019.

[6] Patrick Terriault and Vladimir Brailovski. Modeling and simulation of large, conformal, porosity-graded and lightweight lattice structures made by additive manufacturing. *Finite Elements in Analysis and Design*, 138:1 – 11, 2018.

[7] Diego Montoya-Zapata, Diego A. Acosta, Camilo Cortés, Juan Pareja-Corcho, Aitor Moreno, Jorge Posada, and Oscar Ruiz-Salguero. Meta-modeling of lattice mechanical responses via design of experiments, 2020. Proceedings of The 2nd International Conference on Mathematics and Computers in Science and Engineering (MACISE 2020). To be published.

[8] Dawei Li, Wenhe Liao, Ning Dai, Guoying Dong, Yunlong Tang, and Yi Min Xie. Optimal design and modeling of gyroid-based functionally graded cellular structures for additive manufacturing. *Computer-Aided Design*, 104:87 – 99, 2018.

[9] Diego Montoya-Zapata, Aitor Moreno, Juan Pareja-Corcho, Jorge Posada, and Oscar Ruiz-Salguero. Density-sensitive implicit functions using sub-voxel sampling in additive manufacturing. *Metals*, 9(12), 2019.

[10] Ajit Panesar, Meisam Abdi, Duncan Hickman, and Ian Ashcroft. Strategies for functionally graded lattice structures derived using topology optimisation for Additive Manufacturing. *Additive Manufacturing*, 19:81–94, 2018.

[11] Jun Wu, Weiming Wang, and Xifeng Gao. Design and optimization of conforming lattice structures. *IEEE Transactions on Visualization and Computer Graphics*, pages 1–1, 2019.

[12] Arash Ataee, Yuncang Li, Darren Fraser, Guangsheng Song, and Cuie Wen. Anisotropic Ti-6Al-4V gyroid scaffolds manufactured by electron beam melting (EBM) for bone implant applications. *Materials & Design*, 137:345 – 354, 2018.

[13] Ferry P.W. Melchels, Katia Bertoldi, Ruggero Gabbrielli, Aldrik H. Velders, Jan Feijen, and Dirk W. Grijpma. Mathematically defined tissue engineering scaffold architectures prepared by stereolithography. *Biomaterials*, 31(27):6909 – 6916, 2010.

[14] Lin Cheng, Pu Zhang, Emre Biyikli, Jiaxi Bai, Joshua Robbins, and Albert To. Efficient design optimization of variable-density cellular structures for additive manufacturing: theory and experimental validation. *Rapid Prototyping Journal*, 23(4):660–677, 2017.

[15] Lu Liu, Paul Kamm, Francisco García-Moreno, John Banhart, and Damiano Pasini. Elastic and failure response of imperfect three-dimensional metallic lattices: the role of geometric defects induced by Selective Laser Melting. *Journal of the Mechanics and Physics of Solids*, 107:160 – 184, 2017.

[16] Sang-In Park and David W. Rosen. Homogenization of Mechanical Properties for Material Extrusion Periodic Lattice Structures Considering Joint Stiffening Effects. *Journal of Mechanical Design*, 140(11), 09 2018. 111414.

[17] Colin Bonatti and Dirk Mohr. Mechanical performance of additively-manufactured anisotropic and isotropic smooth shell-lattice materials: Simulations & experiments. *Journal of the Mechanics and Physics of Solids*, 122:1 – 26, 2019.

[18] Hongshuai Lei, Chuanlei Li, Jinxin Meng, Hao Zhou, Yabo Liu, Xiaoyu Zhang, Panding Wang, and Daining Fang. Evaluation of compressive properties of SLM-fabricated multi-layer lattice structures by experimental test and μ-CT-based finite element analysis. *Materials & Design*, 169:107685, 2019.

[19] Diego Montoya-Zapata, Camilo Cortés, and Oscar Ruiz-Salguero. FE-simulations with a simplified model for open-cell porous materials: A Kelvin cell approach. *Journal of Computational Methods in Sciences and Engineering*, 19:989 – 1000, 2019.

[20] Tore Tryland, Odd S. Hopperstad, and Magnus Langseth. Design of experiments to identify material properties. *Materials & Design*, 21(5):477 – 492, 2000.

[21] Andrejs Kovalovs, Andris Chate, Sergejs Gaidukovs, and Arturs Medvids. Finite element simulation of indentation experiment on branched epoxy novolac resin. *IOP Conference Series: Materials Science and Engineering*, 500:012006, 2019.

[22] Lívia Á. Oliveira, Júlio C. Santos, Túlio H. Panzera, Rodrigo T.S. Freire, Luciano M.G. Vieira, and Fabrizio Scarpa. Evaluation of hybrid-short-coir-fibre-reinforced composites via full factorial design. *Composite Structures*, 202:313 – 323, 2018.

[23] Suwattanarwong Phanphet, Surangsee Dechjarern, and Sermkiat Jomjanyong. Above-knee prosthesis design based on fatigue life using finite element method and design of experiment. *Medical Engineering & Physics*, 43:86 – 91, 2017.

[24] Christina Schäfer and Eckhard Finke. Shape optimisation by design of experiments and finite element methods—an application of steel wheels. *Structural and Multidisciplinary Optimization*, 36(5):477–491, 2008.

[25] Bill Lozanovski, David Downing, Phuong Tran, Darpan Shidid, Ma Qian, Peter Choong, Milan Brandt, and Martin Leary. A monte carlo simulation-based approach to realistic modelling of additively manufactured lattice structures. *Additive Manufacturing*, 32:101092, 2020.

[26] William M. Mendenhall and Terry L. Sincich. *Statistics for Engineering and the Sciences*. CRC Press, 6th edition, 2016.

[27] Meinhard Wohlgemuth, Nataliya Yufa, James Hoffman, and Edwin L. Thomas. Triply periodic bicontinuous cubic microdomain morphologies by symmetries. *Macromolecules*, 34(17):6083–6089, 2001.

[28] I. Maskery, L. Sturm, A.O. Aremu, A. Panesar, C.B. Williams, C.J. Tuck, R.D. Wildman, I.A. Ashcroft, and R.J.M. Hague. Insights into the mechanical properties of several triply periodic minimal surface lattice structures made by polymer additive manufacturing. *Polymer*, 152:62 – 71, 2018.

[29] Grant P. Steven. Homogenization of multicomponent composite orthotropic materials using fea. *Communications in Numerical Methods in Engineering*, 13(7):517–531, 1997.

[30] George E. P. Box, J. Stuart Hunter, and William G. Hunter. *Statistics for experimenters: design, discovery, and innovation*. Wiley Series in Probability and Statistics. Wiley, 2nd edition, 2005.

[31] NIST/SEMATECH. e-Handbook of Statistical Methods. http://www.itl.nist.gov/div898/handbook/. Accessed: 2019–12–04.

[32] J.P. Rizzuto. Experimental investigation of reciprocally supported element (rse) lattice honeycomb domes structural behaviour. *Engineering Structures*, 166:496 – 510, 2018.

[33] Huangchao Yu, Jiaqi Huang, Bin Zou, Wen Shao, and Jikai Liu. Stress-constrained shell-lattice infill structural optimisation for additive manufacturing. *Virtual and Physical Prototyping*, 15(1):35–48, 2020.

[34] X. Ren, L. Xiao, and Z. Hao. Multi-property cellular material design approach based on the mechanical behaviour analysis of the reinforced lattice structure. *Materials & Design*, 174:107785, 2019.

[35] R Core Team. *R: A Language and Environment for Statistical Computing*. R Foundation for Statistical Computing, Vienna, Austria, 2019.

[36] Zhibin Niu, Ralph R Martin, Frank C Langbein, and Malcolm A Sabin. Rapidly finding cad features using database optimization. *Computer-Aided Design*, 69:35–50, 2015.

[37] Alain Bezos. Step: The iso 10303 standard for product data exchange and representation. In *Industrial Information and Design Issues*. Springer Berlin Heidelberg, 1996.

[38] Bradford Smith and Joan Wellington. Initial graphics exchange specification (iges); version 3.0. Technical report, US. Nat. Bureau Stand., 1986.

[39] Jorge Posada, Stefan Wundrak, Andre Stork, and Carlos Toro. Semantically controlled lmv techniques for plant design review. In *ASME 2004 International Design Engineering Technical Conferences and Computers and Information in Engineering Conference*, pages 329–335. American Society of Mechanical Engineers Digital Collection, 2004.

[40] Álvaro Segura, Helen V Diez, Iñigo Barandiaran, Ander Arbelaiz, Hugo Álvarez, Bruno Simões, Jorge Posada, Alejandro García-Alonso, and Ramón Ugarte. Visual computing technologies to support the operator 4.0. *Computers & Industrial Engineering*, 139:105550, 2020.

[41] Carlos Toro, Javier Vaquero, Manuel Graña, Cesar Sanín, Edward Szczerbicki, and Jorge Posada. Building domain ontologies from engineering standards. *Cybernetics and Systems*, 43(2):114–126, 2012.

[42] PK Jain and Sharvan Kumar. Automatic feature extraction in prizcapp. *International Journal of Computer Integrated Manufacturing*, 11(6):500–512, 1998.

[43] N Ismail, N Abu Bakar, and AH Juri. Feature recognition patterns for form features using boundary representation models. *The International Journal of Advanced Manufacturing Technology*, 20(8):553–556, 2002.

[44] N Ismail, N Abu Bakar, and AH Juri. Recognition of cylindrical and conical features using edge boundary classification. *International Journal of Machine Tools and Manufacture*, 45(6):649–655, 2005.

[45] B Babic. Development of an intelligent cad-capp interface. In *Proceedings of the International Conference on Intelligent Technologies in Human-Related Sciences*, pages 351–357, 1996.

[46] B Babić and Z Miljković. Feature recognition as the basis for integration of cad and capp systems. *Intelligent Manufacturing Processes and Systems*, pages 596–601, 1997.

[47] HKD Bouzakis and G Andreadis. A feature-based algorithm for computer aided process planning for prismatic parts. *Int. J. Prod. Eng. Comput*, 3(3):17–22, 2000.

[48] Tien-Chien Chang. *Expert process planning for manufacturing*. Addison-Wesley Longman, 1990.

[49] O Owodunni and S Hinduja. Evaluation of existing and new feature recognition algorithms: Part 1: Theory and implementation. *Proceedings of the Institution of Mechanical Engineers, Part B: Journal of Engineering Manufacture*, 216(6):839–851, 2002.

[50] Prasad S Gavankar and Mark R Henderson. Graph-based extraction of two-connected morphological features from boundary representations. *Journal of Intelligent Manufacturing*, 6(6):401–413, 1995.

[51] Patri K Venuvinod and SY Wong. A graph-based expert system approach to geometric feature recognition. *Journal of Intelligent Manufacturing*, 6(3):155–162, 1995.

[52] AK Verma and S Rajotia. Feature vector: a graph-based feature recognition methodology. *International journal of production research*, 42(16):3219–3234, 2004.

[53] Yoonhwan Woo and Hiroshi Sakurai. Recognition of maximal features by volume decomposition. *Computer-Aided Design*, 34(3):195–207, 2002.

[54] Yong Se Kim. Recognition of form features using convex decomposition. *Computer-Aided Design*, 24(9):461–476, 1992.

[55] S. Nagarajan and N. Venkata Reddy. Step-based automatic system for recognising design and manufacturing features. *International Journal of Production Research*, 48(1):117–144, 2010.

[56] Zhibin Niu, Ralph R Martin, Malcolm Sabin, Frank C Langbein, and Henry Bucklow. Applying database optimization technologies to feature recognition in cad. *Computer-aided design and applications*, 12(3):373–382, 2015.

[57] Bitla Venu and Venkateswara Rao Komma. Step-based feature recognition from solid models having non-planar surfaces. *International Journal of Computer Integrated Manufacturing*, 30(10):1011–1028, 2017.

[58] Oscar ES Ruiz, Rodrigo A Marin, and Placid M Ferreira. A geometric reasoning server with applications to geometric constraint satisfaction and configurable feature extraction. In *Modelling and Graphics in Science and Technology*, pages 62–76. Springer, 1996.

[59] Bojan Babic, Nenad Nesic, and Zoran Miljkovic. A review of automated feature recognition with rule-based pattern recognition. *Computers in industry*, 59(4):321–337, 2008.

[60] J. Russell and R. Cohn. *Open Cascade Technology*. Book on Demand, 2012.

[61] Spatial Technology Inc. ACIS geometric modeler, 1995.

[62] Oscar Ruiz, Santiago Arroyave, and Diego Acosta. Fitting of analytic surfaces to noisy point clouds. *American Journal of Computational Mathematics, Volume 3, Issue 1A, pp 18-26*, 2013.

[63] Manfredo P Do Carmo. *Differential geometry of curves and surfaces: revised and updated second edition*. Courier Dover Publications, 2016.

[64] Silvère Gauthier, William Puech, Roseline Bénière, and Gérard Subsol. Analysis of digitized 3d mesh curvature histograms for reverse engineering. *Computers in Industry*, 92:67–83, 2017.

[65] Vicomtech. GeomLib: Geometry library. https://www.vicomtech.org/en/rdi-tangible/software-libraries, 2020.

[66] Ruwen Schnabel, Roland Wahl, and Reinhard Klein. Efficient ransac for point-cloud shape detection. In *Computer graphics forum*, volume 26, pages 214–226. Wiley Online Library, 2007.

[67] László Babai and Eugene M. Luks. Canonical labeling of graphs. In *Proceedings of the Fifteenth Annual ACM Symposium on Theory of Computing*, STOC '83, pages 171–183, New York, NY, USA, 1983. ACM.

[68] László Babai. Graph isomorphism in quasipolynomial time. *CoRR*, abs/1512.03547, 2015.

[69] JungHyun Han, Mike Pratt, and William C Regli. Manufacturing feature recognition from solid models: a status report. *IEEE transactions on robotics and automation*, 16(6):782–796, 2000.

[70] P Gibson, HS Ismail, and MA Sabin. Optimisation approaches in feature recognition. *International Journal of Machine Tools and Manufacture*, 39(5):805–821, 1999.

[71] Jonathan Dekhtiar, Alexandre Durupt, Matthieu Bricogne, Benoit Eynard, Harvey Rowson, and Dimitris Kiritsis. Deep learning for big data applications in cad and plm research review, opportunities and case study. *Computers in Industry*, 100:227 – 243, 2018.

[72] Pedro Javier Gamez-Montero, Esteve Codina, and Robert Castilla. A review of gerotor technology in hydraulic machines. *Energies*, 12(12):2423, 2019.

[73] R Castilla, PJ Gamez-Montero, N Ertürk, A Vernet, M Coussirat, and E Codina. Numerical simulation of turbulent flow in the suction chamber of a gearpump using deforming mesh and mesh replacement. *International Journal of Mechanical Sciences*, 52(10):1334–1342, 2010.

[74] Guillaume Houzeaux and Ramon Codina. A finite element method for the solution of rotary pumps. *Computers & Fluids*, 36(4):667–679, 2007.

[75] Chiu-Fan Hsieh. Fluid and dynamics analyses of a gerotor pump using various span angle designs. *Journal of Mechanical Design*, 134(12), 2012.

[76] Jun Ho Bae, Hyo Seo Kwak, Sereisith San, and Chul Kim. Design and cfd analysis of gerotor with multiple profiles (ellipse–involute–ellipse type and 3-ellipses type) using rotation and translation algorithm. *Proceedings of the Institution of Mechanical Engineers, Part C: Journal of Mechanical Engineering Science*, 230(5):804–823, 2016.

[77] Massimo Rundo and Giorgio Altare. Lumped parameter and three-dimensional cfd simulation of a variable displacement vane pump for engine lubrication. In *Fluids Engineering Division Summer Meeting*, volume 58042, page V01AT03A007. American Society of Mechanical Engineers, 2017.

[78] Pedro-Javier Gamez-Montero, Robert Castilla, David del Campo, Nihal Ertürk, Gustavo Raush, and Esteve Codina. Influence of the interteeth clearances on the flow ripple in a gerotor pump for engine lubrication. *Proceedings of the Institution of Mechanical Engineers, Part D: Journal of Automobile Engineering*, 226(7):930–942, 2012.

[79] Matteo Pellegri, Andrea Vacca, Emma Frosina, Dario Buono, and Adolfo Senatore. Numerical analysis and experimental validation of gerotor pumps: A comparison between a lumped parameter and a computational fluid dynamics-based approach. *Proceedings of the Institution of Mechanical Engineers, Part C: Journal of Mechanical Engineering Science*, 231(23):4413–4430, 2017.

[80] Matteo Pellegri, Andrea Vacca, Ram S Devendran, Etienne Dautry, and Benjamin Ginsberg. A lumped parameter approach for gerotor pumps: model formulation and experimental validation. 2016.

[81] YG Shah, A Vacca, S Dabiri, and E Frosina. A fast lumped parameter approach for the prediction of both aeration and cavitation in gerotor pumps. *Meccanica*, 53(1-2):175–191, 2018.

[82] Massimo Rundo. Models for flow rate simulation in gear pumps: A review. *Energies*, 10(9):1261, 2017.

[83] Fei Tao, He Zhang, Ang Liu, and Andrew YC Nee. Digital twin in industry: State-of-the-art. *IEEE Transactions on Industrial Informatics*, 15(4):2405–2415, 2018.

[84] Flávia Pires, Ana Cachada, José Barbosa, António Paulo Moreira, and Paulo Leitão. Digital twin in industry 4.0: Technologies, applications and challenges. In *2019 IEEE 17th International Conference on Industrial Informatics (INDIN)*, volume 1, pages 721–726. IEEE, 2019.

[85] Daniel Mejia, Aitor Moreno, Ander Arbelaiz, Jorge Posada, Oscar Ruiz-Salguero, and Raúl Chopitea. Accelerated thermal simulation for three-dimensional interactive optimization of computer numeric control sheet metal laser cutting. *Journal of Manufacturing Science and Engineering*, 140(3), 2018.

[86] Daniel Mejia-Parra, Ander Arbelaiz, Oscar Ruiz-Salguero, Juan Lalinde-Pulido, Aitor Moreno, and Jorge Posada. Fast simulation of laser heating processes on thin metal plates with fft using cpu/gpu hardware. *Applied Sciences*, 10(9):3281, 2020.

[87] Pedro Javier Gámez Montero. *Caracterizacion fluidodinamica de una bomba oleohidráulica de engranajes internos generados por perfiles trocoidales*. Universitat Politècnica de Catalunya, 2004.

[88] Soon-Man Kwon, Han Sung Kang, and Joong-Ho Shin. Rotor profile design in a hypogerotor pump. *Journal of mechanical science and technology*, 23(12):3459–3470, 2009.

[89] Sunghun Kim and Hubertus Murrenhoff. Measurement of effective bulk modulus for hydraulic oil at low pressure. *Journal of Fluids Engineering*, 134(2), 2012.

[90] Bruno Simões, Carles Creus, María del Puy Carretero, and Álvaro Guinea Ochaíta. Streamlining xr technology into industrial training and maintenance processes. In *The 25th International Conference on 3D Web Technology*, Web3D '20, New York, NY, USA, 2020. Association for Computing Machinery.

[91] Bruno Simões, María del Puy Carretero, and Jorge Martínez Santiago. Photorealism and kinematics for web-based cad data. In *The 25th International Conference on 3D Web Technology*, Web3D '20, New York, NY, USA, 2020. Association for Computing Machinery.

[92] Roberto Castilla López, Pedro Javier Gámez Montero, Gustavo Adolfo Raush Alviach, and Esteban Codina Macià. Three dimensional simulation of gerotor with deforming mesh by using openfoam. In *Fluid power networks: proceedings: 19th-21th March 2018: 11th International Fluid Power Conference*, pages 260–271, 2018.